

UNIVERSITÀ DEGLI STUDI ROMA TRE

---

DIPARTIMENTO DI MATEMATICA E FISICA



# Far-infrared optical properties of Ge/SiGe quantum well systems

Diego Sabbagh

in partial fulfillment of the requirements  
for the degree of

Doctor of Philosophy in Physics

under the supervision of  
Professor Monica De Seta

XXVIII ciclo, December 2015



# Contents

	Page
List of Figures . . . . .	iii
List of Tables . . . . .	vi
List of Constants . . . . .	vi
<b>Introduction</b>	<b>1</b>
<b>1 Silicon-Germanium heterostructures</b>	<b>5</b>
1.1 General properties of SiGe alloys . . . . .	5
1.2 Strain and dislocations . . . . .	7
1.2.1 Strain effect on the electronic properties . . . . .	13
1.3 Band alignment in SiGe heterostructures . . . . .	14
1.4 SiGe heterostructures growth techniques . . . . .	17
1.4.1 Virtual substrates . . . . .	18
<b>2 Inter-subband transitions in quantum wells</b>	<b>21</b>
2.1 Quantum wells properties . . . . .	21
2.2 Inter-subband transitions . . . . .	27
2.3 Bi-dimensional absorption coefficient . . . . .	30
2.3.1 Transmittance and absorption coefficient . . . . .	31
2.4 Inverse effective mass tensor . . . . .	33
2.5 Non-ideal effects and corresponding corrections . . . . .	35
<b>3 Sample growth and structural characterization</b>	<b>39</b>
3.1 CVD growth setup . . . . .	39
3.1.1 In-situ physical characterization technique . . . . .	41
3.2 Ex-situ structural characterization techniques . . . . .	43
3.3 Substrate preparation . . . . .	45
3.4 Virtual substrate . . . . .	47
3.5 Ge/SiGe heterostructures . . . . .	49
3.6 Waveguide realization . . . . .	52
<b>4 Optical characterization</b>	<b>55</b>
4.1 Fourier Transform InfraRed spectroscopy . . . . .	55
4.1.1 Setup description . . . . .	56
4.1.2 Acquisition geometry . . . . .	59
4.1.3 Bi-dimensional absorption coefficient . . . . .	61

4.2	Degenerate pump-probe spectroscopy . . . . .	63
4.3	Pump-Probe/Time-Domain Spectroscopy . . . . .	67
4.3.1	Setup description . . . . .	67
4.3.2	Optical rectification and electro-optical sampling . . . . .	69
4.3.3	ACQW relaxation times estimation . . . . .	72
4.4	Optical characterization of MQW samples . . . . .	73
4.4.1	Absorption energies and carrier densities . . . . .	74
4.4.2	Linewidth broadening . . . . .	79
4.4.3	Degenerate pump-probe measurements . . . . .	87
4.5	Optical characterization of ACQW samples . . . . .	90
4.5.1	Quantum Fountain . . . . .	90
4.5.2	Absorption energies . . . . .	92
4.5.3	Relaxation times . . . . .	95
4.5.4	Spectral analysis and gain extrapolation . . . . .	97
<b>Conclusions</b>		<b>103</b>
<b>Publications</b>		<b>107</b>
<b>Bibliografy</b>		<b>109</b>

# List of Figures

1.1	Si and Ge crystal structure in the reciprocal space. . . . .	5
1.2	Band structure of Si and Ge at room temperature. . . . .	6
1.3	Constant energy surfaces in the conduction band of Si and Ge. . . . .	6
1.4	SiGe alloys band gap energy as a function of Ge content. . . . .	7
1.5	Lattice deformation of an epilayer with higher and lower lattice parameter compared to the substrate. . . . .	9
1.6	Elastic relaxation with islands in the epilayer and Bauer classification. . . . .	10
1.7	Formation of a threading dislocation at the interface between two materials with different lattice parameter. . . . .	11
1.8	Critical thickness behavior in different $\text{Si}_{1-y}\text{Ge}_y/\text{Si}_{1-x}\text{Ge}_x$ systems. . . . .	12
1.9	Example of a strain-compensated structure. . . . .	13
1.10	$\text{Si}_{1-x}\text{Ge}_x$ conduction band edge shift at $\Delta$ point as effect of strain. . . . .	14
1.11	Possible heterostructure band alignments. . . . .	15
1.12	Band alignment properties of $\text{Si}_{1-x}\text{Ge}_x/\text{Si}_{1-y}\text{Ge}_y$ heterostructure . . . . .	15
1.13	Type I band alignment in a $\text{Ge}/\text{Si}_{0.2}\text{Ge}_{0.8}$ quantum well. . . . .	16
1.14	Silane and germane pyrolysis scheme. . . . .	17
1.15	Transmission electron microscopy images of Ge layers on Si substrate at different growth temperatures. . . . .	19
1.16	TEM images of linear and reverse graded virtual substrates. . . . .	19
2.1	Single QW in material B confined by barriers of material A. . . . .	22
2.2	Subband energy dispersion in the growth plane. . . . .	23
2.3	Solutions of the Schrödinger equation for an infinite potential well. . . . .	24
2.4	Graphic method for solving the Schrödinger equation of a finite potential well. . . . .	25
2.5	Comparison between the first and second level energies in infinite and finite wells. . . . .	25
2.6	ACQW scheme. . . . .	26
2.7	Inter-band and inter-subband transitions. . . . .	27
2.8	Vertical transitions between parabolic subbands. . . . .	29
2.9	Example of absorption spectra for QWs of different width. . . . .	31
2.10	Waveguide geometry scheme. . . . .	33
2.11	Effect of the subbands non-parabolicity on the transition energy. . . . .	37
2.12	Band bending in modulation doped QWs. . . . .	37
3.1	Growth setup scheme. . . . .	40
3.2	Example of an XPS spectrum. . . . .	42

3.3	Scheme of an AFM measurement. . . . .	43
3.4	Sketch of the TEM geometry acquisition. . . . .	44
3.5	Sample holder side and top view. . . . .	46
3.6	AFM images of a virtual substrate at different growth stages. . . . .	48
3.7	STEM image of the reverse graded virtual substrate of sample S2. . . . .	49
3.8	Sample S7 STEM-HAADF and AFM images. . . . .	51
3.9	XRD measurement of sample S6. . . . .	52
3.10	Steady solution of the Maxwell equations inside the waveguide. . . . .	53
3.11	Sample waveguide geometry sketch. . . . .	53
4.1	Michelson interferometer, interferogram and source spectrum. . . . .	56
4.2	Interferometer schemes. . . . .	57
4.3	Cryostat description. . . . .	58
4.4	Bolometer scheme and picture. . . . .	59
4.5	Sample waveguide mounted on the cryostat. . . . .	60
4.6	Light propagation inside the sample waveguide. . . . .	61
4.7	Example of normalized transmittances in TM and TE polarizations, and corresponding dichroic signal. . . . .	62
4.8	Simulated transition rate in Ge and GaAs QWs. . . . .	63
4.9	Degenerate pump-probe measurement scheme. . . . .	64
4.10	Simulations on sample S6 relevant physical quantities as a function of pump-probe delay. . . . .	66
4.11	Pump-probe/TDS setup scheme. . . . .	68
4.12	Detection process scheme of the probe beam coming out of the ZnTe detection crystal. . . . .	71
4.13	Time trace profile and spectral content of the THz probe pulse. . . . .	72
4.14	Bi-dimensional absorption coefficient for samples with different well width. . . . .	74
4.15	Fit results for sample S6 and S4 at 8 K. . . . .	75
4.16	Calculated conduction band edge profiles of L, $\Delta_2$ , $\Delta_4$ and $\Gamma$ valleys. . . . .	76
4.17	Calculations on samples S2 and S1 structure. . . . .	77
4.18	ISB transition energy dependence on increasing temperature for sam- ples S2 and S1. . . . .	78
4.19	Scattering contributions to $\Gamma^{th}$ for sample S3 and S6 . . . . .	83
4.20	Linewidth broadening contributions to $\Gamma^{th}$ for samples S1 and S4 . . . . .	84
4.21	Sample S1 intra- and inter-subband $\Gamma^{II}$ contribution as a function of donor distance. . . . .	85
4.22	Sample S1 linewidth broadening and integrated absorbance as a func- tion of lattice temperature. . . . .	85
4.23	Measured values of $\Gamma$ as a function of carrier density and well width. . . . .	86
4.24	Sample S2 pump-probe signals at $T = 30$ K and $T = 90$ K. . . . .	88
4.25	Samples S4 and S4bis pump-probe signals at different temperatures and pump powers. . . . .	89
4.26	Operation scheme of a QF device. . . . .	91
4.27	Calculation of sample S9 structure. . . . .	93
4.28	Low temperature dichroic signal of samples S10, S8 and S9. . . . .	93
4.29	Relaxation dynamics of sample S9. . . . .	95

4.30	Low temperature spectrally resolved data and electrodynamic model of the relative transmittance change in samples S9 and S8. . . . .	98
4.31	ISB transition intensity and free carrier absorption as a function of increasing pumping power. . . . .	100
4.32	Calculated ISB gain function of sample S9 for increasing FEL pump power. . . . .	101

# List of Tables

1.1	Elastic constants for Si, Ge and SiGe alloys. . . . .	8
3.1	Example of step graded $\text{Si}_{1-x}\text{Ge}_x$ layers deposition conditions. . . . .	48
3.2	Samples growth parameters. . . . .	50
4.1	Samples structural and optical properties. . . . .	75
4.2	Single-well samples properties (S1-S7). . . . .	82
4.3	Experimental conditions and fit results of the pump-probe measurements. . . . .	87
4.4	ACQW samples structural parameters and predicted transition energies. . . . .	92
4.5	Experimental and theoretical relaxation times of sample S9 at different temperatures, pump powers and pump energies. . . . .	96
4.6	Drude-Lorentz model parameters at different FEL pump powers. . . . .	99

# List of Constants

Symbol	Name	Value	Unit
$\hbar$	Reduced Planck constant	$6.582 \cdot 10^{-16}$	eV·s
$\pi$	Pi constant	3.14159	
$e$	Electron charge	$-1.602 \cdot 10^{-19}$	C
$\varepsilon_0$	Vacuum permittivity	$8.854 \cdot 10^{-12}$	F/m
$c$	Speed of light	$3 \cdot 10^8$	m/s
$m_e$	Electron mass	$9.1 \cdot 10^{-31}$	Kg
$k_B$	Boltzmann constant	$8.617 \cdot 10^{-5}$	eV/K
$Z_0$	Free space impedance	377	$\Omega$



# Introduction

The microelectronic industry is nowadays fully dominated by silicon, mostly thanks to the outstanding thermal and mechanical properties exhibited by this material and by its native oxide, needed for the realization of the CMOS platform. On the other hand, the electronic structure of silicon makes it unexploitable in any application involving optics or opto-electronics. The main problem is the indirect nature of the silicon band gap which prevents radiative recombination between conduction and valence bands, resulting in the almost total absence of good silicon-based emitters and detectors. These devices, including lasers, are today realized mainly in compounds of III-V semiconductors and therefore a monolithic photonic integration with the mainstream electronic platform is still far from being achieved, since the employed materials are not compatible with silicon. Several techniques have been investigated in order to obtain III-V materials on silicon, like heteroepitaxial growth or wafer bonding, but the most desirable approach remains the realization of opto-electronic devices in silicon-compatible materials directly grown on silicon substrates.

In this context, the recent breakthroughs in the epitaxial deposition techniques opened the possibility to realize a large number of artificial structures with attracting properties from many points of view. The state of the art in semiconductor deposition now allows the growth of periodic systems of few atomic layers of different composition in which the charges are confined in low-dimensional structures called *quantum wells* (QWs). The quantum effects arising from their low-dimensional nature can be exploited in several manners, for example with the aim of obtaining radiative emission from silicon-compatible materials. In fact, in these periodic *heterostructures*, dipole-active transitions between the confined levels have clearly demonstrated their potential for infrared light emission [1–5]. Each level in a QW is constituted by a two-dimensional electron energy level called *subband*, and therefore the transitions involving them are named *inter-subband* (ISB) transitions. One important property of ISB light emitters is that they are unipolar devices, i.e. they do not require the use of semiconductors with a direct bandgap because either electrons or holes are involved in the emission process, and the radiative emission does not depend on electron-hole recombination between conduction and valence bands. This property makes ISB transition design a viable route toward the realization of silicon-based monolithic light emitters, employing silicon-compatible group-IV semiconductor materials such as germanium (Ge) and tin (Sn) [6–18], even if with indirect band gap. With the employment of these materials, light emitters realized on silicon (Si) wafers could be integrated in the CMOS technology platform [9, 16–18] and thus, although working at low temperatures and in the far-infrared range [6, 7],

they have the potential to open the field of silicon photonics beyond the telecom technology to several applications.

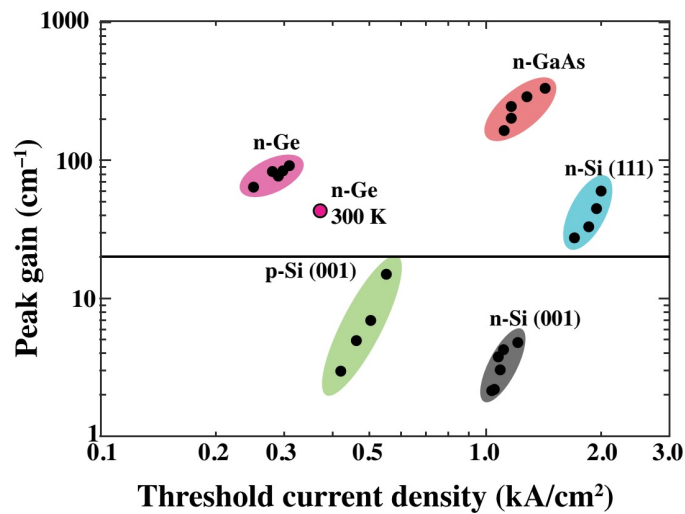
After the first demonstration in 1994 of the quantum cascade laser (QCL) [19], coherent ISB emitters based on electron injection-tunneling between coupled QWs [20] are now an established technology, although QCL are still realized only in III-V semiconductor heterostructures. The polar nature of these compounds limits the emission efficiency specially at room temperature because of the strong interaction with optical phonons, which generates high-rate non-radiative electron relaxation. Moreover, the strong coupling with optical phonons in III-V emitters leads to a forbidden emission range in the far-infrared energy region named *THz gap*, in which any radiative emission is prevented. This means that nowadays compact and efficient emitters in the range of 0.3-10 THz (around 1-40 meV) do not exist yet, excluding the possibility to exploit THz radiation for a number of important applications. In fact, the THz region of the electromagnetic spectrum is of great interest in many fields both from a theoretical point of view and for technological applications [4,9,21]. In spectroscopy, for example, a microscope working in the THz range could be extremely useful in material investigations, allowing to extract important properties as mobility, conductivity and charge density. It could be also possible to obtain images through materials that normally block any incident radiation from the common sources, with a resolution even higher compared to the techniques based on microwaves. Another field of recent interest involves both biology and medicine, where the THz radiation could be used to study inter-molecular vibrations of organic molecules, drugs, tumor tissues, DNA and more. The main advantage of THz investigations over the common infrared ones consists in the possibility to discriminate differences in absorption spectra due to temperature variations, as peculiar of many organic and pharmacological compounds. Concerning the security field, THz sources and detectors allow fast and reliable detection of several chemical components used in explosives and narcotics, whose absorption spectra can be easily acquired without the need of opening and damaging their packaging. In addition to this, THz camera could be employed in critical conditions, for example in airports, since they are able to perform detection even through fog and smoke. The THz radiation has attracted interest also in the ICT field, promising the development of technologies for data transfer via optical fiber above the Tb/s, and wireless communications at speed around the Gb/s.

The current interest in THz detectors and sources as QCL is therefore motivated by several applications in different fields of both technology and basic science. Moreover, in the past two decades, the fundamental investigations on heterostructures for THz applications have been made possible by the availability of ultrafast femtosecond lasers and by the development of down-conversion elements such as optical rectification devices, which allow the production of single-cycle THz pulses for probing the physical properties of the systems under investigation [22,23]. The availability of such technology, together with the mentioned motivations in this field, encouraged many groups in the world to reach the goal of covering the THz gap and achieve coherent emission in suitable devices. In this regard, the employment of heterostructures made of Si-compatible group-IV semiconductors seems to be a promising route towards the realization of optical devices working at higher temperatures compared to the more common III-V systems, thanks to the non-polar

nature of their alloys [12, 15, 24].

Previous studies [6] demonstrated the possibility to induce ISB transitions in the valence band of Si/SiGe heterostructures, i.e. Si QWs sandwiched between SiGe layers acting as confining barriers, facing however many problems mostly due to mixing of the three valence bands. The choice of ISB transitions in the valence band were driven by the low value of the Si effective mass therein and by a very high band offset confining the QW subbands but, in any case, they were found to be unexploitable for light emission. A significant improvement over the p-type structures has been theorized to be possible in n-type QW heterostructures, which should in principle allow for higher gain in emitter structures. The figure below displays the predictions on the achievable peak gain of devices realized in different materials as a function of their threshold current density. It is clear that several n-type structures offer the possibility to achieve radiative emission. Although the predicted peak gain is still far from the values obtained in devices realized in III-V systems, n-type Ge structures seem to be suitable for lasing even at lower threshold currents up to room temperature (see the figure), where III-V systems notoriously cannot emit.

Exploiting the advantage of the n-type structures, ISB transitions in Si conduction band have been reported [26, 31] but the high effective mass has hold back the realization of such structures so far [5]. On the contrary, n-type structures based on Ge QWs are predicted to reach higher gain values at lower threshold current densities, and their several advantages promise to achieve high optical performances. In fact, the low effective mass in the conduction band and the absence of band mixing make this kind of structure perfect candidates for the future realization of THz devices. Theoretical investigations [15, 32] support this scenario, showing how heterostructures realized in compressive strained Ge QWs confined by SiGe barriers of high Ge content exhibit a type I band alignment at L point with a band offset around 100 meV, which properties are found to be suitable for the realization of



A theoretical comparison of identical QW heterostructure designs produced in different technologies. The line corresponds to the minimum waveguide losses, therefore all devices above the line should produce lasing [25].

THz emitters.

In this context, the aim of the present work of thesis is to realize and characterize Ge/SiGe QW heterostructures featuring the needed properties for the implementation in THz emitter devices. To overcome the difficulties in the growth of Ge systems on Si due to the high lattice mismatch between the two materials, an optimization of the deposition process is conducted and the suitable strategy to obtain high quality structures is adopted. Several Ge/SiGe QW samples with different characteristics have been grown and a thorough study is conducted on both structural and optical properties. Specific attention has been paid to the requirements for the realization of a *quantum fountain* laser, an emitter device in which the radiative emission is triggered by optical pumping instead of electron injection from metal contacts as in QCL. Although lasing from quantum fountains have been successfully achieved in many III-V systems [33–39], designs on group-IV materials are seldom reported [40] and a working device is still missing.

First of all, the fundamental electronic and structural properties of the Ge/SiGe heterostructures will be presented in the first chapter. In particular, we studied the effect of the strain and the materials lattice mismatch on the grown structures.

An in-dept analysis on ISB transitions in QW systems will follow in the second chapter, showing the procedure employed to retrieve the sample bi-dimensional absorption coefficient from the measured transmittance. Non-ideal effects occurring in the investigated structures are also briefly considered together with consequences they lead to.

In the third chapter the deposition techniques will be discussed, paying specific attention to the features allowing the integration with the mainstream technology for the microelectronic production at large scale. All the steps required to obtain a high quality heterostructure are analyzed in details from the Si substrate preparation to the deposition of the final QW active region, on top of a proper virtual substrate. The structural properties of the samples we realized are also reported, together with the results of the structural characterization performed.

The fourth chapter will report the optical characterization we conducted on the investigated samples, in collaboration with several international groups which also granted us the access to their laboratories and facilities. Fourier transform infrared (FTIR) spectroscopy, pump-probe and time-domain spectroscopy (TDS) investigations are performed and the obtained results compared to the predictions available from the employed theoretical models. Finally, the possibility to achieve positive material gain in a future Ge/SiGe quantum fountain is discussed.

# 1

## Silicon-Germanium heterostructures

The present work of thesis focuses on optical investigations on heterostructures realized in silicon-germanium (SiGe) alloys. Before analyzing any optical feature of the studied samples it is important to understand the properties of the material they are made of. To this aim, this first chapter introduces the fundamental properties of silicon, germanium and their alloys. The techniques employed to grow the heterostructures are analyzed and the main problems to be faced in their realization are also discussed.

### 1.1 General properties of SiGe alloys

Silicon (Si) and germanium (Ge) are semiconductors with a face-centered cubic (FCC) structure belonging to the IV group of the periodic table of elements. They are compatible with each other and therefore it is possible to realize stable alloys  $\text{Si}_{1-x}\text{Ge}_x$  with relative concentration  $x$  that manifest continuously varying properties from those typical of Si to those typical of Ge. The first Brillouin zone in the reciprocal space is shown in fig. 1.1, where the most interesting directions are highlighted [41].

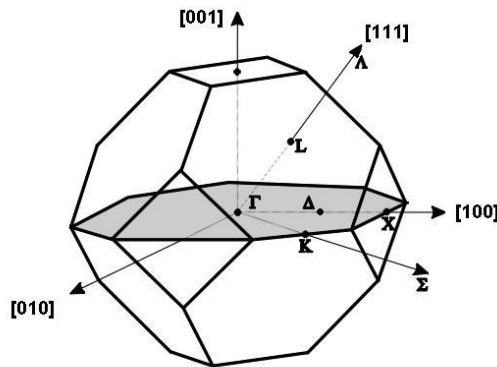


Figure 1.1: Si and Ge crystal structure in the reciprocal space.

Both Si and Ge are semiconductors with indirect band gap: they have the maximum of the valence band in the  $\Gamma$  point of the reciprocal space, but the minimum of the conduction band in a different position. The Si conduction band minimum exhibits a six-fold degeneracy and it is located in the  $\Delta$  point, along the  $[100]$  direction connecting  $\Gamma$  to X. At room temperature, the indirect band gap at  $\Delta$  is  $E_g^\Delta = 1.12$  eV, while the energy band separation at  $\Gamma$  is  $E_g^\Gamma = 3.40$  eV [42]. On the contrary, the Ge conduction band minimum exhibits a four-fold degeneracy (8 semi-ellipsoids) and it is located in the L point, along the  $[111]$  direction. In this case, the indirect band gap is  $E_g^L = 0.66$  eV, while the energy band separation at  $\Gamma$  is  $E_g^\Gamma = 0.80$  eV [42]. Figures 1.2 and 1.3 show the bulk band structure of the two materials and their minima many-fold degeneracy sketch, respectively. Another important difference is the value in the conduction band effective mass along the  $[100]$  direction, which are  $m^* = 0.92m_e$  for Si at  $\Delta$  point and  $m^* = 0.12m_e$  for Ge at L point. As it will be discussed later, this difference leads to important consideration on the optical properties of the two materials.

The band structure of the  $\text{Si}_{1-x}\text{Ge}_x$  alloys has been profusely studied with many

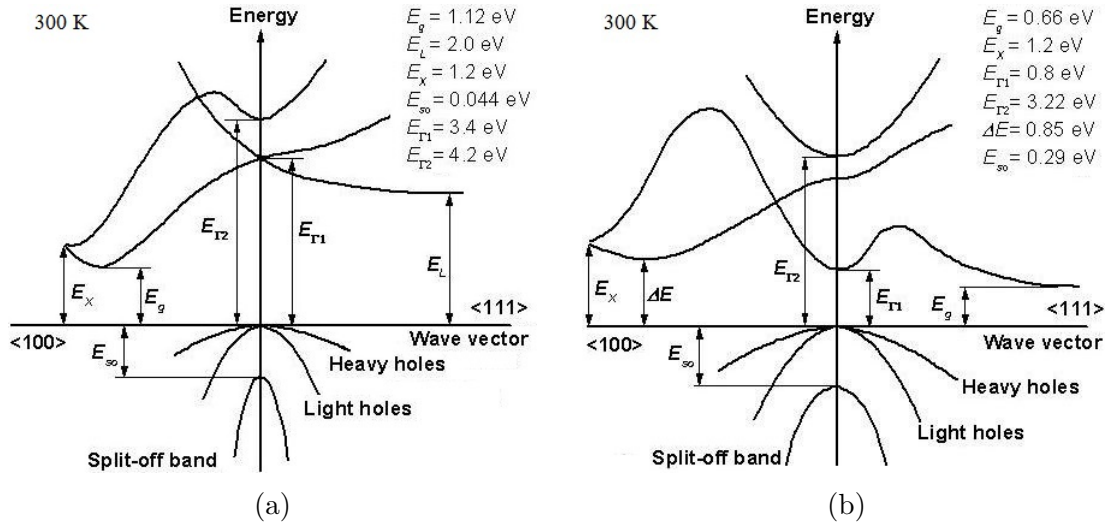


Figure 1.2: Band structure of Si (a) and Ge (b) at room temperature.

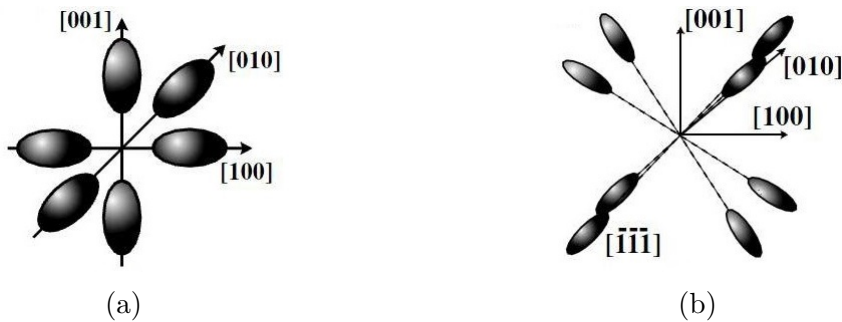


Figure 1.3: Constant energy surfaces in the conduction band of Si (a) and Ge (b). Ge has half of each ellipsoid in the adjacent cells, resulting in 8 semi-ellipsoids per cell (four-fold degeneracy).

approaches and methods [43–45] which all report the indirect band gap dependence on Ge concentration  $x$ . The gap extension, as reported in fig. 1.4, has a drastic change in its behavior around Ge concentrations of  $x = 0.85$ . For lower concentrations the conduction band minimum is located at the  $\Delta$  point as happens in Si, and the alloy is therefore said to be *Si-like*. For higher concentrations, instead, the conduction band minimum is located at L point and the alloy is *Ge-like*. The energy gap dependence on the Ge concentration is described by the following empiric relation, valid at a temperature of  $T = 4.2$  K:

$$\begin{aligned} E_g^\Delta(x) &= 1.155 - 0.43x + 0.206x^2 & \text{if } 0 < x < 0.85 \\ E_g^L(x) &= 2.01 - 1.27x & \text{if } 0.85 < x < 1 \end{aligned} \quad (1.1)$$

With the help of the information reported above it is possible to realize artificial bi-dimensional structures featuring many different layers made of different SiGe alloy compositions. This kind of structure is called *heterostructure* and exhibits properties that can be set by design. In particular, as it will be discussed later, it is possible to grow adjacent layers with different band gap, in order to confine the conduction band electrons in the layer with lower conduction band minimum, surrounded by layers with higher conduction band minimum. Bi-dimensional heterostructures of III-V semiconductor compounds are now an established technology employed in many fields, e.g. in quantum cascade lasers (QCL). On the contrary, the realization of similar heterostructures in group-IV semiconductors with high Ge content is a challenging task still in its seminal stage mainly because of the growth problems discussed in the next section.

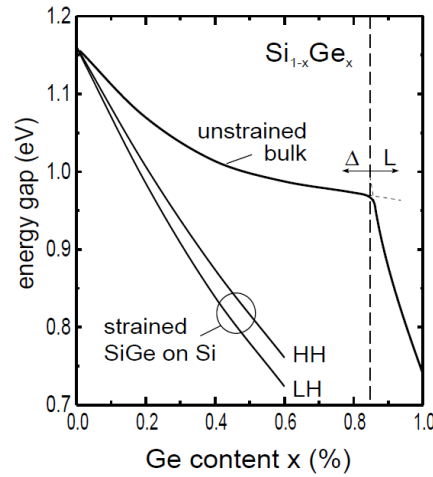


Figure 1.4: SiGe alloys band gap energy as a function of Ge content [46].

## 1.2 Strain and dislocations

The crucial element in the deposition of a Ge *epilayer* on Si, i.e. the deposition of a thin planar layer of Ge over a massive substrate of Si, is the interface behavior dictated by the different lattice parameter in the two materials. In fact, the atomic

distance in the Si lattice is  $a_{Si} = 5.431 \text{ \AA}$  while in the Ge lattice it is equal to  $a_{Ge} = 5.658 \text{ \AA}$ . These values lead to a lattice mismatch in the interface plane of [9]

$$f = \frac{|a_{Si} - a_{Ge}|}{a_{Si}} = 4.2\% \quad (1.2)$$

This value of  $f$  is very high compared to the lattice mismatch in common III-V materials ( $<1\%$ ) and generates growth limitations. Instead of pure materials Si and Ge, the mismatch is reduced if  $\text{Si}_{1-x}\text{Ge}_x$  alloys are employed, in which the lattice parameter can be estimated via the Vegard law [47]:

$$a_{SiGe}(x) = (1 - x)a_{Si} + xa_{Ge} + bx(1 - x) \quad (1.3)$$

where  $b = -0.021 \text{ \AA}$  [48].

In order to realize a SiGe heterostructure on a Si(100) substrate to be compatible with the mainstream microelectronic technology already established, the layer to grow on top of it should be carefully chosen. In fact, the deposited epilayer is subject to an elastic stress field described by the 6 components of the stress tensor  $\boldsymbol{\sigma} = (\sigma_{xx}, \sigma_{yy}, \sigma_{zz}, \sigma_{yz}, \sigma_{zx}, \sigma_{xy})$ , where  $\sigma_{ii}$  and  $\sigma_{ij}$  represent the normal and shear components, respectively. The stress is generated by the lattice mismatch of the two materials at the interface and results in the epilayer lattice deformation described by the strain tensor  $\boldsymbol{\epsilon} = (\epsilon_{xx}, \epsilon_{yy}, \epsilon_{zz}, \epsilon_{yz}, \epsilon_{zx}, \epsilon_{xy})$  linked to the stress tensor by the Hooke's law [49]:

$$\boldsymbol{\sigma} = \mathcal{R} \cdot \boldsymbol{\epsilon} \quad (1.4)$$

where  $\mathcal{R}$  is called *stiffness matrix*. In materials with cubic symmetry like those investigated here, the above relation is highly simplified in the matrix form:

$$\begin{pmatrix} \sigma_{xx} \\ \sigma_{yy} \\ \sigma_{zz} \\ \sigma_{yz} \\ \sigma_{zx} \\ \sigma_{xy} \end{pmatrix} = \begin{pmatrix} C_{11} & C_{12} & C_{12} & 0 & 0 & 0 \\ C_{12} & C_{11} & C_{12} & 0 & 0 & 0 \\ C_{12} & C_{12} & C_{11} & 0 & 0 & 0 \\ 0 & 0 & 0 & C_{44} & 0 & 0 \\ 0 & 0 & 0 & 0 & C_{44} & 0 \\ 0 & 0 & 0 & 0 & 0 & C_{44} \end{pmatrix} \begin{pmatrix} \epsilon_{xx} \\ \epsilon_{yy} \\ \epsilon_{zz} \\ \epsilon_{yz} \\ \epsilon_{zx} \\ \epsilon_{xy} \end{pmatrix} \quad (1.5)$$

where the stiffness matrix components  $C_{ij}$  are the elastic constants of the material, reported in table 1.1 for the group-IV semiconductors employed in this work [46, 49].

If the epilayer deposition is *coherent*, i.e. with the same orientation and lattice parameter of the substrate in the interface plane, it will undergo a biaxial strain

	Si	Ge	$\text{Si}_{1-x}\text{Ge}_x$
$C_{11}$	1.675	1.315	$(1 - x)C_{11}^{Si} + xC_{11}^{Ge}$
$C_{12}$	0.650	0.494	$(1 - x)C_{12}^{Si} + xC_{12}^{Ge}$
$C_{44}$	0.796	0.683	$(1 - x)C_{44}^{Si} + xC_{44}^{Ge}$

Table 1.1: Elastic constants for Si, Ge and SiGe alloys, expressed in Mbar.



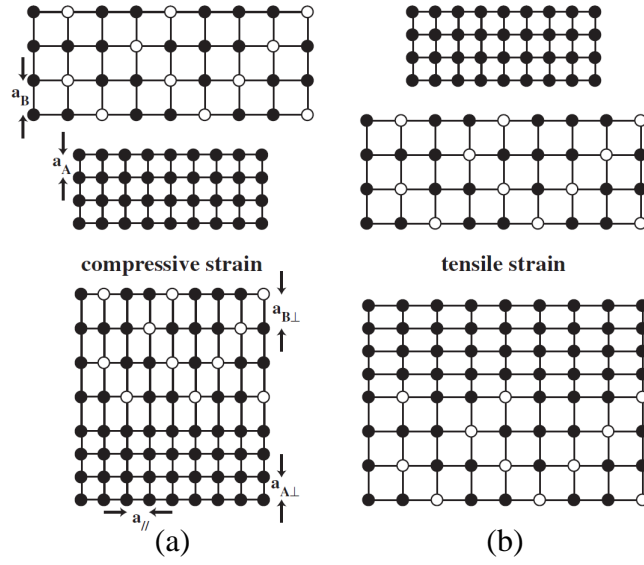


Figure 1.5: Examples of lattice deformation of an epilayer with higher (a) and lower (b) lattice parameter compared to the substrate [9].

whose components are:

$$\begin{aligned} \epsilon_{xx} = \epsilon_{yy} = \epsilon_{\parallel} &= \frac{|a_{Si} - a_{Ge}|}{a_{Si}} = f & \epsilon_{zz} = \epsilon_{\perp} &= -2\epsilon_{\parallel} \frac{C_{12}}{C_{11}} \\ \epsilon_{yz} = \epsilon_{zx} = \epsilon_{xy} &= 0 \end{aligned} \quad (1.6)$$

where the interface is set on the  $x$ – $y$  plane. The epilayer deformation is therefore tetragonal, since it does not extend only in the interface plane but also along the growth direction: a compressive (tensile) strain in the interface plane results in a compression (tension) in the plane and in a tension (compression) in the growth direction. An example of strained structures is shown in fig. 1.5.

The strain components parallel and normal to the interface plane are generally expressed by the mean of the *Poisson modulus*  $\nu$ , according to the relation [9]

$$\epsilon_{\perp} = -\frac{2\nu}{1-\nu}f \quad (1.7)$$

where the identity  $\epsilon_{\parallel} = f$  of equation 1.6 has been used. The energy density per unit volume stored in the system is set by the product between stress and strain, from which it is possible to obtain the stored energy per unit area as a function of the epilayer thickness  $h$ :

$$E_{strain}(h) = \left( C_{11} + C_{12} - 2\frac{C_{12}^2}{C_{11}} \right) f^2 h \quad (1.8)$$

Introducing the *shear modulus*  $G$ , the stored energy can be also expressed in terms of the Poisson modulus [50]:

$$\begin{cases} G = \left( \frac{C_{11} - C_{12}}{2} \right) \\ \nu = \left( \frac{C_{12}}{C_{11} + C_{12}} \right) \end{cases} \Rightarrow E_{strain}(h) = 2G \frac{1+\nu}{1-\nu} f^2 h \quad (1.9)$$

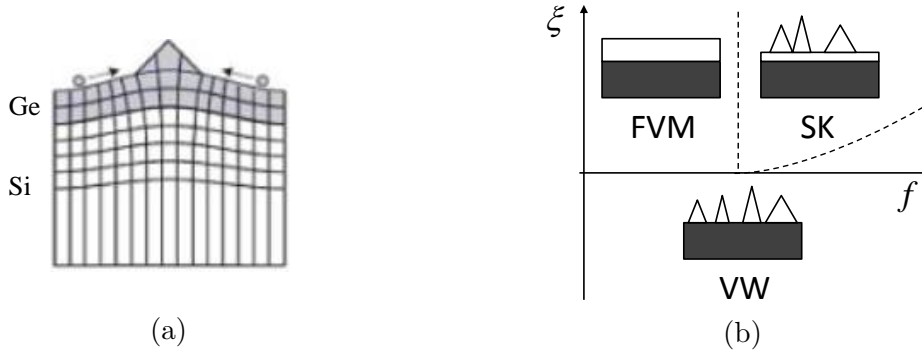


Figure 1.6: (a) Elastic relaxation with islands in the epilayer. (b) Bauer classification scheme as a function of the adhesion coefficient  $\xi$  and lattice mismatch  $f$ . The three regions corresponding to the 3 growth regimes are separated by dashed lines.

From the obtained relations follows the important conclusion that the stored energy increases with the thickness of the deposited layer. Therefore, during a deposition process the energy can be relaxed if a critical thickness is reached. The relaxations processes can be categorized in two groups: elastic relaxation and plastic relaxation. In the first case, the relaxation generates three-dimensional aggregates, while punctual defects are introduced in the lattice if plastic relaxation processes occurs.

## Elastic relaxation

The stored energy in the epilayer caused by the stress at the interface can relax elastically by deformations on lattice planes which evolve in three-dimensional structures called *islands*. The mechanism lowers the elastic energy at the expense of the epilayer surface energy whose increase follows the increase of area, as depicted in fig. 1.6(a).

At thermodynamic equilibrium the Bauer classification [51] identifies three different growth mechanisms if lattice mismatch is present, starting from the surface tension of the substrate  $\gamma_s$  and of the epilayer  $\gamma_e$ . The deposition of the epilayer can thus occur in three different regimes basing on the value of the mismatch  $f$  and of the adhesion coefficient  $\xi = (\gamma_s - \gamma_e)/\gamma_s$ , which are:

$\xi > 0$ , small  $f$  :

The growth process is called *Frank-Van der Merwe* [52] and it is an *epitaxial* (layer-by-layer) deposition that lasts until the critical thickness  $h_c$  is reached.

$\xi < 0$  :

The growth process is called *Volmer-Weber* [53] and it is characterized by the formation of islands in the epilayer. The islands can undergo plastic relaxation if a critical volume is reached. This growth regime can be established also for  $\xi > 0$ , provided a very high value of  $f$ .

$\xi > 0$ , high  $f$  :

The growth process is called *Stranski-Krastanov* [54] and the deposition follows an intermediate regime starting with a number of planar layers on top of which the islands growth is established.

In fig. 1.6(b) a scheme of the three growth regimes is sketched.

In realizing  $\text{Si}_{1-y}\text{Ge}_y/\text{Si}_{1-x}\text{Ge}_x$  heterostructures the deposition regime mainly depends on the difference between  $x$  and  $y$ . If the concentration  $y$  of the growing layer is too high compared to concentration  $x$  of the underlying layer, the Stranski-Krastanov regime is fostered, while the deposition tends to be planar (Frank-Van der Merwe) when the difference in concentrations decreases enough. As it will be discussed later, growing adjacent layer of similar Ge concentration is the key to realize defect-free heterostructures. Relative concentration is not the only parameter that sets the deposition results, since the growth thermodynamic conditions are also crucial. In fact, the experimental conditions in which the sample realization will be performed are far from the equilibrium, in order to favor a planar layer-by-layer growth.

## Plastic relaxation

The plastic relaxation of the stored energy introduces defects in the lattice called *dislocations*, which allow the epilayer to grow with its own lattice parameter as depicted in fig. 1.7. The presence of dislocations could have serious impact on the entire structure, since they are able to propagate through several layers with detrimental effects on the physical properties of the sample. In particular, the atomic vacancies at the interface, called *misfit dislocations*, could interact with each other losing their punctual nature and generating an extended defect through the lattice. The aligned missing atoms chain, called *threading dislocation*, does not only influences the optical and electric properties of the system, being electrically active, but also increases the surface roughness of the structure.

The stored elastic energy obtained in equations 1.8 and 1.9 as a function of the epilayer thickness  $h$  has to be compared with the minimum energy required to generate a dislocation in the lattice. Comparing the two quantities it is possible to extract the behavior of the critical thickness  $h_c$ , i.e. the maximum thickness allowed for a coherent deposition. The energy  $E_D$  required to generate a dislocation depends on the dislocation type and, in a cubic lattice as in SiGe alloys, it refers to the introduction of a screw dislocation [50]:

$$E_D \sim \frac{b^2}{a_e} \ln \left( \frac{h}{b} \right) \quad (1.10)$$

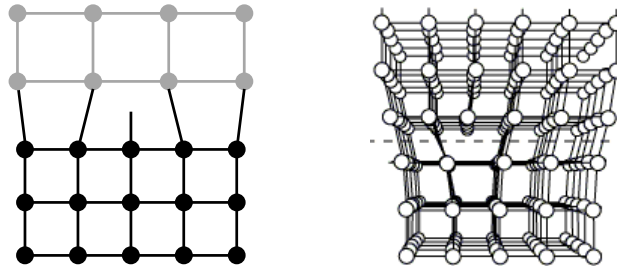


Figure 1.7: Formation of a threading dislocation at the interface between two materials with different lattice parameter.

where  $b$  is the length of the *Burger's vector*, which represents the dislocation amplitude and direction. The dislocation is created inside the lattice when the condition  $E_{strain}(h = h_c) = E_D$  is reached and, considering the corresponding relations, it is therefore possible to obtain the behavior of the critical thickness [50, 55]:

$$h_c \sim \left( \frac{1 - \nu}{1 + \nu} \right) \left( \frac{b^2}{a_e} \right) \left( \frac{1}{f^2} \right) \ln \left( \frac{h_c}{b} \right) \quad (1.11)$$

Many studies have been performed on the estimation of the critical thickness in the case of a  $\text{Si}_{1-x}\text{Ge}_x$  layer deposited on a Si substrate, as reported in the example of fig. 1.8 [5]. A common result is that for Ge concentrations above 80% the critical thickness is of few nanometers, even if higher thickness due to metastable growing conditions have been reported [9]. Such low values of critical thickness limit too much the realization of heterostructures suitable for applications, but some countermeasures can be taken. In fact, in order to deposit a Ge layer of thickness up to 40 nm avoiding relaxation, it needs to be grown on top of a  $\text{Si}_{1-x}\text{Ge}_x$  substrate with high Ge concentration  $x$  around 0.8, as clear from fig. 1.8. Further more, the realization of a system with many layers can be achieved employing the *strain-compensated* structures depicted in fig. 1.9, in which the stress contributions in each layer compensate with each other and the total elastic stress vanishes. In fact, interchanging layers with opposite deformation should theoretically results in a null mean strain along the structure, or at least can drastically limit the dislocation generation. This strategy is often used to grow structures with many layers ( $>100$ ) and it will be therefore employed also in the realization of the samples investigated in the present work.

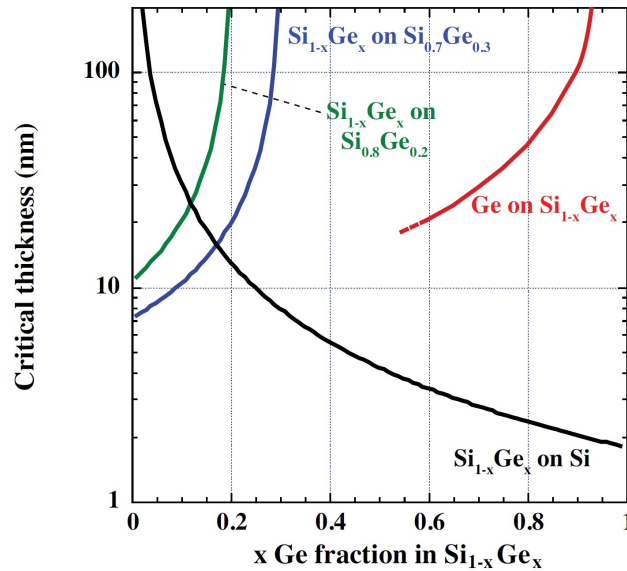


Figure 1.8: Critical thickness behavior in different  $\text{Si}_{1-y}\text{Ge}_y/\text{Si}_{1-x}\text{Ge}_x$  heterostructures as a function of the Ge content  $x$ .

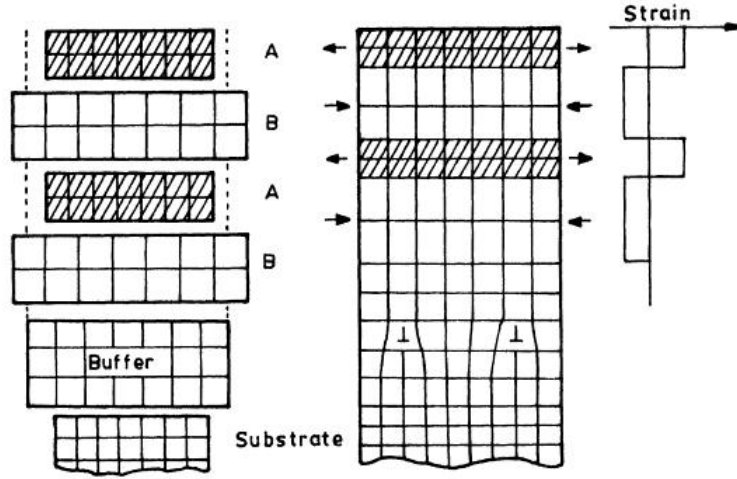


Figure 1.9: Example of a strain-compensated structure.

### 1.2.1 Strain effect on the electronic properties

The electronic properties of a solid material strongly depend on the crystalline structure. Therefore, the discussed lattice deformations directly influence the band structure and the corresponding electronic states. To easily investigate the effects of a  $\text{Si}_{1-x}\text{Ge}_x$  layer deformations on the electronic properties it is convenient to separate the strain in the two components *hydrostatic*  $\epsilon_{hyd}$  and *uniaxial*  $\epsilon_{uni}$ . The former is related to the isotropic variation of the unit cell volume, while the latter relates to the asymmetric variations:

$$\begin{aligned}\epsilon_{hyd} &= (2\epsilon_{\parallel} + \epsilon_{\perp}) = \frac{\Delta V}{V} \\ \epsilon_{uni} &= (\epsilon_{\perp} - \epsilon_{\parallel})\end{aligned}\tag{1.12}$$

Focusing on the conduction band since it is the band in which the heterostructures properties will be investigated, the hydrostatic component of the strain generates a level shift of:

$$\Delta E_{hyd} = \delta_c \frac{\Delta V}{V} = \delta_c (2\epsilon_{\parallel} + \epsilon_{\perp})\tag{1.13}$$

where  $\delta_c$  is the hydrostatic deformation potential in the conduction band, which values are 1.72 eV and -2.78 eV for Si at  $\Delta$  point and Ge at L point, respectively [46].

The uniaxial strain has no effect on the conduction band minimum at L point along the [111] direction, while partially lifts the 6-fold degeneracy of the valley at  $\Delta$  point. The two obtained levels  $\Delta_2$  and  $\Delta_4$ , with degeneracy 2 and 4 respectively, are shifted in energy considering the following values [12]:

$$\Delta E_u = \begin{cases} \frac{2}{3}\Theta_{\Delta}(\epsilon_{\perp} - \epsilon_{\parallel}) & \text{for } \Delta_2 \\ -\frac{1}{3}\Theta_{\Delta}(\epsilon_{\perp} - \epsilon_{\parallel}) & \text{for } \Delta_4 \end{cases}\tag{1.14}$$

where  $\Theta_{\Delta} = 9.16$  eV is the uniaxial deformation potential in the Si conduction band at  $\Delta$  point. The total strain effect on  $\Delta$  valleys is reported in fig. 1.10 for both tensile

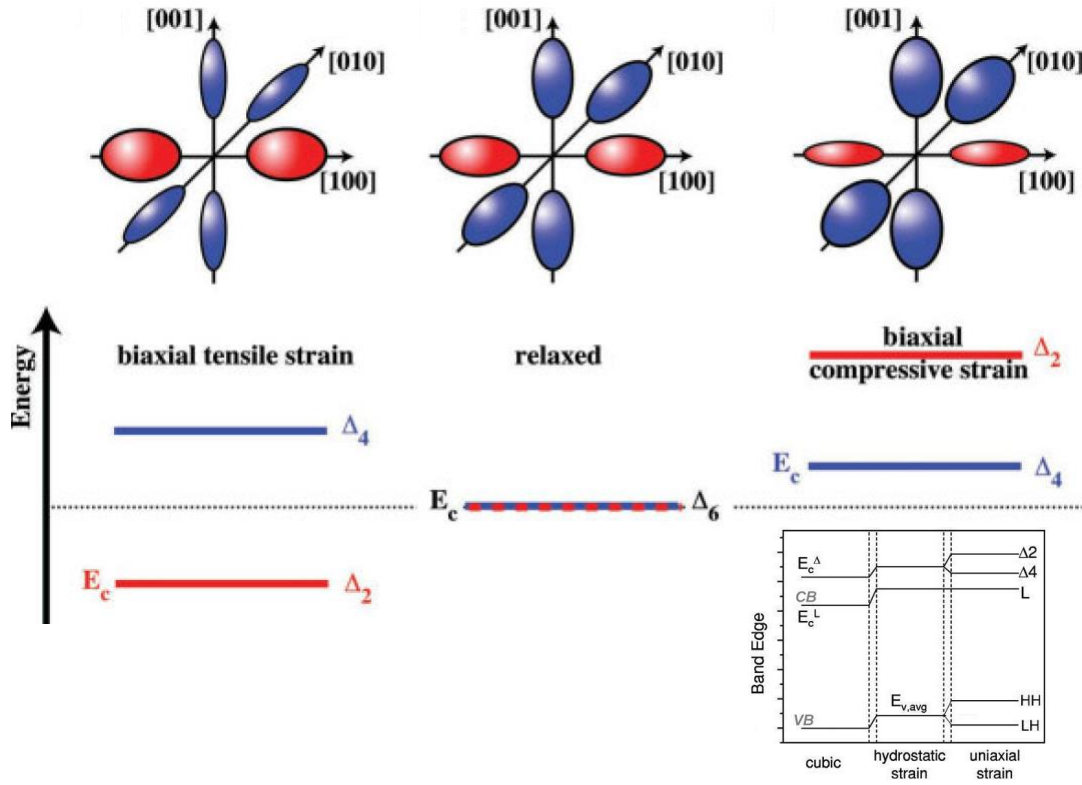


Figure 1.10:  $\text{Si}_{1-x}\text{Ge}_x$  conduction band edge shift at  $\Delta$  point as effect of tensile and compressive strain compared to the relaxed case. The inset shows the effect of the total strains on the averaged valence bands (VB) and conduction band (CB) [12].

and compressive strain together with the direction-dependent valley structure [5]. A similar discussion can be carried also for the valence band, leading to similar results shown in the inset of fig. 1.10, where the maximum of the valence band and the minimum of the conduction band are considered.

### 1.3 Band alignment in SiGe heterostructures

The properties of SiGe alloys discussed so far can be exploited in realizing heterostructures suitable for the implementation in opto-electronic devices. In fact, by choosing the proper layer compositions it is possible to obtain a band alignment producing regions in which the allowed states in one material layer are confined by the band gap of the adjacent ones. The resulting artificial structure is called *quantum well*. A quantum well (QW) is therefore a potential well inside a material delimited by the energy gap of another material, in which the electronic allowed states become discrete if the well is thin enough. The thinner is the well the higher is the energy level separation, allowing to set the desired transition energies by design, simply varying the layer thickness. Depending on the chosen materials, the band alignment can generate three different QW configurations, as depicted in fig. 1.11.

The band alignment of a SiGe heterostructure is determined by the Ge concentrations  $y$  and  $x$  in the adjacent layers  $\text{Si}_{1-y}\text{Ge}_y$  and  $\text{Si}_{1-x}\text{Ge}_x$ , which not only set the

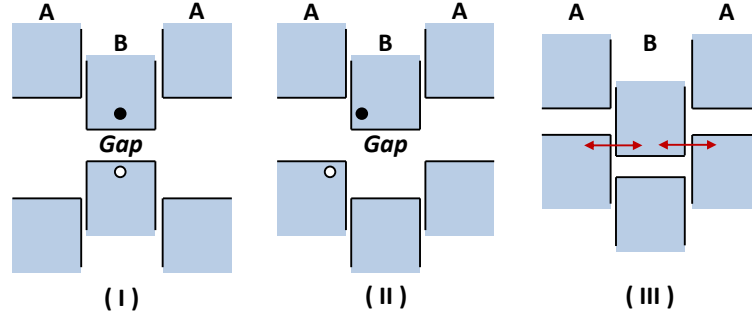


Figure 1.11: Possible band alignments. Type I: QW for both electrons and holes; type II: QW for electrons in material B and holes in material A; type III: direct channel between valence band in material A and conduction band in material B.

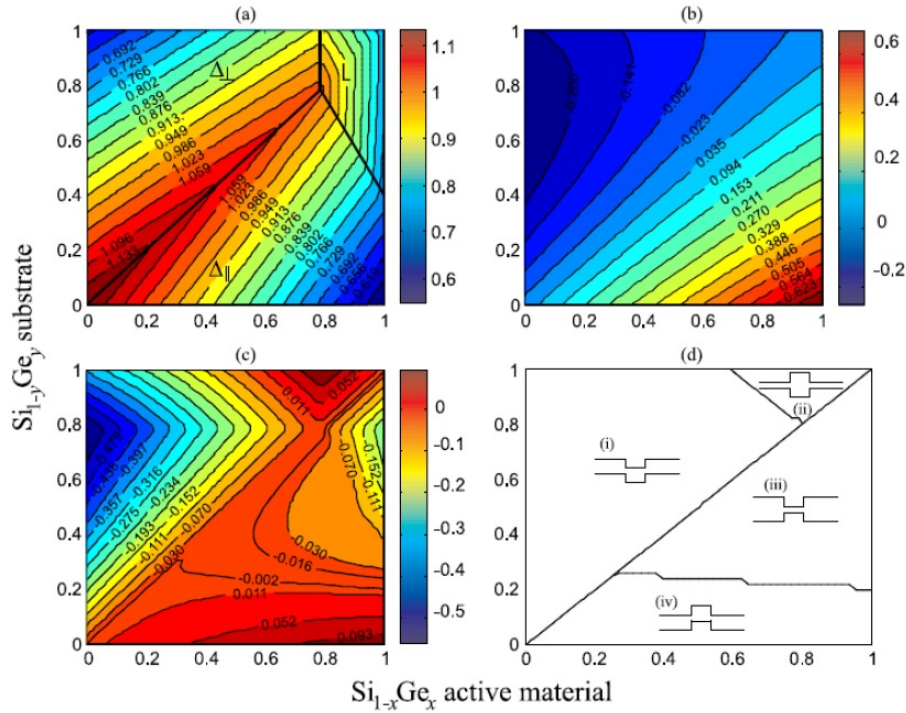


Figure 1.12: Band alignment properties of  $\text{Si}_{1-x}\text{Ge}_x/\text{Si}_{1-y}\text{Ge}_y$  heterostructure as a function of  $x$  and  $y$ : (a) band gap, band offset in (b) valence and (c) conduction band, and (d) resulting band profile.

energy gap values in the two materials but also define if the alloy is Ge-like with the conduction band minimum at L point, or Si-like with the conduction band minimum at  $\Delta$  point as discussed in section 1.1. How these properties vary as a function of the Ge concentration of a  $\text{Si}_{1-x}\text{Ge}_x$  epilayer grown on a  $\text{Si}_{1-y}\text{Ge}_y$  substrate has been extensively studied in reference [32], whose results are reported in fig. 1.12.

The choice of the correct concentrations is dictated by the final goal to achieve. In the case of the present work, the SiGe heterostructure to grow must meet the requirements for the realization of n-type opto-electronic devices in the THz range. This implies a conduction band offset  $\geq 100$  meV, which falls in the yellow-green region of the plot in fig. 1.12(c). Considering the limitations imposed by the strain



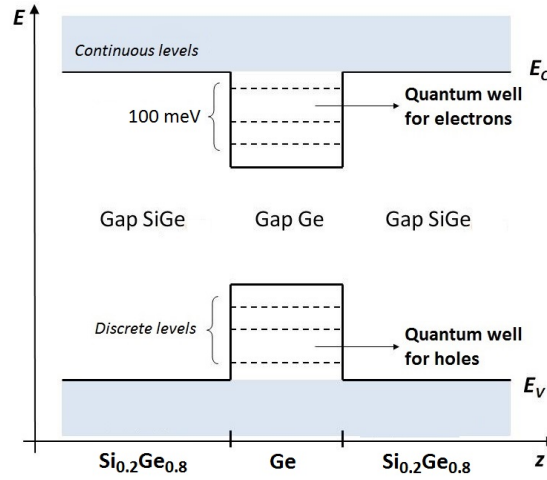


Figure 1.13: Type I band alignment in a Ge/ $\text{Si}_{0.2}\text{Ge}_{0.8}$  quantum well.  $E_c$  and  $E_v$  denote the conduction and valence band edge profile in the heterostructure along  $z$ .

discussed in the previous section, a proper QW system in SiGe alloys can be realized in two ways: the first one is employing QWs of pure Si ( $x = 0$ ) grown on a  $\text{Si}_{1-y}\text{Ge}_y$  substrate with Ge concentration  $y > 0.1$ , while the second one considers QWs of pure Ge ( $x = 1$ ) grown on a  $\text{Si}_{1-y}\text{Ge}_y$  substrate with high Ge concentration around 80%. The previous approach has been already investigated [31, 56], studying the properties of Si QWs confined between SiGe barriers with low Ge concentration in order to limit the lattice mismatch at the interface. This kind of system is not the best option for opto-electronic devices because of the low optical transition rate between energy levels in the Si conduction band, as it will be discussed later. On the contrary, Ge QWs feature high transition rate and better performances as discussed in the introduction, and this is the main reason why the samples investigated in this work of thesis consist in Ge/SiGe heterostructures, with band alignment of type I. A sketch of the resulting heterostructure is shown in fig. 1.13, in which the bottom of the conduction band  $E_c$  and the top of the valence band  $E_v$  generate a band profile with a QW both in the conduction and valence bands of Ge, confined by the larger energy gap of the SiGe layers. If the Ge layer is thin enough, the electrons are arranged in discrete levels within the QW and in a bulk-like continuous configuration outside. The discrete levels inside the well are called *subbands*, because they are confined only along the growth direction  $z$ . In fact, in the normal plane ( $x-y$ ) they are free to move in the layer like plane waves and their states are indeed bands with a proper dispersion. They are called *subbands* because they are formed inside the conduction (or valence) band.

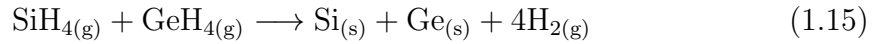
The main problem in realizing such systems is the need to grow Ge QWs on top of SiGe layers with high Ge concentration around 80%. Because of the high lattice mismatch between the  $\text{Si}_{1-x}\text{Ge}_x$  alloys with high  $x$  values and the Si(100) substrates bounded by the microelectronics industry, it is necessary to employ a *virtual substrate* as a linking layer between the QW heterostructure and the Si substrate. With this strategy it is possible to distribute the lattice mismatch among the virtual substrate thickness and obtain a final QW system with low defect density.



## 1.4 SiGe heterostructures growth techniques

The two main techniques that allow to obtain abrupt interfaces on the atomic scale, as required in structures made of different layers of few nanometers, are the Molecular Beam Epitaxy (MBE) and the Chemical Vapor Deposition (CVD). The MBE technique consists in generating a particle beam by heating the solid rough material beyond its melting point, allowing the emitted particles to reach and adhere to the substrate surface while cooling down on the way. The resulting samples grown with this technique are of high quality, although their realization requires a large amount of time. The CVD technique consists in a different approach, allowing the deposition starting from a molecular precursor in gaseous form. If the substrate is heated enough, the impinging molecules can be broken by the pyrolysis process, allowing the heavy components to remain deposited on the substrate surface while the light components in gaseous form can be pumped away.

In the SiGe heterostructure deposition the used gaseous precursors are silane ( $\text{SiH}_4$ ) and germane ( $\text{GeH}_4$ ). The pyrolysis process of these molecules, although including several intermediate stages, can be summarized as follows:



where (g) and (s) refer to the gaseous and solid phases. This reaction takes place on the substrate surface where reactive sites (e.g. dangling bonds) are present, with a threshold temperature around  $500^\circ\text{C}$  for silane and  $300^\circ\text{C}$  for germane. A simplified scheme of the CVD growth process employed in SiGe heterostructure realization is displayed in fig. 1.14. Several kinds of experiments require the material to be doped, a procedure that can be performed with the same CVD technique without employing any post-growth process like dopant implantation. For example, in order to populate the conduction band of the grown structure, the needed n-doping is achieved by performing a phosphine ( $\text{PH}_3$ ) co-deposition. As a result of the  $\text{PH}_3$  pyrolysis, the donor atoms of phosphorus are then uniformly distributed in the doped regions, which can be the Ge QW (direct doping) or the SiGe barrier (modulation doping).

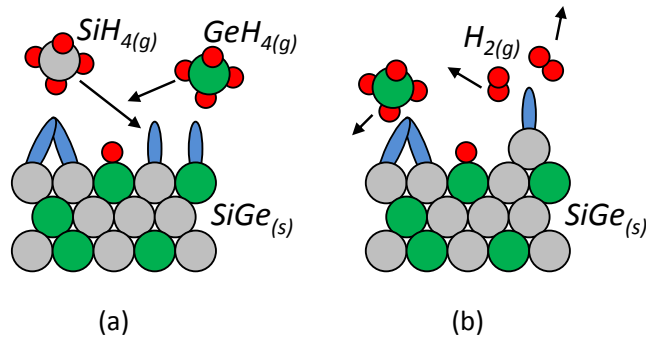


Figure 1.14: Silane and germane pyrolysis scheme: gaseous precursors impinge the heated sample (a) and the heavy atoms remain on the surface while the gaseous hydrogen is pumped away (b). The Si atoms are depicted in grey, the Ge atoms in green, the hydrogen atoms in red and the dangling bonds in blue.

Even if the first employed technique for Si-based structures deposition was the MBE, nowadays the CVD is the dominant one because of the final goal of this field of research. In fact, the scientific interest in these materials meets the technological one, which aims at a large scale and efficient production of electronic and opto-electronic devices and thus requires an affordable, reliable and fast enough growth process to be employed in the industrial production. In this regard, the CVD technique is favorite over the MBE because it allows sample realization in a relative small amount of time, compatible with a production approach at large scale. For example, a typical sample investigated in this work of thesis requires around 10 hours to be completed, far less than what is needed to obtain similar results with the MBE technique. In the case of SiGe material, the CVD technique allows for depositions compatible with the production processes and the grown structures are of high quality, featuring interfaces with sub-nanometer precision. These abrupt interfaces are obtained also with the help of the hydrogen present in the growth chamber as a product of the pyrolysis, since it reduces the Ge atoms segregation. All the samples investigated in the present work are grown by CVD.

#### 1.4.1 Virtual substrates

The high lattice mismatch between the Si substrate and the SiGe heterostructure with high Ge content imposes the realization of a virtual substrate between them, as already introduced. With the employment of this intermediate buffer the large amount of lattice defects is confined in the lower layers as they can not propagate up through the whole structure. In fact, the threading dislocations generated by the lattice mismatch of the virtual substrate with the Si substrate are blocked by the several inner interfaces between the layers the virtual substrate is made of, resulting in a low defect density in the final layers on top of which the QW heterostructure can be grown. In other words, the virtual substrate collects a high density of defects but allows to reach high Ge concentration suitable for the desired SiGe heterostructure deposition.

The first approach employed in virtual substrates growth was called *linear graded* [56], which consists in the deposition of several different layers with increasing Ge concentration, from the pure Si up to the  $\text{Si}_{1-x}\text{Ge}_x$  layer with the desired concentration  $x$ . This technique allows to distribute the total lattice mismatch existing between Si and  $\text{Si}_{1-x}\text{Ge}_x$  among many layer interfaces with low mismatch, resulting in structures with low final defect density at the expense of surface roughness, which increases with the virtual substrate thickness. With the help of thermal, chemical and mechanical treatments it is possible to lower the surface roughness [57], but these procedures are time-consuming and quite expensive, therefore not compatible with an affordable large scale production. In addition, the virtual substrate layers needed to reach a  $\text{Si}_{1-x}\text{Ge}_x$  layer with high Ge content around 80% are so many to imply a long growth process and a huge amount of material needed for the deposition.

Recently, a different approach has been employed in the realization of SiGe virtual substrates with high Ge content, which allows to overcome the problems arisen with the linear graded approach. The technique is called *reverse graded* [58] and consists in the deposition of an initial Ge layer directly on the Si substrate,

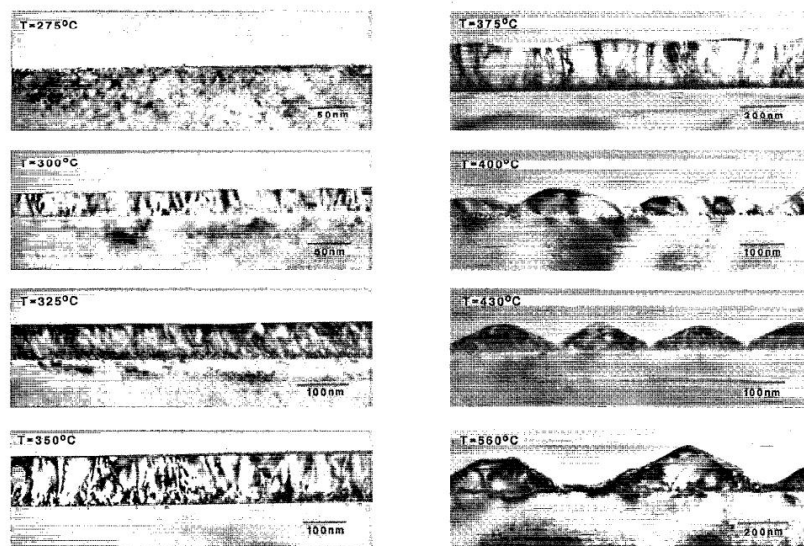


Figure 1.15: Transmission electron microscopy images of Ge layers on Si substrate at different growth temperatures [59].

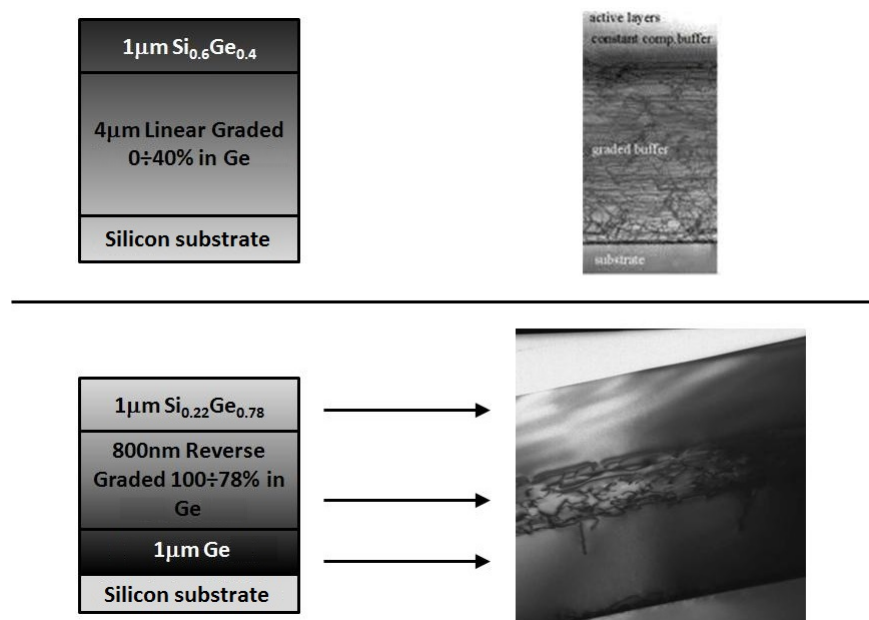


Figure 1.16: Comparison between TEM images of linear graded (top) and reverse graded (bottom) virtual substrates.

which of course will be rich in lattice defects due to the high mismatch. Since a Ge layer tends to grow on Si in the Stranski-Krastanov regime (i.e. with the formation of islands) it is necessary to start the Ge growth at low temperature, in order to keep the system out of thermodynamic equilibrium. However, too low temperatures prevent the germane pyrolysis and thus the growth itself. Figure 1.15 displays different results of Ge deposition on Si obtained at different temperatures with the CVD technique: under 300°C the pyrolysis does not take place and a null Ge thickness is present, while above 375°C the islands formation starts and the surface appears corrugated. The allowed temperature interval for an epitaxial deposition of Ge on Si substrates is therefore 300°C-375°C.

Once the best temperature for the deposition is identified, it is possible to grow the first thin layer of Ge, called *seed layer*, which will exhibit a high defect density and thus a poor crystalline quality. However, at the same time, it will allow for a consecutive epitaxial deposition of another Ge layer at higher temperature, characterized by a higher growth speed, relaxation and crystalline quality [60]. With this multi-temperature approach it is possible to grow Ge layers up to around 1  $\mu\text{m}$ , with defects confined mostly in the seed layer [47]. The employment of this thick Ge layer does not require a large number of subsequent layers to reach the final one with the desired Ge concentration, because it is sufficient to increase the Si content (and not the Ge content as in the linear graded approach) until the final high Ge-rich  $\text{Si}_{1-x}\text{Ge}_x$  composition is reached. This procedure limits the number of layer required, the deposition time and the surface roughness. In fig. 1.16 the images taken with the transmission electron microscope (TEM) show the example of two virtual substrates obtained with the linear and reverse graded approach, respectively [61]. In the case of linear graded approach the virtual substrate is rich in defects and requires a high thickness of around 5  $\mu\text{m}$  to reach only 40% of Ge concentration. On the contrary, the reverse graded approach allows to reach 78% of Ge concentration in much less thickness, with defects localized away from the final layer.

## 2

# Inter-subband transitions in quantum wells

In the previous chapter the properties of the group-IV semiconductor alloys employed in this work have been analyzed in detail, showing how the current technology enables a high-quality material growth on the microelectronic platform. In the present chapter, instead, it will be presented how the peculiar properties of a quantum well can be exploited to obtain engineered electronic transitions and eventually achieve radiative emission at the desired frequency, e.g. in the THz band.

## 2.1 Quantum wells properties

After discussing the possible band alignment of the heterostructures of interest, we now consider the general case of a single QW in the conduction band. In order to determine the energies and wavefunctions of the states confined within a QW characterized by a conduction band edge profile  $V_0(z)$  like the one shown in fig. 2.1, the effective mass approximation and the envelope function approach can be used. In this frame, it is possible to write the electron wavefunction in the well as [42]:

$$\varphi(\mathbf{r}) \simeq \sum_{k \simeq k_0} c_n(k) e^{i\mathbf{k} \cdot \mathbf{r}} u_{c,k_0}(\mathbf{r}) = u_{c,k_0}(\mathbf{r}) \psi(\mathbf{r}) \quad (2.1)$$

where  $\mathbf{k}_0$  is the crystalline wavevector at the minimum of the conduction band.  $\psi(\mathbf{r})$  is called *envelope function* and  $u_{c,k_0}(\mathbf{r})$  is a periodic function of the same form of the Bloch waves. This Bloch term  $u_{c,k_0}(\mathbf{r})$  is related to the bulk material, with the index  $c$  denoting the conduction band, while the envelope functions  $\psi(\mathbf{r})$  are directly related to the different levels (subbands) inside the well. As a matter of fact, the envelope function satisfies the following Schrödinger equation:

$$\left[ \frac{p_z^2}{2m^*} + V_0(z) + \frac{p_x^2}{2m^*} + \frac{p_y^2}{2m^*} \right] \psi(\mathbf{r}) = E\psi(\mathbf{r}) \quad (2.2)$$

where  $\mathbf{p} = \hbar\mathbf{k} = (p_x, p_y, p_z)$  is the electron momentum inside the crystal,  $m^*$  the electron effective mass and  $V_0(z)$  is the conduction band edge profile of the heterostructure, that acts as a confining potential for the electrons in the well. Here it is assumed that the conduction band effective mass tensor at  $\mathbf{k}_0$  is diagonal and

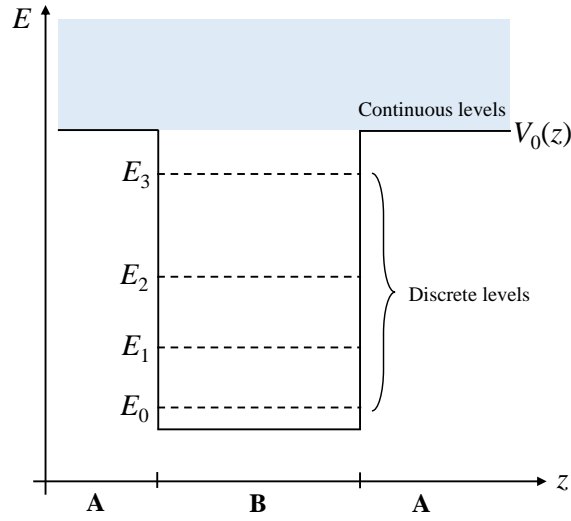


Figure 2.1: Single QW in material B confined by barriers of material A. The conduction band edge alignment  $E_c$  works as the confining potential  $V_0(z)$ .

isotropic. Moreover, it is considered not to change much in the two materials and thus is taken constant in the whole system. This approximation is found to be good enough in most cases and it will be considered valid from now on. The same argument stands for the Bloch terms  $u_{c,k_0}(\mathbf{r})$ , assumed to be the same for both materials A and B.

As introduced above, the confinement in the  $z$ -direction implies that the electrons are free to move in the  $(x-y)$  plane and thus their wavefunction can be factorized in two terms: one depending on the confining direction  $z$  and one plane wave term in the normal plane  $\mathbf{r}_\perp$ , becoming

$$\psi(\mathbf{r}) = \psi(z)e^{i\mathbf{k}_\perp \cdot \mathbf{r}_\perp} \quad (2.3)$$

where  $\psi(z)$  satisfies

$$\left[ \frac{p_z^2}{2m^*} + V_0(z) \right] \psi(z) = \left( E - \frac{\hbar^2 k_\perp^2}{2m^*} \right) \psi(z) = E_n \psi(z) \quad (2.4)$$

In a bi-dimensional system the energy dispersion is therefore

$$E = E_n + \frac{\hbar^2 k_\perp^2}{2m^*} \quad (2.5)$$

where  $E_n$  are the energy levels depicted in fig. 2.1 and the term  $k_\perp^2$  refers to the parabolic dispersion in the  $(x-y)$  plane. The obtained electron energy structure is sketched in fig. 2.2.

The resolution of the above Schrödinger equation depends on the shape of  $V_0(z)$ . In the following, wavefunctions and energies in the two cases of infinite and finite well are discussed.

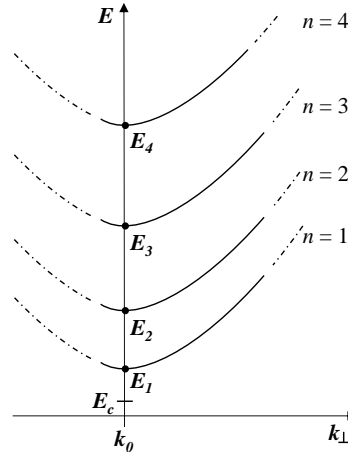


Figure 2.2: Subband energy dispersion in the growth plane.

## Infinite potential well

The only case in which analytic solutions can be obtained is the infinite quantum well, delimited by two infinite potential barriers at  $z = 0$  and  $z = d_w$ . If null potential is assumed inside the well, the Schrödinger equation to be solved is of this simple form:

$$-\frac{\hbar^2}{2m^*} \frac{d^2}{dz^2} \psi(z) = E \psi(z) \quad \Rightarrow \quad \frac{d^2}{dz^2} \psi(z) = -\frac{2m^* E}{\hbar^2} \psi(z) = -k^2 \psi(z) \quad (2.6)$$

and the solutions are plane waves:

$$\psi(z) = A e^{ikz} + B e^{-ikz} \quad (2.7)$$

Outside the well, the wavefunctions are of course zero because of the infinite potential, thus the solutions  $\psi(z)$  inside the well have to satisfy these boundary conditions at  $z = 0$  and  $z = d_w$ . Applying the first one allows to reduce the number of unknown coefficients:

$$\psi(0) = 0 \quad \Rightarrow \quad A + B = 0 \quad \Rightarrow \quad B = -A \quad (2.8)$$

The eigenfunctions inside the wells are then:

$$\psi(z) = A (e^{ikz} - e^{-ikz}) = 2iA \sin(kz) \quad (2.9)$$

Applying the boundary condition at  $z = d_w$ , instead, we get:

$$\psi(d_w) = 0 \quad \Rightarrow \quad \sin(kd_w) = 0 \quad \Rightarrow \quad kd_w = n\pi \quad (2.10)$$

with  $n \in \mathbb{N}$  starting from 1. The solutions of the Schrödinger equation for an infinite QW can therefore be obtained analytically and they are of the sinusoidal form

$$\psi_n(z) \sim \sin\left(\frac{n\pi}{d_w} z\right) \quad (2.11)$$

whose corresponding energies are

$$E_n = \frac{\hbar^2 \pi^2}{2m^* d_w^2} n^2 \quad (2.12)$$

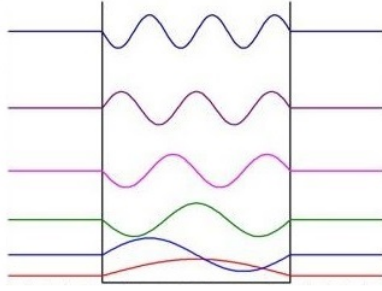


Figure 2.3: Solutions of the Schrödinger equation for an infinite potential well.

The first property of a QW is therefore that the level energies are higher when the well is thinner, with a quadratic dependence on  $d_w$ . Moreover, the relative distance of the obtained levels increases with the energy (increasing  $n$ ), as depicted in fig. 2.3, and their wavefunctions have even and odd symmetry, alternatively. Since the eigenfunctions with even  $n$  have an odd symmetry (and vice versa), the energy levels are usually denoted with the index  $l = n - 1$ , with corresponding energies

$$E_l = \frac{\hbar^2 \pi^2}{2m^* d_w^2} (l + 1)^2 \quad (2.13)$$

with  $l$  starting from 0. In this way, the ground level  $\psi_0$  has an even symmetry, the first excited level  $\psi_1$  has an odd symmetry, and so on. This is the only notation that will be used within the present work.

## Finite potential well

When the QW is delimited by two finite potential barriers of height  $V_0$ , the solutions of the Schrödinger equation cannot be obtained analytically and different methods have to be employed. Here, a simple graphic method is discussed starting from the same wavefunctions with the plane wave form of equation 2.7. In this case, the wavefunctions are not null outside the well because the potential is not infinite there, but they anyway have to fulfill the continuity conditions at the well edges together with their first derivatives. This procedure results in two different equations to be solved for even and odd eigenfunctions:

$$\begin{cases} \tan x = \sqrt{\frac{x_0^2}{x^2} - 1} & \text{even eigenfunctions} \\ -\cot x = \sqrt{\frac{x_0^2}{x^2} - 1} & \text{odd eigenfunctions} \end{cases} \quad (2.14)$$

where

$$x_0^2 = \frac{m^* V_0 d_w^2}{2\hbar^2} \quad (2.15)$$

The dimensionless parameter  $x = kd_w/2$  is related to the level energy by the relation  $E = \hbar^2 k^2 / 2m^*$  and it is obtained graphically by the intersection of the two curves of the equation, as shown in fig. 2.4.



In fig. 2.5 the energy behavior as a function of the well width is displayed for a given value of well dept  $V_0 = 100$  meV and compared to the infinite well energies. The energy values obtained are very different in the two cases, specially for thin wells. On the contrary, increasing the well width reduces the energy difference in the two cases of finite and infinite well, suggesting that the infinite well approximation can be applied to wide enough QWs. The validity of this approximation is of course even higher with increasing well dept.

Even if this method is generally good enough to retrieve the energy levels inside a QW, their evaluation will be performed employing more reliable numeric calculations which will be discussed later.

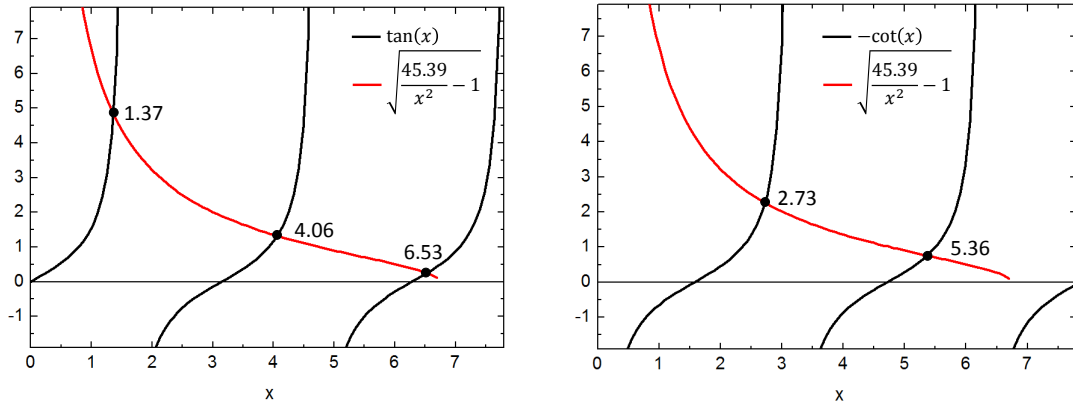


Figure 2.4: Graphic method for the solutions of the Schrödinger equation of a finite potential well of width  $d_w = 24$  nm and depth  $V_0 = 100$  meV.

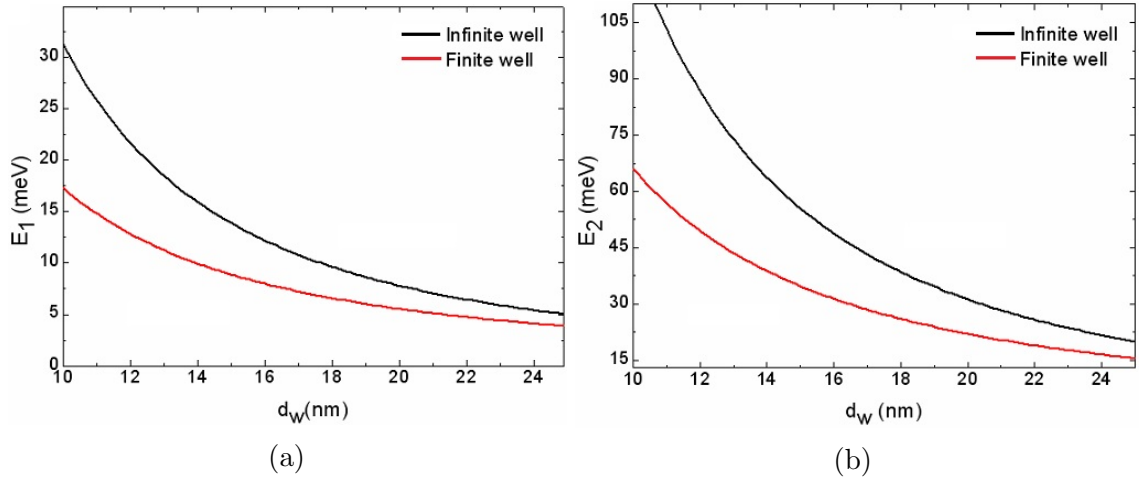


Figure 2.5: Comparison between the first (a) and second (b) level energies in the two cases of infinite and finite well as a function of the well width  $d_w$ .

## Asymmetric Coupled Quantum Wells

Two different heterostructure systems will be studied across this work of thesis. The first one is called *multi quantum well* (MQW) system and features a periodic repetition of single QWs separated by barriers thick enough to guarantee the wells are isolated from each other and hence not interacting. The second configuration that will be investigated is called *asymmetric coupled quantum well* (ACQW) system, in which every single element of the periodic repetition consists in two QWs with different width separated only by a thin barrier of few atomic layers. The two QWs cannot be therefore considered isolated anymore, because the small thickness of the barrier in the middle allows them to interact with each other. In fact, the tunneling probability through the thin barrier could be very high and the electron wavefunction of each well can extend into the adjacent one. The result is a level mixing that generates global stationary levels with energies different from the original ones associated to each single QW. In addition, the generated level wavefunctions lose the defined symmetry they would have in each well if isolated and their overlap becomes a varying parameter set by the specific structural properties. Employing a proper ACQW design, it is therefore possible to tune the optical properties of the system like, for example, the transitions probability between the subbands within the structure. This characteristic of ACQW systems results in a higher flexibility that can be exploited to finely engineer the optical properties of an eventual device. Because of the delocalized nature of the wavefunctions, the prediction on the energy levels inside an ACQW structure requires the use of numeric methods that will be discussed in chapter 4. A sketch of the ACQW configuration is displayed in fig. 2.6.

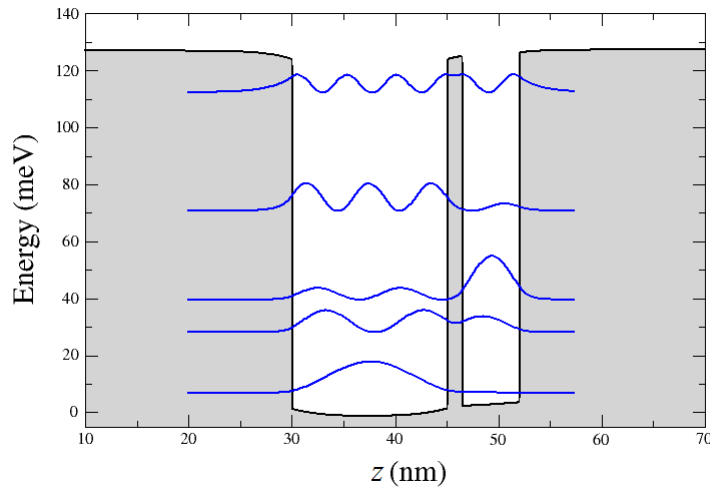


Figure 2.6: ACQW scheme. The black line indicates the conduction band profile shaping the two QWs, the thin barrier in the middle and the two thick barriers at sides. The squared modulus of the calculated wavefunctions inside the structures is reported with blue lines.

## 2.2 Inter-subband transitions

The interaction of an incident radiation with the described system can generate electron transitions inside the QW. If the transition is between an electron state in the valence band and one in the conduction band, it is called *inter-band* transition and therefore involves both the QWs for holes and electrons. When the transition involves levels inside the same well (e.g. only in the conduction band), it is instead called *inter-subband* (ISB) transition. The two types of transition are depicted in fig. 2.7.

In the semi-classical framework, in which the radiation is treated as a classic quantity while the electron system follows the rules of the quantum mechanics, the Hamiltonian  $H_{int}$  describing the interaction is

$$H_{int} \sim \frac{e}{m} A_0 \boldsymbol{\epsilon} \cdot \mathbf{p} e^{-i\omega t} + c.c. \quad (2.16)$$

where the dipole approximation is assumed valid.  $A_0$  is the amplitude of the vector potential  $\mathbf{A}$  of the radiation,  $\hbar\omega$  its energy and  $\boldsymbol{\epsilon}$  its polarization vector, directed along the electric field. With the use of the Fermi golden rule the interaction Hamiltonian leads to the following mean transition rate, as the balance between the absorption and emission rates:

$$W = W_{abs} - W_{em} \sim \frac{1}{m^2 \omega^2} \sum_{i,j} |\langle j | \boldsymbol{\epsilon} \cdot \mathbf{p} | i \rangle|^2 [\rho(E_i) - \rho(E_j)] \delta(E_j - E_i - \hbar\omega) \quad (2.17)$$

where  $|i\rangle$  and  $|j\rangle$  are the initial and final electron states involved in the transition,  $\rho(E_i)$  and  $\rho(E_j)$  the corresponding occupation functions. The Dirac delta function

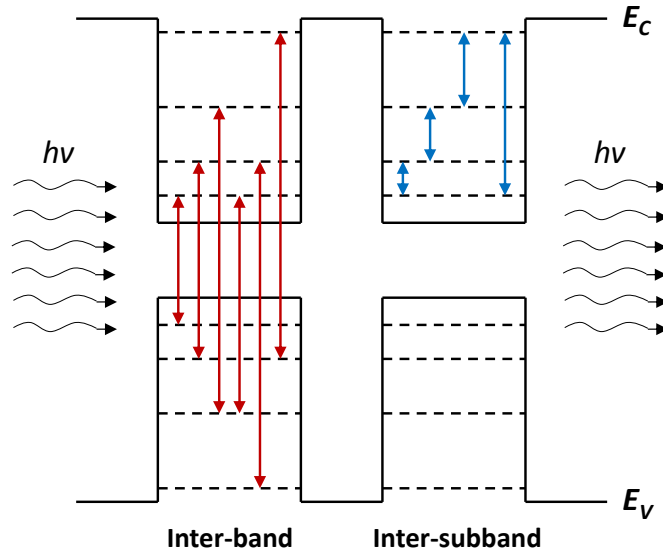


Figure 2.7: Inter-band transitions between the two bands and inter-subband transitions in the conduction band.

assures that the absorption process can take place only if the incident photon has an energy equal the energy difference of the two electron levels involved in the transition, while the occupation functions imply that the system will absorb energy from the incident radiation if at equilibrium, since  $\rho(E_i) > \rho(E_j)$ . On the other hand, if the system is out of equilibrium like in the case of a laser,  $\rho(E_j) > \rho(E_i)$  and the system can release energy to amplify an incident beam of light [42].

The matrix element  $\langle j | \boldsymbol{\epsilon} \cdot \mathbf{p} | i \rangle$  bears all the remaining information on the optical transitions and it will be therefore analyzed in detail. Recalling that the derivative operator  $\mathbf{p}$  generates two terms when applied to a product, the matrix element becomes:

$$\begin{aligned} \langle j | \boldsymbol{\epsilon} \cdot \mathbf{p} | i \rangle &= \int \psi_j^*(\mathbf{r}) u_{c,k_0}^*(\mathbf{r}) (\boldsymbol{\epsilon} \cdot \mathbf{p}) \psi_i(\mathbf{r}) u_{c,k_0}(\mathbf{r}) d\mathbf{r} = \\ &= \int \psi_j^*(\mathbf{r}) [u_{c,k_0}^*(\mathbf{r}) (\boldsymbol{\epsilon} \cdot \mathbf{p}) u_{c,k_0}(\mathbf{r})] \psi_i(\mathbf{r}) d\mathbf{r} + \\ &+ \int u_{c,k_0}^*(\mathbf{r}) [\psi_j^*(\mathbf{r}) (\boldsymbol{\epsilon} \cdot \mathbf{p}) \psi_i(\mathbf{r})] u_{c,k_0}(\mathbf{r}) d\mathbf{r} \end{aligned} \quad (2.18)$$

The envelope functions  $\psi_{i,j}(\mathbf{r})$  are slowly varying in the space region of a unit lattice cell and can thus be considered constant therein. This property allows to exploit the crystal periodicity and thus to extend the two integrals only to a single unit cell, summing later on all the cells. Bringing the envelope functions out of the integral and referring to them via the  $n$ -th unit cell position  $\mathbf{R}_n$ , the matrix element can be safely approximated with the following expression:

$$\begin{aligned} \langle j | \boldsymbol{\epsilon} \cdot \mathbf{p} | i \rangle &\simeq \sum_n \psi_j^*(\mathbf{R}_n) \psi_i(\mathbf{R}_n) \int_{cell} [u_{c,k_0}^*(\mathbf{r}) (\boldsymbol{\epsilon} \cdot \mathbf{p}) u_{c,k_0}(\mathbf{r})] d\mathbf{r} + \\ &+ \sum_n \psi_j^*(\mathbf{R}_n) (\boldsymbol{\epsilon} \cdot \mathbf{p}) \psi_i(\mathbf{R}_n) \int_{cell} [u_{c,k_0}^*(\mathbf{r}) u_{c,k_0}(\mathbf{r})] d\mathbf{r} \simeq \\ &\simeq \langle \psi_j | \psi_i \rangle \langle u_{c,k_0} | (\boldsymbol{\epsilon} \cdot \mathbf{p}) | u_{c,k_0} \rangle + \langle \psi_j | (\boldsymbol{\epsilon} \cdot \mathbf{p}) | \psi_i \rangle \langle u_{c,k_0} | u_{c,k_0} \rangle \end{aligned} \quad (2.19)$$

where the two sums over the unit cells have been substituted with the corresponding integrals. The two terms of equation 2.19 are not non-zero simultaneously and which of them is null depends on the nature of the transition. In the case of ISB transitions, the first term is the one that vanishes, because the envelope functions refer to the different subbands in the same well and they are orthogonal to each other. On the contrary, the periodic functions  $u_{c,k_0}(\mathbf{r})$  refer to the nature of the band in which the QW is located, i.e. the conduction band in the present case. This means that every subband in the conduction band have the same  $u_{c,k_0}(\mathbf{r})$  term in the wavefunction expression, although a different  $\psi_i(\mathbf{r})$ , and the integral  $\langle u_{c,k_0} | u_{c,k_0} \rangle = 1$  always.

Recalling that the initial and final states are of the form

$$\begin{cases} |i\rangle = \psi_i(\mathbf{r}) u_{c,k_0}(\mathbf{r}) = \psi_i(z) e^{i\mathbf{k}_\perp \cdot \mathbf{r}_\perp} u_{c,k_0}(\mathbf{r}) \\ |j\rangle = \psi_j(\mathbf{r}) u_{c,k_0}(\mathbf{r}) = \psi_j(z) e^{i\mathbf{k}'_\perp \cdot \mathbf{r}_\perp} u_{c,k_0}(\mathbf{r}) \end{cases}, \quad (2.20)$$

the matrix element for ISB transitions can be expressed as follows:

$$\langle j | \boldsymbol{\epsilon} \cdot \mathbf{p} | i \rangle = \int d\mathbf{r}_\perp e^{i(\mathbf{k}_\perp - \mathbf{k}'_\perp) \cdot \mathbf{r}_\perp} \int dz \psi_j^*(z) (\boldsymbol{\epsilon} \cdot \mathbf{p}) \psi_i(z) \quad (2.21)$$

The obtained interaction matrix element leads to 3 selection rules:

1. The first integral implies that the matrix element is not-null only if  $\mathbf{k}_\perp = \mathbf{k}'_\perp$ . The allowed transitions are therefore only *vertical* in the reciprocal space, i.e. they only involve states with the same values of  $\mathbf{k}_\perp$ . In the parabolic approximation, this means that all the ISB transitions occurring between the same subbands but at different values of  $\mathbf{k}_\perp$  are characterized by the same transition energy, as depicted in fig. 2.8.
2. The odd nature of the momentum operator  $\mathbf{p}$  sets the allowed ISB transitions only between states with opposite symmetry, e.g.  $|0\rangle \rightarrow |1\rangle$ ,  $|0\rangle \rightarrow |3\rangle$ ,  $|1\rangle \rightarrow |2\rangle$  (see fig. 2.7). This is true only if the wavefunctions have a definite symmetry and the selection rule can be broken if any asymmetry is inserted in the system.
3. Since  $(\boldsymbol{\epsilon} \cdot \mathbf{p})$  is applied to a function depending only on  $z$ , the incident radiation has to exhibit a non-null polarization component along  $z$ .

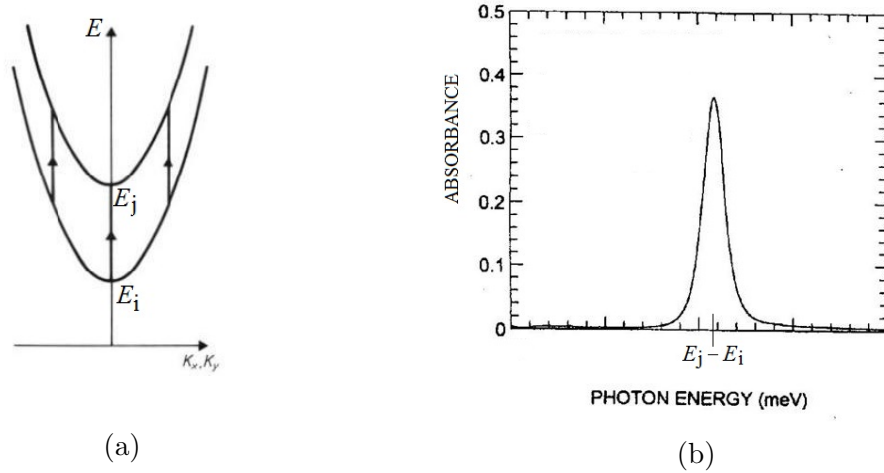


Figure 2.8: Vertical transitions between parabolic subbands. The same transition energy of each different values of the in-plane wavevector (a) corresponds to a single peak in the absorption spectra (b) [3, 62].

The third selection rule concerns the polarization of the incident radiation, allowing only the radiation component polarized along the growth direction  $z$  to generate ISB transitions in a QW. The condition in which the radiation is polarized along  $z$  is called *Transverse Magnetic* (TM) polarization, while a radiation polarized in the  $(x-y)$  plane is said to be *Transverse Electric* (TE) polarized. This notation is generally extended also to the absorption and transmission spectra acquired in the two polarizations, calling them TM and TE spectra. Therefore, the third selection rule forces the ISB transitions to be visible in the TM spectra only, although this result is strictly true only if the effective mass tensor is assumed diagonal.

## 2.3 Bi-dimensional absorption coefficient $\alpha_{2D}$

An important parameter of any structure realized with the aim of obtaining a photonic device is the absorption coefficient, which bears the information on the optical properties and energy structure of the system. The absorption coefficient of a bulk material is usually defined as the ratio between the electromagnetic energy absorbed per unit time and volume, obtained from the absorption rate  $W$  [3], and the intensity of the incident radiation. In the case of bi-dimensional systems like a QW, it is necessary to introduce some modifications to this definition. The most common and natural way to do so is to consider the absorption per unit area and not per unit volume, defining the *bi-dimensional absorption coefficient*  $\alpha_{2D}$  as a function of the incident radiation energy  $E$ . This bi-dimensional coefficient is dimensionless, differently to what happens in the 3D case, and it represents the measure of the radiation absorbed by a single 2D layer of the system.

To make notation simpler, in the following it will be used the definition

$$\langle \psi_j | p_z | \psi_i \rangle = \int dz \psi_j^*(z) (\epsilon_z \cdot p_z) \psi_i(z) \quad (2.22)$$

where only the  $z$ -component of the scalar product  $(\boldsymbol{\epsilon} \cdot \mathbf{p})$  has been considered, since it is the only one coupling with the ISB transitions.

Considering an incident radiation with frequency  $\omega$  and an absorbing system of refractive index  $\eta$  ( $\eta_{Ge} = 4$ ), the bi-dimensional absorption coefficient is [3]:

$$\begin{aligned} \alpha_{2D}(\omega) &= \\ &= \frac{\pi e^2}{\varepsilon_0 c \eta \omega m^{*2}} \sum_{i,j} \frac{2}{(2\pi)^2} \int d\mathbf{k}_\perp |\langle \psi_j | p_z | \psi_i \rangle|^2 [\rho(E_i) - \rho(E_j)] \delta(E_j - E_i - \hbar\omega) \end{aligned} \quad (2.23)$$

where  $m^*$  is the effective mass,  $\varepsilon_0$  is the vacuum permittivity and  $c$  the speed of light. The above expression can be highly simplified if a parabolic subband dispersion in the  $(x-y)$  plane is assumed, allowing for a direct integration over the Fermi-Dirac distribution, which is possible to perform analytically only in 2D. It is also useful to introduce the dimensionless *oscillator strength*

$$f_{ij} = \frac{2}{m^*(E_j - E_i)} |\langle \psi_j | p_z | \psi_i \rangle|^2 \quad (2.24)$$

which obeys the sum rule

$$\sum_j f_{ij} = 1 \quad (2.25)$$

valid for each initial state  $i$ . In the sum, the absorption transitions are counted as positive and the emissions as negative. Since in all the investigated samples the doping process allowed only the first subband to be populated, the initial state of the sum rule is only the one with  $i = 0$  and it can be demonstrated that in this case the dominant contribution to the sum is the  $f_{01}$  one, related to the first ISB transition from the ground level to the first excited one. The value of  $f_{01}$  is almost

1, and anyway more than 30 times the second highest contribution, therefore it is safe to consider it equal to 1.

Assuming a low enough temperature, the bi-dimensional absorption coefficient exhibits the simple following form:

$$\alpha_{2D}(E = \hbar\omega) = \frac{n_{2D}\hbar e^2}{2\varepsilon_0 c \eta m^*} \frac{\Gamma}{(E_2 - E_1 - \hbar\omega)^2 + \Gamma^2} \quad (2.26)$$

where  $n_{2D}$  is the bi-dimensional charge density in the QW. A more realistic lorentzian shape with linewidth  $2\Gamma$  is considered instead of the theoretical delta function, to take into account a finite lifetime of the excited states as reported in fig. 2.9 for the result obtained from an absorption experiment. Here the energy position of the absorption peak depends on the energy separation of the involved states and thus on the QW width  $d_w$ , as already discussed in equation 2.12. In the figure it is also possible to see the line-shape asymmetric broadening of the absorption peak when the well width is so small that only one subband can be arranged inside (width of 35-47 Å). In these cases, the absorption spectra refer to transitions with a confined subband as initial state and a continuous of levels outside the well as final states.

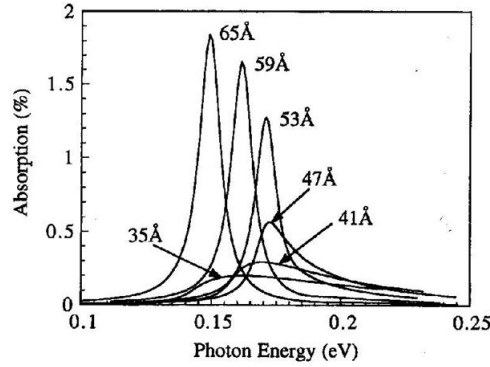


Figure 2.9: Absorption spectra for QWs of different width. Symmetric peaks refer to QWs with at least two subbands inside (from 53 Å to 65 Å), while asymmetric peaks refer to QWs with only one subband inside (from 35 Å to 47 Å) [63].

### 2.3.1 Transmittance and absorption coefficient

One of the methods to investigate the optical properties of a QW system is to study the ISB transitions analyzing the sample transmittance as a function of the energy. In fact, the transmittance through a QW sample is directly linked to its bi-dimensional absorption coefficient  $\alpha_{2D}(E)$  and therefore includes all the optical properties discussed in the previous sections.

In the case of a bulk material, the transmittance  $T(E)$  is defined as the ratio between the transmitted radiation intensity  $I_t$  and the incident radiation intensity  $I_0$ , and it is related to the three-dimensional absorption coefficient  $\alpha_{3D}$  via the common Lambert-Beer law:

$$T(E) = \frac{I_t}{I_0} = e^{-\alpha_{3D} \cdot h} \quad (2.27)$$

where  $h$  is the material thickness the radiation gets through.

In the case of a bi-dimensional system, the law has to be modified to take into account several geometric parameters, since it is experimentally almost impossible to measure a sample transmittance in straight collinear geometry. In fact, the third selection rule for ISB transitions forbids the simple acquisition of transmitted intensity through a thin sample in normal incidence, as generally happens in the 3D case, and a waveguide geometry needs to be employed. An example of a waveguide suitable for transmittance experiments is depicted in fig. 2.10, in which the radiation undergoes internal reflections through the QW active region, guaranteed by the difference in the refractive index of the material compared to that of the vacuum. The electric field component along the growth direction  $z$  is thus modulated by the sinus of the angle  $\theta$ , which leads to a factor  $\sin^2 \theta$  in the radiation intensity. Concerning the optical path length, the radiation inside the sample proceeds through a thickness much higher than the QW stack extension in the  $z$ -direction and another factor  $1/\cos \theta$  has therefore to be considered and multiplied for the number  $M$  of times the radiation goes through the QW region ( $M = 2$  in fig. 2.10, twice for each reflection on the QW side of the sample). Since the boundary conditions of the Maxwell equations inside the waveguide impose a null intensity of the  $z$ -component of the electric field at the sample-vacuum interface, a metal deposition is needed in order to amplify such component, as it will be discussed later. The resulting form of the transmittance through a QW sample in a waveguide configuration similar to the one depicted in fig. 2.10 is therefore:

$$T(E) = t \exp \left( -CMN_W \alpha_{2D}(E) \frac{\sin^2 \theta}{\cos \theta} \right) \quad (2.28)$$

where  $t$  is the transmission coefficient of the waveguide facet, calculated from the common Fresnel formula [64]. Although this coefficient is in principle different in TM and TE polarization, it is here considered the same in the two cases since the small difference does not introduce any significant correction but only a small underestimation of the peak value of  $\alpha_{2D}$ . The quantity  $N_W$  in the above equation is the number of QWs inside the sample and  $C$  the amplifying factor of the  $z$ -component of the electric field due to the surface metal deposition. This parameter is estimated to be  $C = 1.5$  for samples featuring characteristics comparable to those employed in this work [31,65]. The bi-dimensional absorption coefficient can therefore be directly obtained from an experimental measure of the sample transmittance  $T(E)$ :

$$\alpha_{2D}(E) = -\frac{\ln [T(E)] \cos \theta}{CMN_W \sin^2 \theta} \quad (2.29)$$

The relation of the bi-dimensional absorption coefficient obtained from the sample transmittance  $T(E)$  can be compared to equation 2.26 in order to retrieve the needed information, e.g. the ISB transition energies. Another important feature related to the sample transmittance is the bi-dimensional charge density  $n_{2D}$ , since it is responsible for absorbing the radiation propagating through the waveguide. It can be directly evaluated by integrating the bi-dimensional absorption coefficient experimental curve obtained from the sample transmittance:

$$\int \alpha_{2D}(E) dE = n_{2D} \frac{\pi \hbar e^2}{2\varepsilon_0 \eta c m^*} \quad (2.30)$$

as results from the integration of the lorentzian function of equation 2.26.



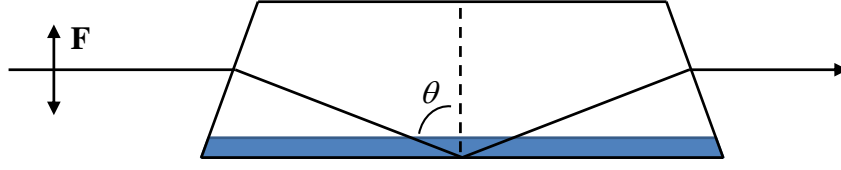


Figure 2.10: Waveguide geometry with internal reflection angle  $\theta$  and electric field  $\mathbf{F}$  oriented along the growth direction  $z$ . The highlighted area is the active region in which the QWs are located.

## 2.4 Inverse effective mass tensor

The effective mass  $m^*$  has been previously used in equation 2.2 as a constant to be considered instead of the electron mass  $m_e$  in order to write a Schrödinger equation for the envelope function only. However, this quantity can be considered as a constant only in isotropic materials, which do not include Ge for example. In a general three-dimensional system an *inverse effective mass tensor* is defined, whose components are:

$$M_{ij}^*(\mathbf{k}) = \frac{1}{\hbar^2} \frac{d^2}{dk_i dk_j} E(\mathbf{k}) \quad (2.31)$$

This means that the Hamiltonian of the Schrödinger equation for the envelope function  $\psi(\mathbf{r})$  has to be modified to include the inverse effective mass tensor and becomes

$$H = \frac{1}{2} \mathbf{p} \cdot \mathbf{M}^* \cdot \mathbf{p} + V_0(z) \quad (2.32)$$

Exploiting the wavefunction factorization of equation 2.3, the Schrödinger equation is expressed only in terms of the  $z$ -component, similarly to equation 2.4 [66]:

$$\left[ -\frac{\hbar^2}{2/M_{zz}^*} + V_0(z) \right] \psi(z) = (E - E_{\perp}) = E_n \psi(z) \quad (2.33)$$

where  $E_{\perp}$  is the in-plane dispersion which depends on the inverse effective mass tensor components<sup>(1)</sup>:

$$\begin{aligned} E_{\perp} = \frac{\hbar^2}{2} & \left[ \left( M_{zz}^* - \frac{(M_{xz}^*)^2}{M_{zz}^*} \right) k_x^2 + \left( M_{xy}^* - \frac{M_{xz}^* M_{yz}^*}{M_{zz}^*} \right) k_x k_y + \right. \\ & \left. + \left( M_{yy}^* - \frac{(M_{yz}^*)^2}{M_{zz}^*} \right) k_y^2 \right] = \\ & = \frac{\hbar^2}{2} \left[ \frac{1}{m_x^*} k_x^2 + \frac{1}{m_{xy}^*} k_x k_y + \frac{1}{m_y^*} k_y^2 \right] \end{aligned} \quad (2.34)$$

where the proper values of the effective mass are considered depending on the considered direction.

The specific expression of the inverse effective mass tensor depends on the nature of the minima in the band structure of the material taken into consideration. For

<sup>1</sup>Here the function  $\psi(z)$  is not exactly the function used in reference [66], but for the purpose of the present discussion the difference is not of much importance.

example, the 6  $\Delta$ -valleys of Si(100) are oriented along the principal directions and hence they are described by a diagonal tensor in which the non-zero elements are the effective masses along the three directions of the ellipsoids depicted in fig. 1.3. The case of Ge(100) is different because the L-valleys ellipsoids are tilted with respect to the principal directions and  $M^*$  is therefore not diagonal [12]:

$$M^* = \begin{pmatrix} M_{xx}^* & M_{xy}^* & M_{xz}^* \\ M_{yx}^* & M_{yy}^* & M_{yz}^* \\ M_{zx}^* & M_{zy}^* & M_{zz}^* \end{pmatrix} = \begin{pmatrix} \frac{1}{3} \left( \frac{1}{m_t} + \frac{2}{m_l} \right) & 0 & \frac{\sqrt{2}}{3} \left( \frac{1}{m_t} - \frac{1}{m_l} \right) \\ 0 & \frac{1}{m_t} & 0 \\ \frac{\sqrt{2}}{3} \left( \frac{1}{m_t} - \frac{1}{m_l} \right) & 0 & \frac{1}{3} \left( \frac{2}{m_t} + \frac{1}{m_l} \right) \end{pmatrix} \quad (2.35)$$

where  $m_l = 1.64m_e$  is the Ge longitudinal effective mass along the  $\Lambda$  direction (see fig. 1.1) and  $m_t = 0.082m_e$  the corresponding transverse value. The specific form of the inverse effective mass tensor for Ge implies that the second term of the in-plane dispersion of equation 2.34 vanishes, since  $1/m_{xy}^* = 0$ . The remaining terms are generally averaged on the  $(x-y)$  plane considering the *density-of-states effective mass*  $m_d = \sqrt{m_x^* m_y^*} = \sqrt{m_t(m_t + 2m_l)/3} = 0.3m_e$ , resulting in the more common expression for the energy dispersion:

$$E = E_n + \frac{\hbar^2}{2m_d} (k_x^2 + k_y^2) \quad (2.36)$$

Following the discussion in reference [12], when the non-isotropic conduction band minima are involved, also the transition rate  $W$  has to be modified in order to account for the different effective masses along the principal directions. This implies that all the physical quantities related to the transition rate have to include the proper effective mass, which is the case of the bi-dimensional absorption coefficient  $\alpha_{2D}(E)$  and, of course, of the oscillator strength  $f_{ij}$  defined in equation 2.24. The proper value to be included in these expressions depends on the direction of the electric field driving the electrons. In particular, the correct form of  $f_{ij}$  for a non-isotropic material like Ge is:

$$f_{ij} = \frac{2}{(E_j - E_i)} |\langle \psi_j | p_z | \psi_i \rangle|^2 |\boldsymbol{\epsilon} \cdot M^* \cdot \hat{\mathbf{z}}|^2 \quad (2.37)$$

where  $\hat{\mathbf{z}}$  is the unitary vector in the  $z$  direction. In the case of transitions induced by a TM polarized radiation, in which the polarization vector is along  $z$  ( $\boldsymbol{\epsilon} \equiv \hat{\mathbf{z}}$ ), the oscillator strength is found to be inversely proportional to  $m^* = 1/M_{zz}^* = 0.12m_e$ , which is the correct value to consider in the bi-dimensional absorption coefficient  $\alpha_{2D}(E)$  of equation 2.26. This low value of the effective mass compared to the case of Si is one of the main reasons Ge is a promising material for the opto-electronic devices realization. In fact, the difference in the two values leads to an amplifying factor in the absorption coefficient and transition rate of  $(m_{Si}^*/m_{Ge}^*)^2 = (0.92/0.12)^2 \simeq 70$ .

Moreover, the non-diagonal nature of the Ge inverse effective mass tensor suggests the possibility to induce ISB transitions also in the TE configuration, since the component  $M_{xz}^*$  is not null. This is one of the main features that made Ge

QWs more attractive than other materials to obtain normal emission (or absorption) in opto-electronic devices, thanks to the coupling of the  $x$ - and  $z$ -component of the radiation through the inverse effective mass tensor. Although this result is in principle true and ISB transitions are expected to be visible in TE spectra with intensities around 20% compared to the TM polarization case, transitions between bound states in TE configuration have never been observed so far. For these reasons, in the present work the ISB transitions will be assumed to be present only in the spectra acquired through TM-polarized radiation.

## 2.5 Non-ideal effects and corresponding corrections

The study of the QW characteristics carried so far lied on the assumption of single non-interacting electrons in subbands with perfect parabolic energy dispersion, neglecting any multi-particle interaction and non-ideal effects generated by the real electron band structure. Most of the corrections that should be applied to account for these effects compensate with each other, leaving the *depolarization shift* the only relevant contribution and therefore the only one considered in the QW system analysis. In the following, a brief description of the principal non-ideal effects is presented, without any purpose to be exhaustive.

**Depolarization shift.** The depolarization shift is the most relevant effect on the transition energy, making the absorption peak to appear in the spectra at higher energies if compared to what expected from a single-particle framework prediction. This many-body effect reflects the situation of a real charge surrounded by an electron distribution polarized by the external field, which shields the charge and impose a higher energy to induce the ISB transition [3].

The contribution of the depolarization shift can be represented by a parameter  $\phi > 0$  to be included as a correction in the transition energy:

$$\tilde{E}_{ij}^2 = E_{ij}^2(1 + \phi) \quad (2.38)$$

where  $\tilde{E}_{ij}$  is the new transition energy and  $E_{ij}$  the expected transition energy obtained in a single-particle framework without the depolarization shift. If the temperature is low enough to consider only the ground level  $|0\rangle$  populated, the depolarization shift parameter is of the following form [3, 69]:

$$\phi = \frac{2e^2\bar{d}}{\varepsilon_r\varepsilon_0E_{01}}n_{2D} \quad (2.39)$$

where  $\varepsilon_r = \eta^2$  is the dielectric constant of the material and  $\bar{d}$  is a parameter defined starting from the wavefunction overlap integral, which can be easily expressed as  $\bar{d} = \frac{5}{9\pi^2}d_w$  if the QW is infinitely deep.

The depolarization shift  $\tilde{E}_{01} - E_{01}$  is therefore a relevant correction only in the case of high charge density  $n_{2D}$  and small energy separation between levels, i.e. in the case of wide wells. Concerning the samples investigated in this work, despite

the electron densities achieved with the doping process should allow to neglect the depolarization shift correction if the wells are wide less than 15 nm, it will be anyway considered in the analysis of every sample.

If working at finite temperatures high enough to partially populate also the first excited level  $|1\rangle$ , the relevant feature that sets the depolarization shift intensity is not the total charge density  $n_{2D}$ , but the relative population  $\Delta n = n_0 - n_1$ . This implies that the depolarization shift intensity can vary with the temperature, since temperature variations lead to variations in the level populations [67, 68].

**Exciton shift.** The other collective effect that will be here discussed is the *exciton shift*, which together with the depolarization shift influences the ISB transition energy. As the name suggests, this effect is similar to the exciton interaction present when an electron-hole pair is created in inter-band transitions, also in bulk materials. Here the interaction is between the excited electron and the quasi-hole created in the initial subband, even if it is not a proper exciton in the sense of an electron-hole bound state but more a mean correction to the energy transition. This negative contribution is expressed by a positive parameter  $\beta$  generally appearing alongside the one related to the depolarization shift:

$$\tilde{E}_{ij}^2 = E_{ij}^2(1 + \phi - \beta) \quad (2.40)$$

The expression of  $\beta$  includes not only the wavefunctions involved in the ISB transition and the charge density, but also the potential related to the many-body Coulomb interactions. A detailed description can be found in references [3, 70–72].

**Non-parabolicity.** At the beginning of this chapter it has been shown how it is possible to consider a simple Schrödinger equation for the envelope functions only, at the condition of substituting the electron mass  $m_e$  with the effective mass  $m^*$ , as a constant depending only on the material ( $m_{Ge}^* = 0.12m_e$ ). One of the consequence of this approximation is that the subbands appear of perfect quadratic form and parallel to each other. Discussing the first selection rule of the ISB transitions, it has been stated that in presence of parallel subbands every vertical transition would be characterized by the same energy, whatever the value of  $\mathbf{k}_\perp$  is. However, in the real non-isotropic case this statement cannot be true, since the effective mass exhibits the energy dependence shown in equation 2.31 and thus the subbands are not parallel to each other. In this case, the vertical ISB transitions would feature different energies depending on the wavevector  $\mathbf{k}_\perp$  of the initial state. The example in fig. 2.11 shows that the higher the  $\mathbf{k}_\perp$  is, the lower is the transition energy from the ground subband to the first excited one [3]. Therefore, when a broadband (non-monochromatic) radiation propagates through the sample, more than one frequency is absorbed. This phenomenon implies a broadening of the transition peak in the spectrum, which is the sum of many different single-frequency absorption peaks related to each different transition at different values of  $\mathbf{k}_\perp$ .

**Coulomb interactions.** The electron charge inside a QW generates Coulomb interactions that have been ignored in the single-particle discussion of the ISB transitions. Although often of negligible intensity, they in principle influence the absorption processes. The Coulomb interactions that involve the well electron population

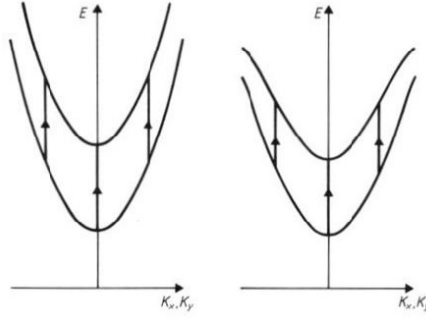


Figure 2.11: Effect of the subbands non-parabolicity on the transition energy. Different energies are obtained from transitions at different values of the in-plane momentum  $\mathbf{k}_\perp$  (right scheme) compared to the case of parallel subbands (left scheme).

belong to two different categories: one is related to the charge present inside the well and one is instead related to the charge outside the well.

Concerning the first group, the Coulomb interaction of a charge distribution with itself generates two contributions to the energy known as *exchange energy* and *correlation energy*, which can be obtained from the Hartree-Fock equations or from the density functional theory [73, 74]. The second group of interactions originates from the doping procedure needed to populate the first subband, which employs donor atoms inserted in the material lattice during the growth process. When the electrons are transferred from the donor atoms to the first subband of the QW, the interaction with the left behind ions generates an electrostatic field that influences the absorption process [3]. The field intensity depends on the doping technique employed and can be so low to be negligible or high enough to introduce a significant contribution. With the direct doping technique the donor atoms are inserted in the Ge layers and the corresponding donor levels are right under the conduction band edge (i.e. right under the well), localized in the same space region of the electrons populating the QW. In this way, the electrostatic field is generally so low to be neglected. On the contrary, when the modulation doping technique is employed the donors are inserted in the SiGe layers, leaving the barriers with a positive charge density spatially separated from the electron density populating the QW. In this case, the conduction band undergoes a changing in its profile due to the strong field established. This *band bending* reflects in a decreasing of the energy distance between the subbands that should be generally taken into account. In fig. 2.12 a sketch of the effect of the modulation doping on the band profile is showed.

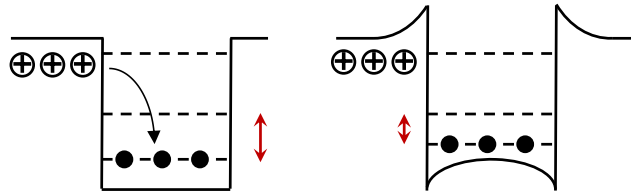


Figure 2.12: Band bending and corresponding levels shift in the presence of modulation doping. The first transition is reduced in energy as effect of the Coulomb interaction between the electrons and the ionized donors in the barrier.



## 3

# Sample growth and structural characterization

The growth of the samples investigated in the present work of thesis took place at the “Laboratory of Semiconductor Physics and Technology” (LFTS) at “Università Roma TRE”, where a clean room is equipped with the suitable deposition setup for ultra-high vacuum (UHV) CVD epitaxial growth. Referring to the components sketched in fig. 3.1, the setup consists in one pipe (1) kept at a UHV pressure ( $\sim 10^{-10}$  Torr) guaranteed by two ionic pumps, a pressure regime required in order to obtain high quality samples with low contamination thanks to the low number of colliding molecules. Several chambers are connected to the tube with the help of suitable valves, allowing the low pressure conditions to be preserved within all the setup components. The only component at higher pressure is the load-lock chamber (2), which serves as linking point with the external environment to load the substrate into the system. Here, a pressure around  $10^{-7}$  Torr is reached by a pumping system of a turbo-molecular pump coupled to a rotary one.

The substrate is initially prepared in a clean environment under laminar flow equipped with a chemical hood (3) and loaded into the load-lock chamber (2) before entering the preparation chamber (4), with the use of magnetic manipulators. From there it can travel the tube (1) to reach the UHV-CVD chamber (5) for deposition or the X-ray photoemission spectroscopy (XPS) chamber (6) for analysis.

Employing the described setup, ten samples have been grown (S1-S10) and their structural properties have been then investigated with several techniques.

## 3.1 CVD growth setup

The CVD chamber for the epitaxial growth is a steel cylinder with low content in carbon and nickel connected to the main tube with a valve that is kept closed during the deposition process not to contaminate the rest of the system. The chamber is equipped with external water cooling to limit the contaminant desorption from the internal surface and thus to help keeping a low pressure inside. Low pressure is required in order to obtain deposition conditions in which the sample surface is preserved from contamination and all the growth steps can be kept under full control. High quality samples are obtained only in UHV conditions, with a pressures in the

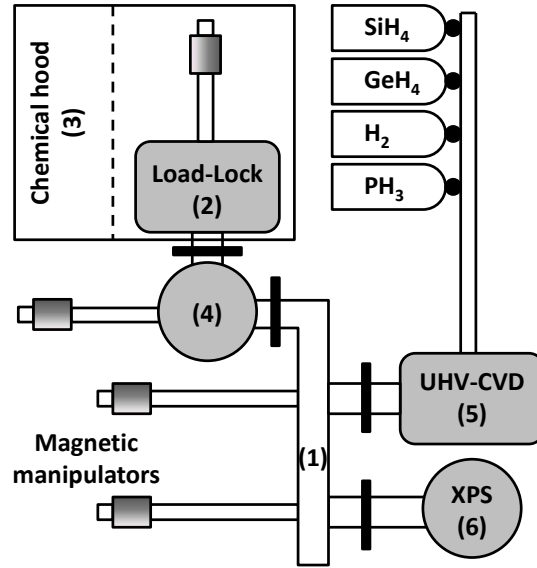


Figure 3.1: Growth setup scheme: (1) main pipe, (2) load-lock chamber for loading substrates into the UHV system, (3) chemical hood for substrate preparation, (4) preparation chamber for thermal treatments of the substrate, (5) UHV-CVD growth chamber, (6) XPS chamber for in-situ analyses. Magnetic manipulators are used to transport the samples across the different setup parts, separated by the UHV valves indicated in black.

range of  $10^{-10}$  Torr that can be reached with a proper pumping system of turbo-molecular and rotary pumps. At these pressure values, the molecules impinging the sample surface are few enough to guarantee a clean surface during deposition. For example, at a pressure of  $10^{-6}$  Torr the number of molecules hitting and sticking to the sample surface is so high to completely cover it in about 1 second. On the contrary, UHV conditions assure a clean surface for several hours giving sufficient time for a clean deposition.

Cooling the chamber and equipping it with the proper pumping system is not enough to reach the desired low pressure, since the desorption of molecules from the internal surface is still too high to reach UHV in a reasonable amount of time if the pumping process starts from atmospheric conditions. To accelerate the process and allow the pressure to be lowered down to the UHV regime, it is necessary to perform a *baking* operation. The baking consists in heating the whole CVD chamber with resistive cables that bring the temperature up to  $150^{\circ}\text{C}$ , forcing the inner adsorbed molecules to desorb at high speed. This procedure assures that the residual desorption rate inside the chamber after the baking is low enough to reach UHV pressures suitable for clean sample realization, with the use of the proper pumping system.

Once reached the lowest pressure possible with the employed setup, deposition can take place introducing the gaseous precursors in the CVD chamber, which are stored in tanks located in the lab roof for safety. The precursors are individually introduced through electro-pneumatic valves and the flux is set by flowmeters placed in each gas line entering the CVD chamber. Both valves and flowmeters are electronically controlled by a dedicated computer with a Labview graphical interface,



which also serves for automatic depositions of the heterostructures in those steps with constant temperature and pressure. These two growth parameters, in fact, are generally not constant since many delicate steps require substrate temperature and gas pressure to be tuned during the process, as it happens in the case of the virtual substrates realization. The required temperatures are reached heating the samples via Joule effect with a power supply that delivers the set current to the sample through a metal finger, connected to an electrical feedthrough. A set of windows allows to monitor the substrate temperature with a pyrometer, while the pressure can be monitored by different instruments working at different ranges. Before and after the deposition process, the UHV pressure inside the chamber is measured by an ion gauge, but it has to be switched off when the gaseous precursors are present. In fact, silane and germane can damage the ion gauge because of its hot metal filament it uses to measure the pressure, on which the pyrolysis can occur. Therefore, the filament can be rapidly covered in deposited Si and Ge, resulting in malfunctioning or breaking. During the deposition process the pressure is thus monitored with a capacitive sensor, which does not employ a hot filament but it can measure pressures only in the range of  $10^{-3}$  Torr.

### 3.1.1 In-situ physical characterization technique

After the deposition of an heterostructure it could be important to check the result before characterizing its optical properties. For example, it is often needed to retrieve the composition of a deposited SiGe layer and to eventually calibrate the growth parameters used in the deposition process to match the desired relative concentrations. Two other important aspects strongly influencing the deposition results are the cleaning conditions of the substrate, which should not present contaminants on its surface before the deposition starts, and the residual contamination inside the CVD chamber that will result in the presence of undesired components in the grown structure. All these aspects can be monitored using the X-ray photoemission spectroscopy (XPS), a non-destructive investigation technique which allows to retrieve the composition of a surface highlighting the fingerprints of every element present.

## X-ray Photoemission Spectroscopy

The experimental setup in fig. 3.1 is equipped with an UHV chamber (6) for X-ray photoemission spectroscopy (XPS), used to verify SiGe alloy concentrations and identify eventual contaminants inside the samples and on the substrates surface. The XPS chamber mainly features an X-ray source and an electron analyzer. The source provides a photon beam of 1486.6 eV of energy generated by the radiative electron-hole recombination in the aluminum anode, hit by electrons thermo-emitted from a tungsten cathode. The radiation is sent through a monochromator to reduce its linewidth down to a value around 0.3 eV, and it is then directed towards the sample. The interaction of the X-ray beam with the sample surface generates photoemitted electrons collected by the analyzer, which consists in a hemispheric cavity whose walls are polarized in order to collect electrons with a specific energy. Varying the applied potential it is possible to select only the electrons with the right trajectory, able to get through the cavity without hitting the walls and thus enter the

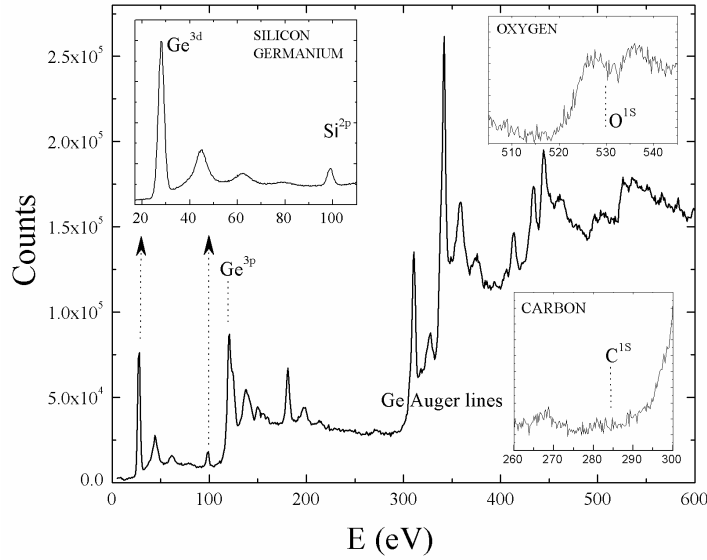


Figure 3.2: Example of an XPS spectrum acquired to check the composition and contamination on the sample surface. Insets show the zoom of three important energy ranges in which germanium 3d ( $\text{Ge}^{3d}$ ), silicon 2p ( $\text{Si}^{2p}$ ), oxygen 1s ( $\text{O}^{1s}$ ) and carbon 1s ( $\text{C}^{1s}$ ) photoemission peaks are present.

*channeltron*. Here, the electrons are multiplied in number thanks to the peculiarity of the material the channeltron is made of, emitting several electrons for every incident one in a cascade process which results in an amplification of a factor of  $10^6$ . Therefore, for every electron entering the channeltron an electric signal is generated, associated to the specific electron energy set to exit the hemispheric cavity. Scanning the cavity voltage results in the acquisition of a photoemission spectrum with a resolution depending on the specific configuration used, down to 0.35 eV.

The operating principle of the XPS technique is based on the photoelectric effect, according to which a material emits electrons if hit by radiation with sufficient energy, following the relation

$$K = \hbar\omega - E_b - \phi_a \quad (3.1)$$

where  $K$  is the kinetic energy of the photoemitted electron,  $E_b$  the binding energy related to the initial state before photoemission and  $\phi_a$  the work function of the analyzer. Knowing  $\phi_a$  and measuring the kinetic energy  $K$  of the photoelectrons as described above it is therefore possible to retrieve their binding energies  $E_b$ , peculiar of each specific element. With this technique it is possible to obtain the alloy concentration and contamination of a sample surface, since the number of counts recorded by the analyzer is proportional to the corresponding element abundance, weighted by the cross section of the specific electronic level involved.

In the case of the work presented here, the XPS technique has been employed to retrieve the composition of the deposited  $\text{Si}_{1-x}\text{Ge}_x$  alloys to eventually calibrate the growth parameters and to check the contamination level of both samples and substrates, limited to the first surface layers due to the low photoelectrons escape depth inside the material (few Ångström). In fig. 3.2 a typical XPS spectrum of SiGe sample is displayed, in which the photoemission peaks needed to retrieve the

alloy concentration are highlighted. The insets on the right show the zoom of the portions of the spectrum related to the most common contaminants. The extremely suppressed intensity of the photoemission peaks related to carbon and oxygen atoms testifies their low concentration, assuring the high cleaning level and the quality of the sample under investigation.

## 3.2 Ex-situ structural characterization techniques

Once the deposition process is concluded, a structural characterization of the realized samples can be performed ex-situ employing several different techniques. The peculiarities of each characterization process allow to retrieve important information on the grown structures, as the defect density or the surface roughness. The main features of the employed techniques will be briefly discussed in the following, together with the corresponding information that can be obtained.

### Atomic Force Microscopy

The atomic force microscopy (AFM) is a scanning probe technique largely used to characterize the surface of many types of samples in different conditions. Here it has been used to image the surface topography of the grown structures in order to retrieve the surface roughness and the characteristic dimension of the eventual surface defects or terraces. The working principle of the microscope relies on the interaction between the sample surface and a small tip with a curvature radius of few nanometers. The tip is mounted on a cantilever whose movements are monitored by an optical system consisting in several mirrors guiding a laser beam on the cantilever and then on a position sensitive photo-detector after the reflection. Scanning the sample surface in the  $(x-y)$  plane results in the cantilever position change in the  $z$  direction and in the corresponding deflection of the reflected beam. A feedback loop acts on the piezoelectric scanner tube on which the sample is mounted, adjusting its height with respect to the cantilever and restoring the initial position of the reflected laser beam on the photo-detector. The scanner contraction (or expansion) at each  $(x-y)$  coordinate can be therefore recorded to retrieve the sample surface topography. A simple scheme of an AFM measurement is shown in fig. 3.3.

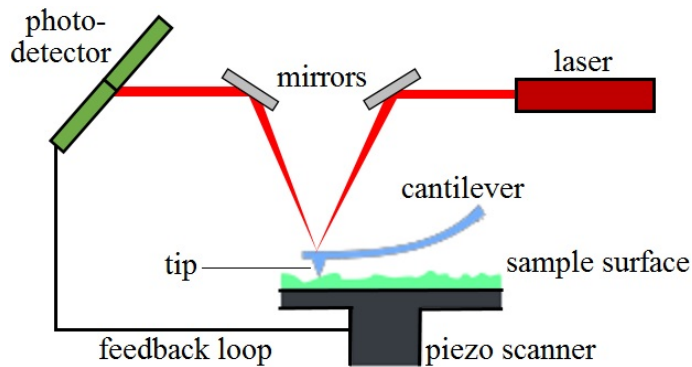


Figure 3.3: Scheme of an AFM measurement.

The AFM measurements on the grown samples have been performed in our LFTS laboratory with a Veeco CPII lying on a vibration-damping table and equipped with acoustic and electromagnetic shields. The typical resolution along  $z$  is less than 1 nm, while it is around 5 nm on the  $(x-y)$  plane. With this technique it has been possible also to estimate the temperature at which the Ge growth on Si substrates enters the Stranski-Krastanov regime, highlighting the formation of islands on the surface, and therefore it allowed to estimate the best temperature for a planar growth, which is found to be around 340°C.

## Transmission Electron Microscopy

While the AFM measurements give information about the sample surface morphology, investigation on the bulk properties of the heterostructure can be performed employing the transmission electron microscopy (TEM) which allows to retrieve structural information like the layer thicknesses. This technique consists in detecting an electron beam transmitted through the sample, highlighting the differences in composition corresponding to the differences in the transmitted intensity. The employment of an electron beam allows to achieve better resolutions compared to the imaging techniques relying on light beams because of the smaller wavelength associated to electrons, and thickness fluctuations less than 1 nm can be detected.

Beside the conventional TEM, scanning measurements (STEM) at high resolution have been performed at the IMM institute of the “National Research Council” (CNR) of Catania, employing a JEOL 2010F TEM/STEM microscope equipped with a Schottky field-emission electron gun operating at 200 keV, and objective lens with spherical aberration correction. In particular, the “high angle annular dark field” technique (HAADF-STEM) sketched in fig. 3.4 has been employed in order to be sensitive to alloy composition fluctuations below 5%, much higher than the standard bright field technique. Exploiting the high resolution achieved with this technique, several structural properties of the grown samples have been analyzed, as the defect density, the layers thickness and the roughness at the interfaces between them.

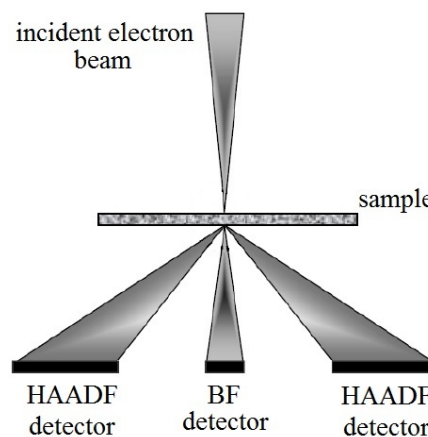


Figure 3.4: Sketch of the TEM geometry acquisition in bright field (BF) and dark field with the annular detector (HAADF).

## X-ray Diffraction

Another technique often employed for heterostructures characterization together with the TEM is the X-ray diffraction (XRD) [75]. The principle of the XRD is to collect the diffracted photons coming from the sample under an incident X-ray beam and analyze the diffraction pattern. In fact, the angles and the intensities of the diffracted beams carry information about the structural properties of the bulk system, as the lattice parameter and the spatial periodicity. The XRD is thus a more than suitable technique to obtain the interesting properties of an heterostructure since, starting from basic knowledge of the sample or from results of other characterizations (like the concentrations obtained from the XPS investigations), it is possible to retrieve the strain present in the structure, the thickness and the composition of the layers the heterostructure is made of.

The XRD measurement have been performed at the IHP-microelectronics institute of Frankfurt-Oder employing a SmartLab diffractometer from Rigaku equipped with a 9 kW rotating-anode Cu source, a Ge(400) $\times$ 2 crystal collimator and a Ge(200) $\times$ 2 crystal analyzer. The apparatus allows to image the reciprocal space map of the investigated samples and to simulate a diffraction pattern for comparison.

## 3.3 Substrate preparation

The realization of a high quality sample starts from a correct Si substrate preparation. On the opposite, a contaminated substrate generates defects propagating through the whole structure, which leads to a poor final result. Even if accurate procedures and perfect growth steps are performed afterwards, an inadequate starting substrate means a failure, leading to a waste of time and resources. For this reason, a proper sample deposition requires a high quality n-doped ( $\simeq 10^{15} \text{ cm}^{-3}$ ) Si(100) wafer from which several substrates are cut in a clean environment with professional semi-automatic scribes. The doping is necessary in order to allow the current propagation needed to heat the substrate up to the growth temperature.

The Si substrate preparation that will be discussed here could be summarized in the following steps:

- Chemical and mechanical cleaning performed in the chemical hood (3) to remove physisorbed contaminants.
- Thermal cleaning at current of 0.30 A in the preparation chamber (4) to remove chemisorbed contaminants.
- Thermal cleaning in  $\text{H}_2$  atmosphere at  $1150^\circ\text{C}$  in the CVD chamber (5) to remove native silicon oxide.
- Deposition of a Si layers at  $800^\circ\text{C}$  in the CVD chamber (5) to reconstruct a planar Si surface.

The cleaning processes the substrate undergoes start inside the chemical hood (indicated with number (3) in fig. 3.1), the first one being an ultrasonic bath in isopropyl alcohol (2-propanol  $\text{CH}_3\text{CH}(\text{OH})\text{CH}_3$ ) for the duration of 20 minutes. This step assures the desorption of organic contaminants present on the substrate surface, and the alcohol traces left behind can be removed with a continuous-flow rinse in de-ionized water. The rinse products are monitored by an instrument that measures

the water resistivity and therefore its purity level. When the rinsing water reaches the proper resistivity value (around  $10 \text{ M}\Omega\cdot\text{cm}$ ) it can be considered free of contaminants, implying that the rinsed substrate surface is clean of physisorbed impurities. In fact, the residues present in the rinsing water, which come from the substrate surface, tends to lower the water resistivity under its nominal value. Once the rinse is finished the substrate needs to be dried under a nitrogen jet of ultra-high purity, in order to remove any water residue without contaminating the clean surface. This step has to be as quick as possible because the substrate is exposed to the air, which contaminates the surface the more it stays unprotected.

After the substrate surface is free of physisorbed impurities, further cleaning is necessary to remove any chemisorbed contaminant. To this purpose the substrate is set on a sample holder, on which it will be kept not only for the remaining cleaning processes but also for the epitaxial deposition. The holder consists in one conductive part in steel and tantalum, and one insulating part in Macor and quartz. The substrate is fixed to the holder using molybdenum contacts and steel screws. The choice of such materials is forced by the high temperatures the system has to endure during the cleaning and deposition processes, which could induce thermal stress and deformation in the substrate if the proper materials are not employed. The sample holder is sketched in fig. 3.5.

Once the Si substrate is fixed on the holder, it is inserted in the load-lock (2) and in the preparation chamber (4) afterwards. Here, with the help of a metal finger, a current of 0.30 A propagates through the sample for 12 hours in order to heat it above  $400^\circ\text{C}$ , allowing the desorption of the chemisorbed contaminants. This step is especially effective in the removal of water molecules from the Si surface. Finally, the substrate is brought to the CVD chamber (5) where it is heated up to around  $1150^\circ\text{C}$  in  $\text{H}_2$  atmosphere, a value above the silicon oxide sublimation temperature. This procedure removes the non-stoichiometric native oxide and leaves an exposed Si surface clean but irregular and corrugated, requiring a reconstruction before the heterostructure deposition. To this aim, a Si layer is grown at  $800^\circ\text{C}$  via CVD of silane, allowing to restore a planar Si surface with high crystalline quality.

Up to this step the temperature is monitored by the pyrometer previously calibrated considering the Si emissivity, which therefore cannot be employed during the deposition processes that follow, since the emissivity changes too much according to the  $\text{Si}_{1-x}\text{Ge}_x$  relative concentrations and to the covering of the Si surface during all the stages of the deposition process. The tuning of the temperature during the

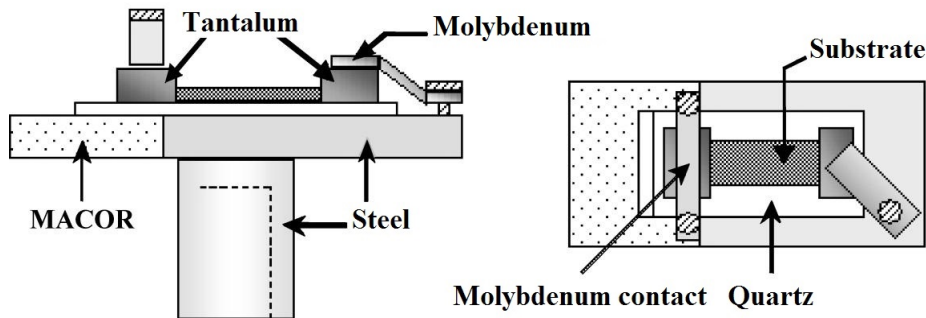


Figure 3.5: Sample holder side and top view.

growth process can be performed exploiting its correspondence with the injected current provided by the power supply. Since the sample temperature at each step is determined by a specific value of current, a temperature-current calibration can be performed on the silicon substrate before any other deposition and the use of the pyrometer can be avoided.

### 3.4 Virtual substrate

After the Si substrate preparation, the deposition process can take place starting from the growth of the virtual substrate. This element is necessary because of the high lattice mismatch between the Si substrate and the heterostructure with high Ge content, and serves as a linking layer collecting the structural defects and avoiding their propagation through the structure. The results of the analysis carried in section 1.4.1 suggest that the reverse graded virtual substrate is the best option, and thus it is the one employed in the realization of the samples investigated in this work.

Before going into details a list of the required steps needed for a proper virtual substrate growth is given:

- Ge seed layer deposition at 340°C (25 min).
- High temperature Ge deposition at 600°C and 700°C (35 min).
- Annealing at 800°C (20 min).
- High relaxation Ge deposition at 500°C (45 min).
- $\text{Si}_{1-x}\text{Ge}_x$  step graded layers deposition at 500°C (40 min).
- $\text{Si}_{0.18}\text{Ge}_{0.82}$  thick layer deposition at 500°C (230 min).

The virtual substrate growth starts with the deposition of a Ge seed layer, which covers the Si substrate and collects most of the defects induced by the high lattice mismatch. The deposition takes place in 25 minutes at the substrate temperature of 340°C and pressure of 4 mTorr. The pressure is set by the balance of the injected gas flow and the pumping volume, and can therefore be adjusted not only varying the amount of gas filling the CVD chamber but also reducing the aperture of the valve separating the chamber from the turbo-molecular pump. This convenient procedure allows to limit the gas consumption and waste, an attractive aspect for affordable industry production. However, a constant and homogeneous flow of precursor gas has to be maintained, considering that the seed layer deposition is a delicate step that risks to prevent a good quality sample realization. For example it is important to recall that special attention has to be paid to the deposition temperature, since too high values force the growth not to be planar but with islands, and too low values prevent the germane pyrolysis.

Once a good quality seed layer has been grown and an epitaxial planar deposition is established, it is possible to increase the temperature to 600°C and then to 700°C for a total amount of time around 35 minutes. This allows not only to increase the growth speed (thus reducing the time needed to complete the deposition) but also to reduce the density of defects introduced during the deposition.

After an annealing process at 800°C for 20 minute with the aim of reducing the defect density, a thick layer of Ge is grown for 45 minutes at a temperature of 500°C and pressure of 1.20 mTorr. This step results in a Ge layer around 1  $\mu\text{m}$  with a high relaxation level and low defect density.

$\phi(\text{GeH}_4)$ (sccm)	$\phi(\text{SiH}_4)$ (sccm)	$\Delta t$ (min)	$p$ (mTorr)	$x$
2.1	0.6	10	4	0.955
2.1	1.1	10	4	0.910
2.1	1.6	10	4	0.865
2.1	2.1	10	4	0.820

Table 3.1: Example of step graded  $\text{Si}_{1-x}\text{Ge}_x$  layers deposition conditions: precursors injected flows  $\phi(\text{GeH}_4)$  and  $\phi(\text{SiH}_4)$  (1 sccm =  $1.6 \cdot 10^{-2} \text{ cm}^3/\text{s}$ ), deposition time  $\Delta t$ , pressure  $p$  and Ge layer concentration  $x$ .

Starting from the relaxed Ge surface it is possible to proceed with the *step graded* layer deposition at  $500^\circ\text{C}$ , consisting in a group of four layers with increasing Si concentration realized by injecting both germane and silane in the CVD chamber, thus allowing the growth of Si and Ge at the same time (co-deposition). Increasing the silane concentration in the chamber at each step it is possible to grow four  $\text{Si}_{1-x}\text{Ge}_x$  layers with Ge concentration decreasing, for example, from  $x = 1$  to  $x = 0.82$ , i.e. from 100% to 82% with 4.5% difference between each adjacent layer. The same procedure applies to any final Ge concentration needed, e.g. 80% or 85%. The proper precursor flows needed to achieve the desired concentration are estimated theoretically and then checked experimentally with XPS. Giving the deposition conditions reported in table 3.1, each layer results in a thickness of 150 nm.

In order to achieve the final crystal quality and surface roughness, a  $1.5 \mu\text{m}$  thick SiGe layer with the same Ge concentration of the last step graded layer (e.g.  $\text{Si}_{0.18}\text{Ge}_{0.82}$  as above) is grown at  $500^\circ\text{C}$  with 0.80 mTorr of pressure, as final layer of the virtual substrate. The concentration is set to match the one of the SiGe barriers needed to realize the desired QW heterostructure.

Structural characterization has been performed on the realized virtual substrates

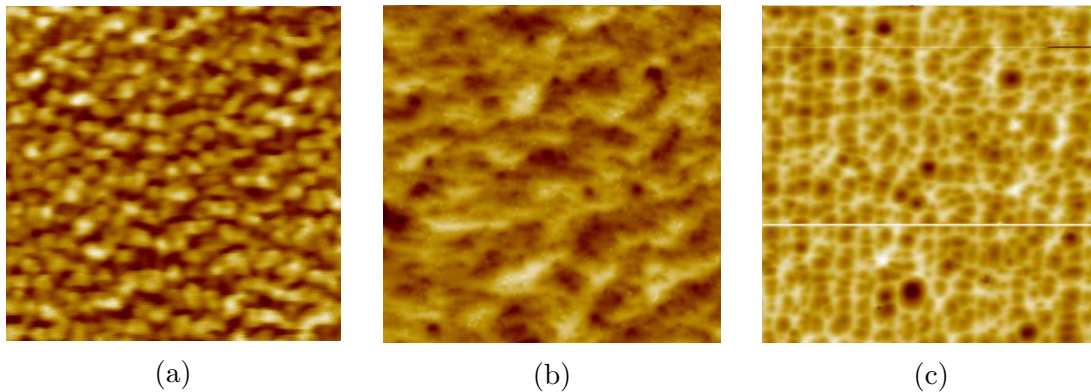


Figure 3.6: AFM images of a virtual substrate at different growth stages: (a)  $1.5 \times 1.5 \mu\text{m}^2$  image of a Ge seed layer on Si(100) substrate; (b)  $20 \times 20 \mu\text{m}^2$  image of the virtual substrate after the  $700^\circ\text{C}$  deposition step; (c)  $40 \times 40 \mu\text{m}^2$  image of the final virtual substrate after the reverse graded layers deposition.



in order to optimize the growth procedure. The AFM images in fig. 3.6 show the comparison between the results obtained at different stages of the virtual substrate growth. While the seed layer appears with a corrugated surface with a maximum excursion in the  $z$  direction of 14 nm, the increase in the growth temperature allows to obtain a flatter surface characterized by a lower excursion reduced by almost 30%. The final result of a virtual substrate deposition is reported in the last panel of the figure, in which is shown the low surface defect density suitable for the realization of a proper heterostructure on top, with a maximum excursion of 20 nm.

A STEM image obtained from a reverse graded virtual substrate realized with the described procedure is reported in fig. 3.7. From the image it is clear how the lower layers of Ge exhibit a very high defect density due to the lattice mismatch with the Si substrate, as happens also at each interface between the step graded layers. These interfaces, however, are able to block the threading dislocations which otherwise would have propagated through the whole structure, and the result is a final layer with a very low defect density ( $N_{TD} < 3 \cdot 10^6 \text{ cm}^{-2}$ ). XRD measurements show how the realized virtual substrate exhibit a residual strain resulting in a lattice parameter peculiar of  $\text{Si}_{0.12}\text{Ge}_{0.88}$  alloys. This aspect has to be taken into consideration in designing the samples, since a lattice strain induces variations in the electronic properties of the system, as discussed in chapter 1.

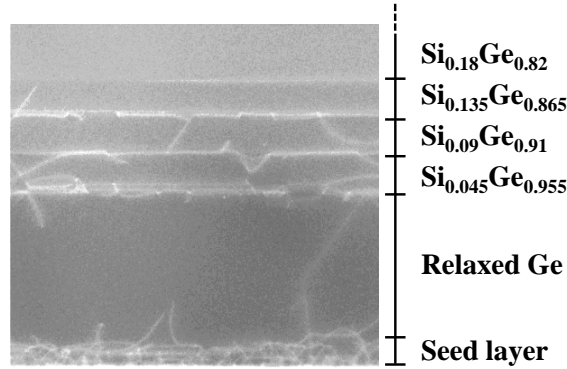


Figure 3.7: STEM image of the reverse graded virtual substrate of sample S2 [68].

### 3.5 Ge/SiGe heterostructures

A proper virtual substrate allows the deposition of the QW heterostructure with low defect density and high crystal quality. The realized samples consist in a periodic repetition of Ge QWs and  $\text{Si}_{0.18}\text{Ge}_{0.82}$  barriers resulting in strain-compensated structures of two possible designs: the MQW and the ACQWs, as described in chapter 2. The first group includes the samples with several single QWs isolated from each other by thick barriers to prevent any interaction among them, while the second group includes the samples in which the symmetry is broken to engineer the wavefunction overlap and hence the ISB relaxation times.

In order to perform the optical characterization through absorption spectroscopy, n-type doping of the structures has been performed via phosphine ( $\text{PH}_3$ ) co-deposition, resulting in charge transfer to the QW subbands. With the direct doping

technique, the donor phosphorous atoms are introduced in the lattice structure of Ge, hence directly in the QW layers. On the contrary, the modulation doping technique consists in the  $\text{PH}_3$  co-deposition within the SiGe layers, resulting in a charge transfer from the barriers to the wells. In this case, the positive charge distribution is spatially separated by the electron density in the wells, and a strong electric field can be established.

Due to the delicate nature of the ACQW samples, the direct doping technique has been chosen in order to avoid the band bending introduced with the modulation doping technique (see section 2.5), which instead is used as standard procedure to populate the single QWs. In some cases, the barrier doping is performed leaving a spacer layer between the well and the doped region, in the attempt to minimize the Coulomb interaction with the ionized donor atoms. Specially in the presence of spacer layers, the modulation doping technique was found to be weak in transferring the electrons from the donors to the well and a high doping concentration of  $10^{18} \text{ cm}^{-3}$  is needed to ensure a sufficient well population. This aspect will be confirmed also by the multi-band calculations that will be discussed in chapter 4. The direct doping technique is instead more efficient and a lower doping concentration of  $2 \cdot 10^{17} \text{ cm}^{-3}$  is therefore employed. The real amount of electrons transferred into the well has anyway to be determined after the growth process and can significantly differ from the expected value in some cases. The growth parameters used in the realization on the investigated samples are summarized in table 3.2.

The growth process of the periodic structure can be controlled by a program in Labview platform, which allows to load a text file with all the instructions within. The file consists in a table in which every line is a step of the process and the columns represents the growth parameters, with the corresponding values at each line (step). The program simply reads the file and open (or close) the valves for gas insertion accordingly, for a time interval specific of each step.

Sample	$d_w$ (nm)	$d_b$ (nm)	$N_W$	$n_{3D}$ ( $10^{18} \text{ cm}^{-3}$ )
S1	13.5	10+ <b>10</b> +10	20	1
S2	24	10+ <b>10</b> +10	20	1
S3	10	<b>30</b>	10	1
S4	12	<b>30</b>	15	1
S5	24	<b>30</b>	10	1
S6	24	<b>30</b>	20	1
S7	12	4+ <b>22</b> +4	10	1
S8	<b>13</b> +4.5*	30	20	0.2
S9	<b>15</b> +5.5*	30	20	0.2
S10	<b>15</b> +3.5*	30	20	0.2

Table 3.2: Samples growth parameters: Ge well width  $d_w$ , SiGe barrier width  $d_b$ , number of periods  $N_W$ , charge density  $n_{3D}$ . Bold numbers indicate the doped layers, eventually sandwiched between spacer layers. (\*)For ACQW samples a thin barrier of 1.5 nm is implied between the two wells.

The growth starts with a  $\text{Si}_{0.18}\text{Ge}_{0.82}$  layer as connection with the virtual substrate and continues with the periodic QW heterostructure finally covered with a thick  $\text{Si}_{0.18}\text{Ge}_{0.82}$  layer for protection. At the end of every step a hydrogen purge is inserted, in order to expel every gas residue from the previous step and perform the next one in clean and uncontaminated environment. Every step is performed at  $500^\circ\text{C}$  with a pressure of 1.20 mTorr, conditions in which the growth speed is around 6 nm/min for pure Ge and slightly lower for  $\text{Si}_{0.18}\text{Ge}_{0.82}$ .

In fig. 3.8 the TEM and AFM images of sample S7 are reported, showing how the automatic growth procedure results in heterostructures with the desired layer thicknesses and high precision. In particular, the STEM image demonstrates that a composition variation around 5% between layers is clearly discerned and the interface roughness can be estimated to be lower than 0.4 nm. The absence of extended defects in the structure evidences the high quality obtained with the described deposition procedure. Moreover, the surface topography reported in the AFM image shows the very low surface roughness achieved, which is around 3 nm.

The spatial periodicity of the grown heterostructure obtained by the TEM analysis can be confirmed by XRD measurements, as in the example reported in fig. 3.9. The image displays the reciprocal space map of sample S6 and the intensities of the diffracted beams as a function of the collecting angle  $\Theta$  along the (400) reflection. The experimental data have been compared to the results of a simulation algorithm based on a quasi-kinematical approximation (neglecting defects diffusion), which is also displayed in the figure. The XRD analysis also allowed to retrieve the lattice parameter of each layer and thus the strain in the virtual substrate and in the strain-compensated QW heterostructure. In the case of sample S6 in fig. 3.9, the structure is found to be partially compensated with an in-plane compressive strain of  $\epsilon_{\parallel} \simeq -4.7 \cdot 10^{-3}$  in the Ge wells and  $\epsilon_{\parallel} \simeq 2 \cdot 10^{-3}$  in the SiGe barriers.

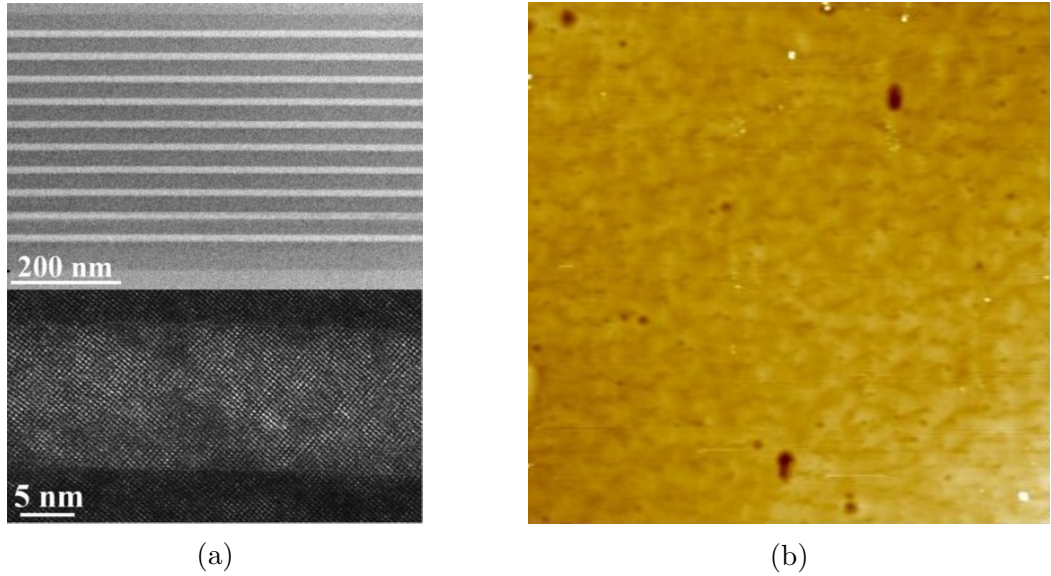


Figure 3.8: Sample S7 structural analysis: (a) STEM-HAADF images at increasing magnifications [65]; the Ge QWs are apparent in light grey while the SiGe barriers in dark grey. (b)  $50 \times 50 \mu\text{m}^2$  AFM image.

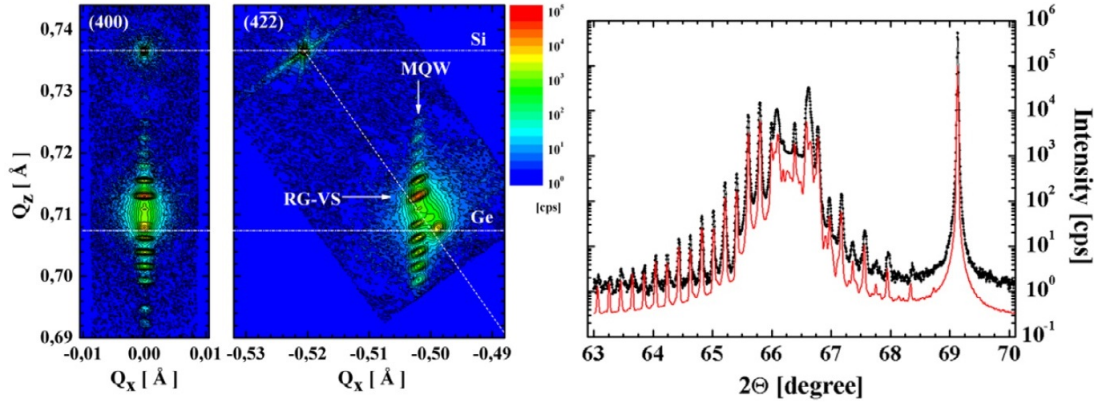


Figure 3.9: Sample S6 reciprocal space maps of (400) and (422) reflections obtained with the XRD analysis (left panel). The expected  $Q_z$  positions for Si and Ge are marked by dash-dotted lines. The dashed line in the (422) reciprocal space map points toward the origin of reciprocal space and marks the line of fully relaxed (cubic) materials. A specular (400)-XRD scan of the same sample in comparison to a simulated curve is shown in the right panel. The simulated curve is shifted to lower intensities for better visibility [68].

### 3.6 Waveguide realization

Before the optical characterization could be performed, the samples need to be shaped in a waveguide configuration, in which the sample surface is coated with a metal layer and the opposite face (the back of the Si wafer) is used to confine the waveguide modes via total internal reflection [14, 76]. The coating procedure has been performed at the “Institute for photonics and nanotechnologies” (IFN) of the “National Research Council” (CNR) and it is necessary due to the employed characterization techniques which rely on the radiation absorption by the system. In fact, as introduced in section 2.3, the radiation fraction absorbed by the QW would have been almost null if the metal coating were absent, because of the boundary conditions of the Maxwell equations describing the radiation propagation through the waveguide. Here, the solutions exhibit a node in the  $z$ -component of the electric field at the sample-vacuum interface, i.e. in the QW active region. The metal on the surface modifies the boundary conditions and the new solutions of the Maxwell equations represent a stationary wave with an antinode in the  $z$ -component of the electric field, as depicted in fig. 3.10. The coupling with the ISB transitions becomes therefore possible allowing the radiation absorption according to what described in section 2.2 [3].

The samples are coated with a gold layer of 100 nm separated from the SiGe sample surface by a thin titanium layer around 10 nm which works as glue between the two materials. The evaporation is performed heating the solid metals in their crucibles by an electron beam, until the melting temperature is reached. To ensure an uniform deposition of the metals on the surface, the samples have to be located at least at 50 cm from the crucibles, at a distance too large to allow the sublimated metals to reach it. In order to increase the mean free path of the particles is therefore necessary to perform the evaporation in vacuum conditions, at a pressure around

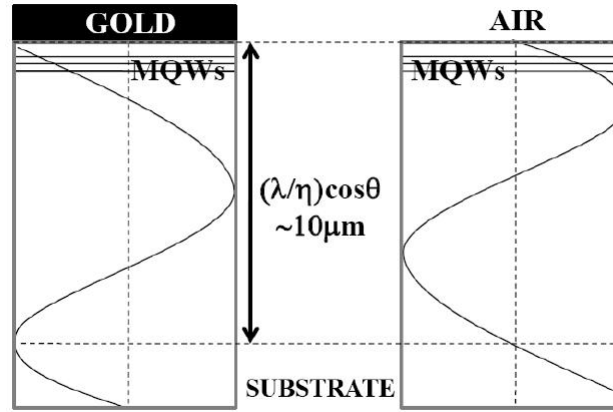


Figure 3.10: Steady solution of the Maxwell equations inside the waveguide with and without the surface metal deposition [3].

$10^{-6}$  Torr. The deposited thickness is monitored by a quartz crystal microbalance, an instrument able to retrieve the amount of the deposited element starting from its atomic mass.

After the metal deposition, the sample can be shaped in a waveguide geometry similarly to the one depicted in fig. 2.10. This process consists in two steps: the sample cut and the facets lapping. The cut is performed using a saw with diamond wire and it is needed to avoid the total radiation absorption by the sample, allowing a sufficient fraction to exit the waveguide and be measured. To this aim, the samples are generally cut in small pieces of 3 mm, which therefore corresponds to the waveguide length. The opposite facets of the waveguide are then lapped to obtain the desired angle of  $70^\circ$  and to smooth as much as possible the interface, limiting the diffusion of the incident radiation. The angle is chosen to be close to the Si Brewster angle of  $73.7^\circ$ , at which the reflected component of the incident radiation vanishes. The sample is therefore glued to a proper metallic support and mechanically lapped using several sandpaper sheets with different grain density. The coarse-grained sheet allows to shape the facet, while the finer ones smooth the surface. The result of a lapping process suitable for optical characterization measurements is sketched in fig. 3.11.

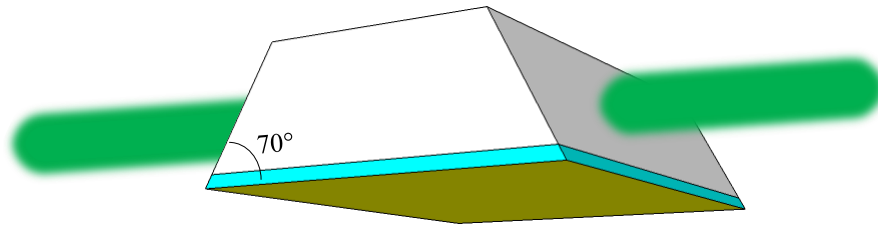


Figure 3.11: Sample geometry after the lapping process performed to obtain final smooth facets at an angle of  $70^\circ$ , close to the Brewster angle of  $73.7^\circ$ . The QW active region close to the metallic surface is highlighted in light blue (not to scale).



# 4

## Optical characterization

The inter-subband (ISB) transition study presented in this thesis mainly focuses on two different aspects: the absorption spectra of the steady-state electronic configuration and the relaxation times of the out-of-equilibrium excited states. The first aspect is investigated using the Fourier Transform InfraRed (FTIR) spectroscopy to obtain transition energies and linewidth broadening, while relaxation times are estimated from pump-probe measurements eventually combined with Time-Domain Spectroscopy (TDS) when needed.

### 4.1 Fourier Transform InfraRed spectroscopy

Part of the samples optical characterization has been performed using the FTIR spectroscopy in collaboration with the IRS group at the department of Physics of the “Sapienza Università di Roma”. This technique allowed us to obtain the absorption spectra of the samples in a wide range of energies, and thus allowing the study of the ISB transitions within the quantum wells. This kind of spectroscopy is based on a Michelson interferometer, in which the beam from the radiation source is directed towards a beam splitter that separates it in two identical components. The two beams recombine after being reflected by a fixed and a moving mirror generating an interference pattern called *interferogram*, which depends on the optical path difference caused by the moving mirror.

If the source beam has only one frequency component, the detected signal is a simple sinusoidal oscillation, while it is a more complicated function if the source covers a wide range of frequencies. In this case, the interferogram is the result of the interference generated by each single-frequency component of the source spectrum, which can be recovered computing the Fourier transform of the interferogram. In fact, the time-dependent electric field of a plane wave can be expanded in its Fourier components:

$$\mathbf{F}(\mathbf{r}, t) = \frac{1}{2\pi} \int_{-\infty}^{+\infty} d\omega B^{\frac{1}{2}}(\omega) e^{i(\omega t - \mathbf{k} \cdot \mathbf{r})} \quad (4.1)$$

where  $B(\omega)$  is the radiation source power spectrum. If  $\bar{T}$  is the wave period and  $\delta$  the optical path difference, the intensity at the detector is

$$I(\delta) = \frac{c}{8\pi\bar{T}} \int_{-\bar{T}/2}^{+\bar{T}/2} dt \left| \mathbf{F}\left(\mathbf{r}, t + \frac{\delta}{c}\right) + \frac{1}{2}\mathbf{F}\left(\mathbf{r}, \frac{\delta}{c}\right) \right|^2 \quad (4.2)$$

Exploiting the symmetry with respect to the point of zero path difference ( $\delta = 0$ ), the Fourier image of the interferogram  $I(\delta)$  gives the source power spectrum:

$$B(\omega) = \frac{32\pi^2\bar{T}}{c^2} \int_{-\infty}^{+\infty} d\delta \left( I(\delta) - \frac{I(0)}{2} \right) e^{-i\omega t} \quad (4.3)$$

The presence of a sample crossing the beam has been neglected so far, and the function  $B(\omega)$  is indeed the power spectrum of the radiation source with every frequency component. With the presence of the sample, however, the calculated function will miss all the frequency components absorbed during the propagation through the sample, and thus equation 4.3 will represent the sample transmittance function. A schematic description is given in fig. 4.1.

The procedure explained here to obtain the transmittance spectra implies ideal conditions. As evident in equation 4.3, in fact, computation of the Fourier transform would theoretically need a continuous change in the optical path variable  $\delta$  in an infinite integration range. These conditions can not obviously be satisfied in real experiments and the result is the appearance of artifacts in the spectrum. Fortunately, nowadays is possible to limit and partially fix these unwanted effects using complicated algorithms, as profusely described in reference [77].

#### 4.1.1 Setup description

The FTIR measurements have been performed using the interferometer Bruker IFS 66v/S, a versatile tool able to investigate spectra from the far-infrared to the ultraviolet region. Its components are directly controlled by a dedicated software and kept in low vacuum conditions ( $\sim 10^{-3}$  Torr) to prevent absorption from atmospheric molecules. The high versatility allows the acquisition of either transmission or reflection spectra (with different components and geometries) using different radiation sources and detectors, with a resolution up to 0.01 meV. This value depends on several parameters and it was set to 1.5 meV in order to acquire up to 100 spectra/sec

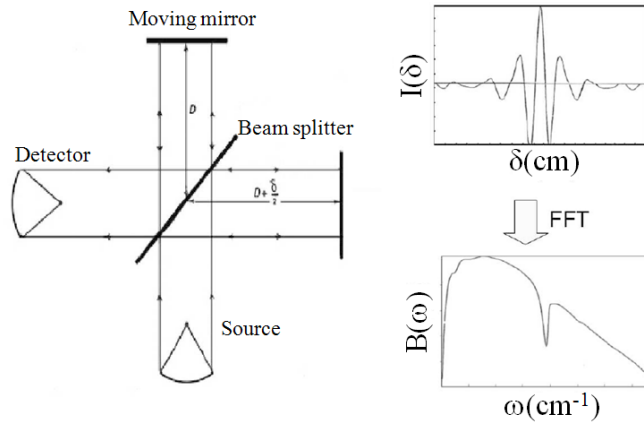


Figure 4.1: Michelson interferometer, interferogram  $I(\delta)$  and source spectrum  $B(\omega)$ .



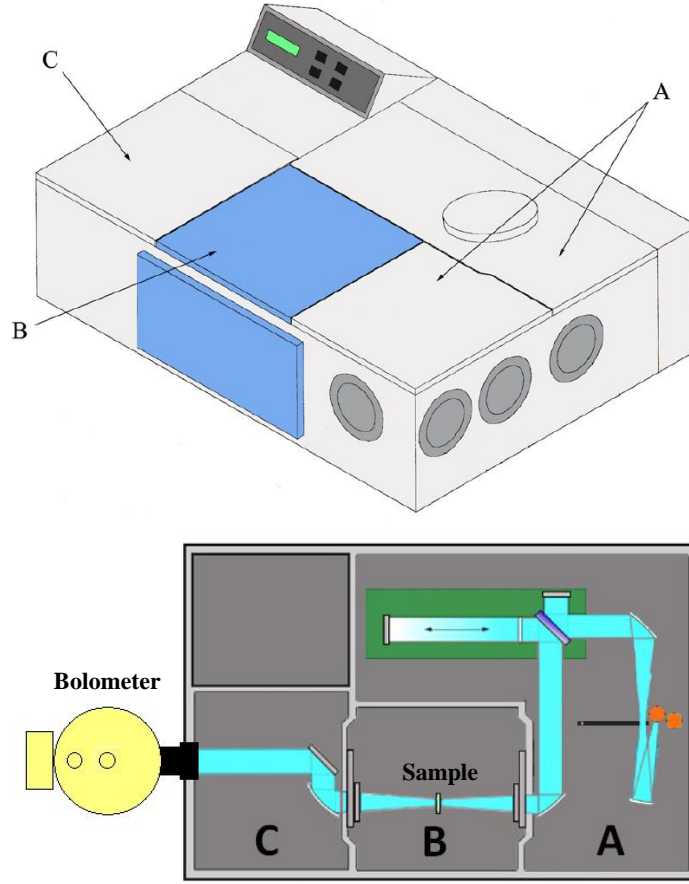


Figure 4.2: Interferometer schemes.

with enough resolution to evaluate the ISB transition energies and linewidths. The interferometer is divided into several independent compartments, as schematically shown in fig. 4.2.

In compartment A the appropriate radiation source is mounted accordingly to the desired spectral range to investigate. The selected source used to study the ISB transitions of our samples in the THz range is a SiC glow-bar emitting a black body radiation mainly in the interval 10-80 meV. Radiation is guided towards the beam splitter using a system of parabolic mirrors, and the two generated beams are sent to the fixed and moving flat mirrors. After recombination, another parabolic mirror focuses the light in the center of compartment B, where the sample is conveniently mounted to allow measurements from 7 K to room temperature. Sample cooling is needed to force carriers only in the lowest subband, in order to study ISB transitions in absorption configuration starting from the system ground level.

The cooling process and the steady low temperature retention are achieved using the cryostat described in fig. 4.3. A continuous liquid helium flow cools down the copper cold finger where the samples are mounted. The cold finger is protected by a thermal shield and isolated from the rest of the apparatus to keep high vacuum conditions to prevent ice formation from the water vapor present in the residual atmosphere inside the interferometer. Pressure around  $10^{-6}$  Torr is kept constant in the cold finger vacuum chamber using a dedicated membrane/turbomolecular

pumping system, connected to the cryostat through a vacuum valve. Since the cold finger can hold two samples, a manual height regulator guarantees not only the right overlapping with the incident radiation, but also allows measurements on both mounted samples without the need of heating and ventilate the apparatus.

Right before the cryostat, compartment B can host a polarizer. As discussed in section 2.2, ISB transitions are allowed only with TM-polarized incident light, which in our case is instead a non-polarized black body radiation generated by the source through thermal emission. The use of a polarizer is thus needed in order to select the TM component of the incident radiation. The polarizer we used here consists in a grid of thin aluminium wires with a period of 400 nm, able to block the radiation polarized along them and let the normal-polarized component get through. The electric field parallel to the grid is in fact absorbed by the aluminium electrons that oscillate from one side of the wires to the other, while the normal-polarized component can not induce any oscillation and can therefore cross the polarizer without being absorbed. A  $90^\circ$  rotation of the polarizer allows the acquisition of spectra also in TE polarization.

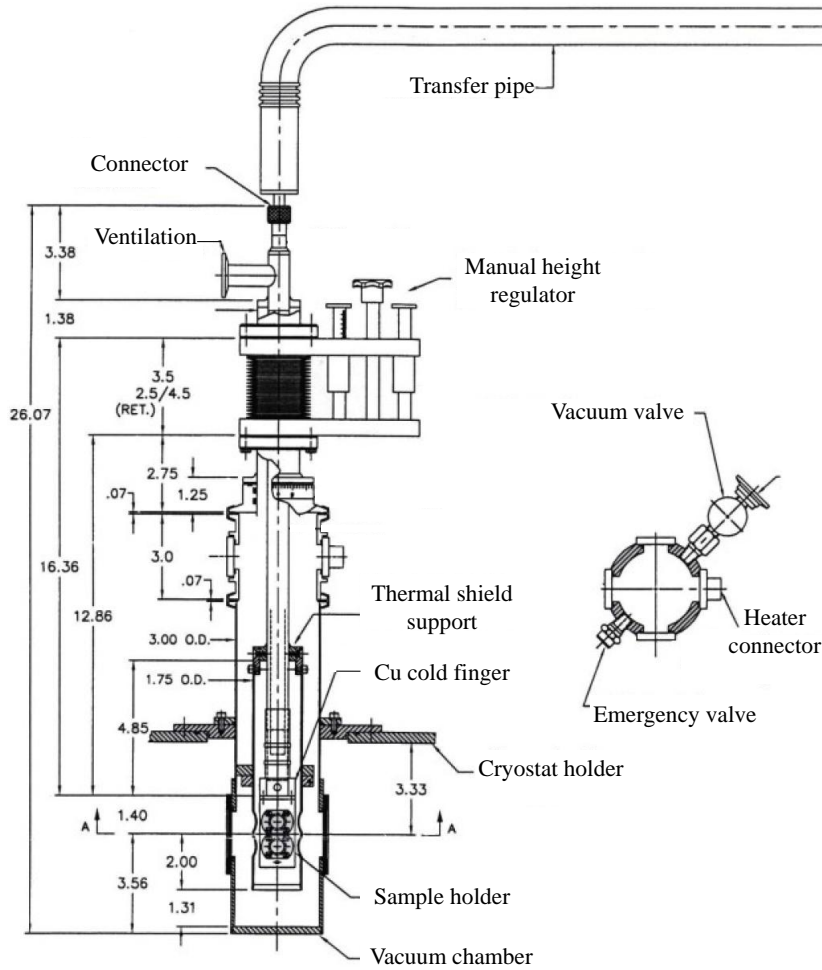


Figure 4.3: Cryostat description.

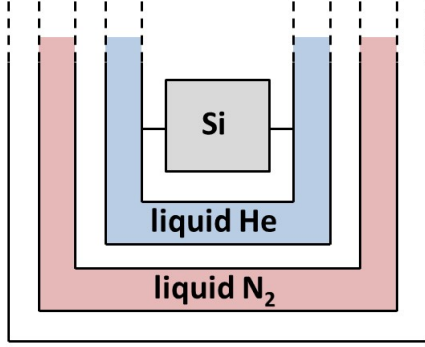


Figure 4.4: Bolometer scheme and picture.

After propagating inside the sample, the radiation enters compartment C where the detectors are generally placed. In our case, the beam is guided outside the interferometer, where the far-infrared detector is located. The one used in this work is a semiconductor bolometric detector, whose scheme is shown in fig. 4.4.

This bolometer consists in ultra-high vacuum cavities that isolate two compartments with liquid helium at the temperature of 4.2 K and liquid nitrogen at 77 K. This system guarantees an 8-hours lasting steady low temperature of a heavy-doped silicon crystal located in the center. When radiation hits the crystal, the temperature rise induces a resistivity change proportional to the radiation intensity. The calculated value is sent to the computer that keeps track of the intensity for each step of the moving mirror, generating the interferogram.

### 4.1.2 Acquisition geometry

After the lapping process described in section 3.6, the sample waveguides are mounted on the cryostat cold finger using two small brass blocks to hold them in position. The two small blocks have also the function of blocking any radiation apart from the light propagating through the sample. This configuration, depicted in fig. 4.5, avoids the detector saturation that could occur if part of the incident beam propagates beside and not inside the sample. In the adopted geometry the incident radiation hits the sample lateral facet with an angle of  $70^\circ$ , very close to the Si Brewster angle ( $73.7^\circ$ ) to limit interface reflection, and leaves the waveguide with same angle.

Recalling equation 2.29, in order to calculate the bi-dimensional absorption coefficient  $\alpha_{2D}$ , the propagation angle  $\theta$  and the parameter  $M$  are needed. The former can be easily evaluated using the Snell law with incident angle of  $\alpha_i = 20^\circ$  (with respect to the normal of the surface) and the refractive angle  $\alpha_r$ , assuming valid the geometrical optics approximation:

$$\eta_a \sin(\alpha_i) = \eta_{Si} \sin(\alpha_r) \quad \Rightarrow \quad \alpha_r = 5.74^\circ \quad (4.4)$$

where  $\eta_a = 1$  and  $\eta_{Si} = 3.42$  are the air and Si refractive indexes, respectively.

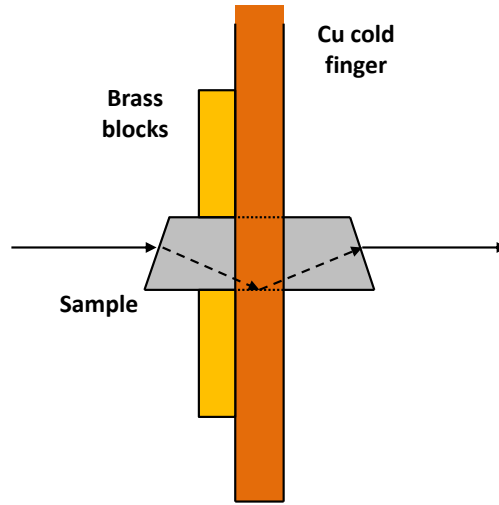


Figure 4.5: Sample waveguide mounted on the cryostat using two small brass blocks screwed on the copper cold finger.

Considering the geometric scheme in fig. 4.6 it is possible to calculate the radiation propagation angle  $\theta$  inside the sample:

$$\beta = 180^\circ - (90^\circ - 70^\circ) \Rightarrow \theta = 90^\circ - (180^\circ - \alpha_r - \beta) = 75.74^\circ \quad (4.5)$$

Concerning the parameter  $M$ , it is the number of times the light crosses the active region and thus depends on the waveguide geometrical dimensions. Its value is twice the number of internal reflections because the light propagates through the active region once before the reflection and once after. Following the scheme in fig. 4.6 and considering the samples thickness equals to the Si wafer thickness of  $h = 0.7$  mm (the CVD-grown layers are always less than  $5 \mu\text{m}$  in total), the waveguide length  $L$  needed to have only one internal reflection is

$$L = 2 \left( \frac{h}{2 \cos(\theta)} \right) \sin(\theta) = h \tan(\theta) = 2.75 \text{ mm} \quad (4.6)$$

Although this single-pass geometry condition, which leads to  $M = 2$ , is not much important in FTIR measurements, it is indeed important in pump-probe experiments. When carrier dynamics are studied, it is crucial to avoid the overlapping of phenomena happening in different part of the waveguide at different times because they lead to misinterpretations. Therefore, the waveguides have to be as short as possible in order to consider the interaction within the sample as it is happening almost at the same time in every point. In 2.75 mm long waveguides, the light enters and exits in few picoseconds, preventing any evaluation of time-dependent phenomena that take place in shorter time intervals.

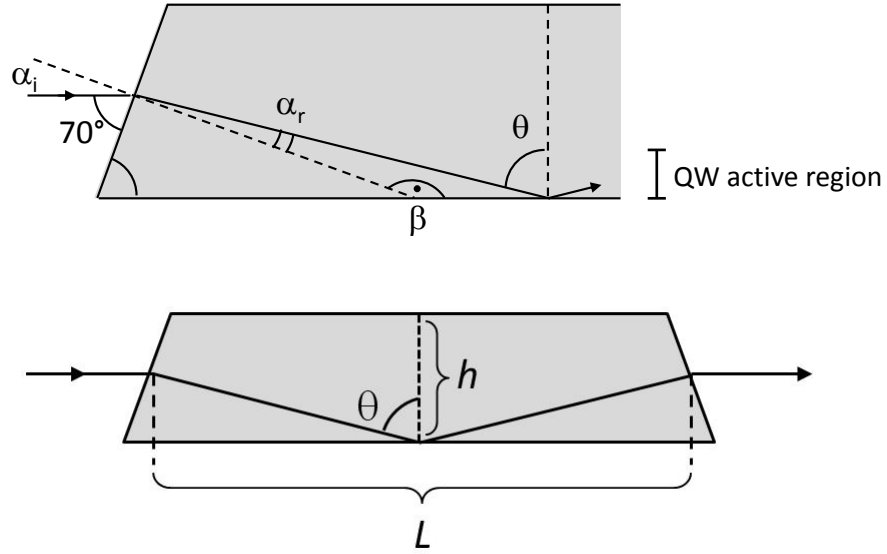


Figure 4.6: Light propagation inside the sample waveguide assuming valid the geometrical optics approximation (upper figure) and single-pass geometry waveguide scheme (bottom figure).

### 4.1.3 Bi-dimensional absorption coefficient $\alpha_{2D}$

Transmittance spectra obtained from FTIR measurements have been used to characterize the samples and highlight ISB transitions features. In particular, the bi-dimensional absorption coefficient  $\alpha_{2D}(E)$  can be evaluated from the waveguide transmittances using the following relation:

$$\alpha_{2D}(E) = -\frac{\ln [T(E)] \cos(\theta)}{CMN_W \sin^2(\theta)} \quad (4.7)$$

where  $T(E)$  is the waveguide transmittance,  $N_W$  is the number of QW periods present in the sample,  $M$  the number of times the light crosses the QW active region with the propagation angle  $\theta$ , and  $C = 1.5$  the electric field amplification factor close to the metal-semiconductor interface (see section 3.6).

In order to study only the ISB transitions properties, all other contributions to the transmittance have to be excluded. This extraction procedure can be accomplished exploiting the TM polarization selection rule valid for the ISB transitions only. In fact, any other contribution to the acquired spectra is independent on the incident polarization and can be therefore ruled out calculating the *dichroic signal*, i.e. the ratio of the transmittance signals obtained in the two different polarizations TM and TE with the use of the polarizer. Moreover, it is necessary to take into account any possible anisotropy of the apparatus components that may lead to slight polarization dependent differences. These differences can be canceled by a simple normalization operation, acquiring the same spectrum with and without the sample. Referring with  $S_{TM}$  and  $S_{TE}$  to the sample spectra and with  $S_{TM}^0$  and  $S_{TE}^0$  to the reference spectra acquired in absence of the sample, the normalized transmittances are:

$$TM(E) = \frac{S_{TM}}{S_{TM}^0} \quad \text{and} \quad TE(E) = \frac{S_{TE}}{S_{TE}^0}. \quad (4.8)$$

We therefore define the dichroic signal as the ratio between the normalized transmittances:

$$T(E) = \frac{TM(E)}{TE(E)} \quad (4.9)$$

In the dichroic signal only the polarization dependent features of the sample are present, while all other absorption phenomena are normalized. In the specific case of the samples studied here, the only polarization dependent effects are the ISB transitions within the QWs, which therefore are the only features present in the dichroic signal.

Fig. 4.7(a) shows an example of the normalized transmittances acquired with the two different polarizations of the incident radiation. In both spectra the absorption from hydrogen-like phosphorous donor atoms are present and they will be canceled in the dichroic signal because of their polarization independent nature. At lower energies, instead, it can be noticed an absorption dip present in the TM transmittance only, which thus is the mark of an ISB transition at that energy.

In fig. 4.7(b) it is reported the dichroic signal of sample S1 at 30 K. The spectrum shows a minimum around 30 meV with a linewidth around 5 meV, while the transitions within the hydrogen-like donor atoms have been canceled in the process, even if not exactly. This is an example of how the dichroic signal highlights only the ISB transitions, hiding all the other contributions to the transmittance. Starting from the dichroic signal  $T(E)$ , the bi-dimensional absorption coefficient  $\alpha_{2D}(E)$  has been evaluated using equation 4.7.

At low temperature, the curves generally exhibit only a single peak at the energy of the ISB transition  $|0\rangle \rightarrow |1\rangle$ , i.e. the absorption by electrons in the lowest subband to the first excited subband. This is because at low temperatures only the fundamental level is populated and any other ISB transition apart from the  $|0\rangle \rightarrow |1\rangle$  is forbidden or too low in intensity.

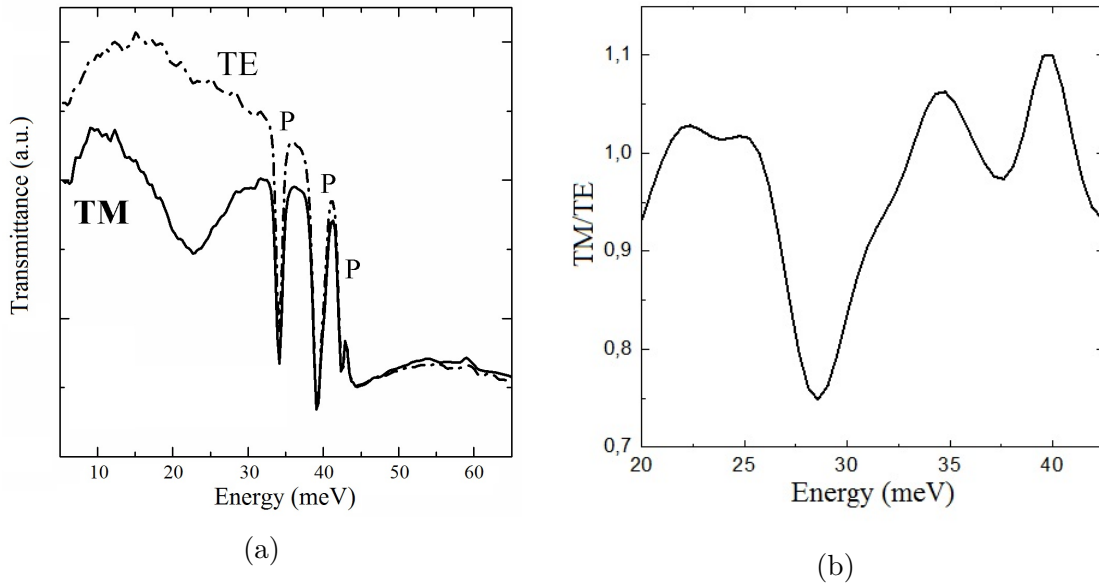


Figure 4.7: (a) Example of normalized transmittances in the two polarization TM and TE. (b) Dichroic signal  $T(E) = TM/TE$  of sample S1 at 30 K.

## 4.2 Degenerate pump-probe spectroscopy

In group-IV materials the optical phonon scattering is mediated only by the deformation potential because of the non-polar nature of the material, and not also by the Fröhlich interaction as it happens in III-V systems [78,79]. In this regard, fig. 4.8 reports the theoretically calculated transition rate  $W_{10}$  of the  $|1\rangle \rightarrow |0\rangle$  relaxation in Ge and GaAs QWs, as a function of the ISB transition energy  $E_{01}$  for different values of bi-dimensional electron density and temperature [80]. In the Ge wells the transition rate exhibits a monotonic increase as a function of the transition energy, with a drastic change around the optical phonon energy, especially for the empty-band calculation (only a single electron in subband  $|1\rangle$ ). On the contrary, the transition rate in GaAs systems is characterized by a sharp resonance at the phonon energy. In fact, the coupling term describing the electron-phonon interaction in Ge does not depend on the exchanged momentum, and the scattering rate behavior resembles a step function. In polar materials like GaAs, instead, the coupling term is inversely proportional to the squared modulus of the exchanged momentum and a sharp resonance is thus present at the optical phonon energy, since in this case the initial and final states have the same momentum. In both materials, the presence of carriers in the excited subband has the effect of smearing the drastic increase of the transition rate for subband energy separation close to the phonon energy. Besides the absence of the sharp resonance, it is important to notice that the transition rate in group-IV QWs is predicted to reach values up to 60 times smaller if compared to the corresponding values in III-V systems. As a consequence, the predicted values of the relaxation times reach several tens of picoseconds up to room temperature even for ISB transition energy close to the optical phonon one. This is one of the main reasons why the group-IV QW systems are currently very attractive for designing ISB unipolar emitters [5, 81–84].

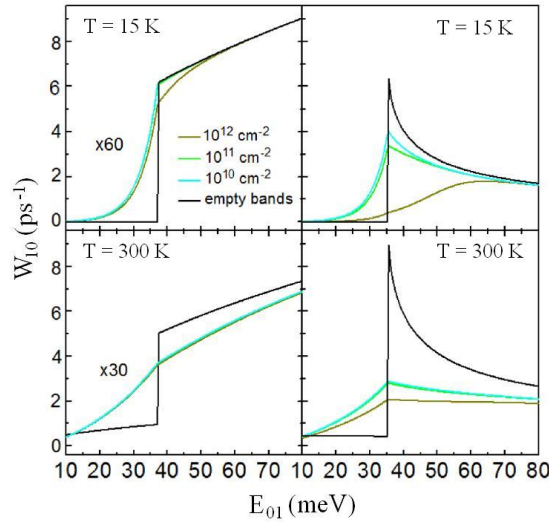


Figure 4.8: Simulated transition rate in Ge (left panels) and GaAs (right panels) QWs as a function of the ISB transition energy, temperature and electron density in the excited subband. Calculations on both systems consider a single effective phonon energy of 37 meV and 36 meV, respectively.



To verify the theoretical predictions, pump-probe experiments have been performed, in which a portion of the electron charge density is pumped into the excited state and the time needed by the system to relax back to the equilibrium conditions is measured. In this regard, seminal investigation on the relaxation times in our samples has been conducted via degenerate pump-probe experiments at the FELBE facility of the Helmholtz-Zentrum Dresden-Rossendorf. In this experimental setup, samples are optically pumped with free-electron laser (FEL) pulses to populate the first excited subbands and the relaxation dynamics back to the equilibrium is probed with the same pulses delayed in time. Pulses are emitted with repetition rate of 13 MHz and pulse length around 10 ps, while the emission wavelength can be tuned in the far-infrared range by changing the undulator gap of the FEL cavity [85]. The time interval between subsequent FEL pulses (77 ns) is long enough to ensure complete relaxation before the next pulse arrives. A sketch of the measurement configuration is given in fig. 4.9.

To perform degenerate pump-probe analyses, the energy of the pump and probe pulses is set to match the  $|0\rangle \rightarrow |1\rangle$  ISB transition energy obtained from previous FTIR experiments, while the pulse power delivered to the samples is adjusted in the range of 8-750 mW with the help of a set of attenuators (densities at focus around 1-100 kW/cm<sup>2</sup>). The transmitted intensity through the samples is recorded as a function of the pump-probe delay time and allows to retrieve the relaxation time of the excited states. The samples are shaped in suitable waveguides and mounted in the same cryostat described in section 4.1.1, while the coupling with the incident radiation is assured by the TM geometry, as imposed by the ISB transition selection rules. The quantity here monitored is the differential transmission change  $\Delta S/S = (S(t') - S_{off})/S_{off}$  calculated as the normalized transmitted intensity  $S(t')$  as a function of pump-probe delay time  $t'$  relative to the transmitted intensity  $S_{off}$  without pumping. The differential transmission change is measured at different pumping powers  $P$  and temperatures  $T$ , and the relaxation times  $\tau_{10}$  from the excited level  $|1\rangle$  to the ground level  $|0\rangle$  are extracted fitting the data to single or multiple exponential curves and compared to predictions obtained by calculation.

The theoretical framework in which the relaxation dynamics is investigated consists in an energy-balance model which allows to evaluate the measured differential transmission spectra  $\Delta S/S$ . In this model, the time dependence of the out-of-

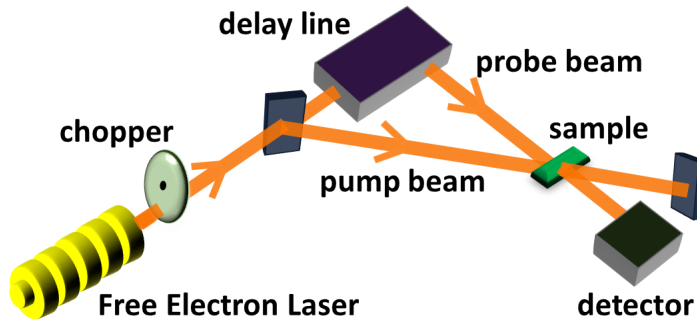


Figure 4.9: Degenerate pump-probe measurement scheme. The chopper is needed to perform the detection using a lock-in amplifier (not shown in the figure).



equilibrium energy of the electronic system is evaluated calculating the inelastic interactions with the pump beam and with the acoustic and optical phonon baths at an equilibrium lattice temperature  $T$ . Due to the optical pumping and the corresponding energy absorption from the incident radiation, the electronic system is considered to exhibit a global temperature higher than the local lattice temperature, strongly depending on the incident radiation intensity. Thanks to the presence of fast (sub-picosecond) elastic electron-electron interaction [86], at each time step of the model calculation, the electronic system is assumed to thermalize at a time-dependent electron temperature  $T_e$  calculated self-consistently. In this context, the electrons do populate excited states as effect of finite temperature and the obtained relaxations times are lower than in the case of empty-band calculations neglecting the effect of the electron distribution in the subbands. This is attributed to the thermal activation of non-radiative  $|1\rangle \rightarrow |0\rangle$  ISB transition via optical phonon emission, which involves electrons in the initial subband whose energy is high enough to guarantee the energy conservation.

Using the discussed features of the model, the electron distribution function in the two subbands  $|0\rangle$  and  $|1\rangle$  can thus be calculated as a function of the probe delay time, and subsequently used to simulate the differential transmission signal  $\Delta S/S$ . As stated before, the electron-phonon interaction in group-IV crystals is mediated only by the deformation potential and, if a dispersion-less optical phonon branch is assumed, it is possible to calculate the scattering rate  $W_{ij}^\mp(k_i)$  of an electron from subband  $|i\rangle$  to subband  $|j\rangle$  by phonon absorption ( $-$ ) or emission ( $+$ ). Following references [67, 80], the resulting expression is:

$$W_{ij}^\mp(k_i) = \Theta(k_f^2) \frac{m_d(D_{op}^{LL})^2}{2\hbar^2 \varrho \omega_{eff}} F_{ij} \left[ N(\omega_{eff}, T) + \frac{1}{2} \mp \frac{1}{2} \right] [1 - \rho(E_j, k_j, T_e, \mu)] \quad (4.10)$$

where  $k_{i,j}$  is the in-plane momentum<sup>(1)</sup>,  $\Theta$  the Heaviside step function,  $m_d = \sqrt{m_t(m_t + 2m_l)}/3 = 0.3m_e$  is the density-of-state (DOS) effective mass of Ge [66],  $\varrho$  the Ge mass density,  $N(\omega_{eff}, T)$  the phonon Bose distribution at lattice temperature  $T$ ,  $\rho(E_j, k_j, T_e, \mu)$  the electron Fermi distribution at temperature  $T_e$  and chemical potential  $\mu$ ,  $F_{ij}$  the overlap between initial and final wavefunctions. In the above expression,  $D_{op}^{LL}$  and  $\hbar\omega_{eff}$  are the effective deformation potentials and phonon energy, whose values are here considered to be  $3 \cdot 10^8$  eV/cm and 37 eV, respectively. Starting from the above scattering rate, the power loss related to absorption and emission of optical phonons can be easily calculated as

$$P_{OP} = \sum_{i,j} \hbar\omega_{eff} (W_{ij}^+ - W_{ij}^-) \quad (4.11)$$

As for the acoustic phonon scatterings, the power loss is expressed by

$$P_{AC} = \frac{3\pi k_B \hbar (D_{ac})^2 n_0}{64 \varrho k_j} \frac{4m_d}{\pi \hbar^2} F(T_e - T) \quad (4.12)$$

---

<sup>1</sup>The momentum vector  $\mathbf{k}_\perp$  introduced in section 2.1 is here used with the simpler notation  $\mathbf{k}$  for a better readability.

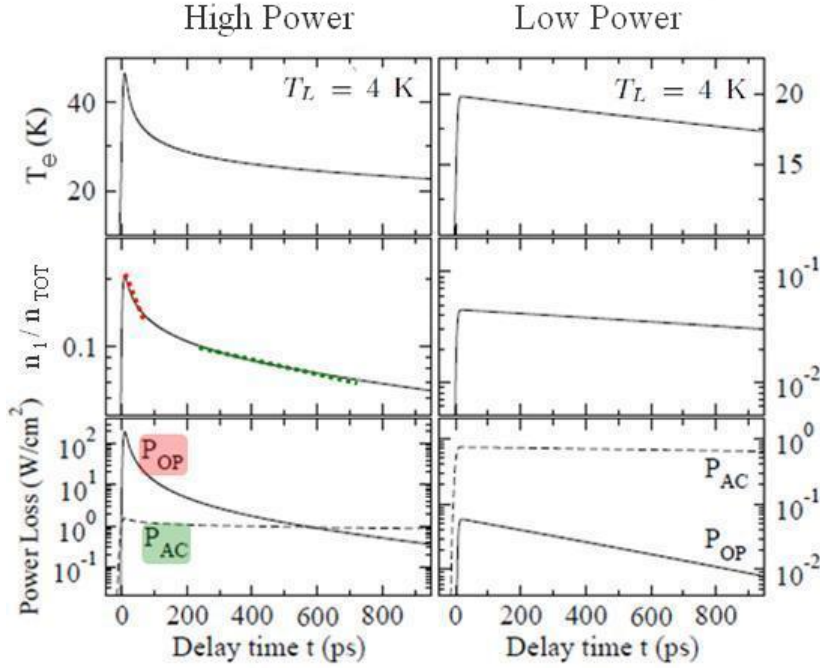


Figure 4.10: Simulations on sample S6 electron temperature  $T_e$ , population in the excited subband  $n_1/n_{TOT}$  and power loss via optical ( $P_{OP}$ ) and acoustic ( $P_{AC}$ ) phonon scattering as a function of pump-probe delay time for different pumping powers.

where  $D_{ac} = 2.5$  eV is the acoustic phonon deformation potential of Ge [87],  $n_0$  the population of subband  $|0\rangle$ , and

$$F = \frac{\sinh(x - x_e)}{\sinh x \sinh x_e} \left( \frac{x_e x}{x - x_e} \right), \quad x = \frac{\hbar\omega_{avg}}{2k_B T}, \quad x_e = \frac{\hbar\omega_{avg}}{2k_B T_e} \quad (4.13)$$

where  $\hbar\omega_{avg} = \sqrt{2}\hbar v_s k_j$  and  $v_s$  is the Ge sound velocity [67].

The obtained scattering rate expression has been used to perform calculations on sample S6 ( $E_{01} = 18$  meV), considering a constant lattice temperature of  $T = 4$  K and an electron temperature changing with the pumping power [67]. The result is reported in fig. 4.10, which shows the temporal evolution of the electron temperature  $T_e$ , the population in the excited subband  $|1\rangle$  and the system power loss due to optical ( $P_{OP}$ ) and acoustic ( $P_{AC}$ ) phonon scatterings. The simulations have been performed considering different levels of pumping powers.

For high pumping power (left columns in fig. 4.10) a significant fraction ( $\simeq 20\%$ ) of electrons are promoted to subband  $|1\rangle$ ,  $T_e > 40$  K and therefore the electrons can scatter to the ground subband  $|0\rangle$  via optical phonon interaction. This process results in a relatively fast relaxation characterized by an initial relaxation time of around 90 ps (red dots in the figure), until the acoustic contribution starts to dominate around  $t = 550$  ps (see the plot of power loss). The relaxation is now slower (green dots), on time scale around 2400 ps. These values are found to strongly depends on the pumping power employed and hence they may differ according to the experimental conditions. When instead the pumping power is low, the population of subband  $|1\rangle$  is almost negligible and the relaxation is dominated by the acoustic

term on the whole time interval, since  $E_{01}$  is lower than the optical phonon energy. In fact, the electron temperature and the power loss follow a single-exponential behavior in which the initial fast relaxation is absent.

The model developed here will be employed in the analysis of the electron dynamics of MQW samples back to equilibrium.

## 4.3 Pump-Probe/Time-Domain Spectroscopy

The optical characterization of the 3-level structure of the ACQW samples requires a spectroscopy technique able to probe the system in a wide range of energy while varying the pumping energy. The degenerate pump-probe spectroscopy discussed in the previous section is not suitable for this purpose and it needs be adapted accordingly. Optical investigation on ACQW samples has been therefore performed combining the pump-probe and time-domain spectroscopy (TDS) techniques, in order to investigate the possibility to achieve population inversion. In this configuration, the samples are pumped with the free-electron laser (FEL), while the TDS apparatus provides broadband THz probe pulses [88]. The employed setup has been built at the FELBE facility and its scheme is sketched in fig. 4.11. The generation of the THz probe signal is triggered by the ultrashort pulse of a synchronized Ti:sapphire (Ti:Sa) regenerative amplifier system lasing at 800 nm. The 10fs-short emitted pulse hits a ZnTe crystal, where the THz probe signal is generated by optical rectification. After the THz pulse propagation through the sample, detection takes place in an identical ZnTe crystal using the electro-optical sampling technique.

Generation and detection were performed in a nitrogen-purged environment, since many atmospheric constituents absorb the radiation in the THz range. The samples were placed in the same configuration described in sections 4.1 and 4.4.3, i.e. in a vacuum-pumped cryostat cooled with liquid He flow.

### 4.3.1 Setup description

The pump-probe/time-domain spectroscopy setup used in our experiments is sketched in fig. 4.11. The pump beam is provided by the free-electron laser FELBE at the Helmholtz-Zentrum Dresden-Rossendorf, whose characteristics are described in the previous section. The emission wavelength is tuned in the far-infrared range allowing the pumping of electrons from the ground level of our samples to the first or second excited levels. In order to pump the  $|0\rangle \rightarrow |1\rangle$  ISB transition, a wavelength of 50  $\mu\text{m}$  had been selected (photon energy of 25 meV), while the pumping of the  $|0\rangle \rightarrow |2\rangle$  ISB transition had been performed using a wavelength of 30  $\mu\text{m}$  (photon energy of 41 meV). The energy of the FEL pump pulses was adjusted with a set of attenuators in the 3-30 nJ range, corresponding to a power density at focus inside the sample of 8-80 kW/cm<sup>2</sup>, taking into account reflection and absorption losses due to all the elements inserted along the optical path shown in fig. 4.11. The use of the attenuators allowed to select the resulting pump power to values high enough to bring around 5% (0.5%) of the electrons populating the ground state into the first (second) excited state [67], avoiding steady-state sample heating at the same time. In order to properly study the electron dynamics, in fact, the samples need to be

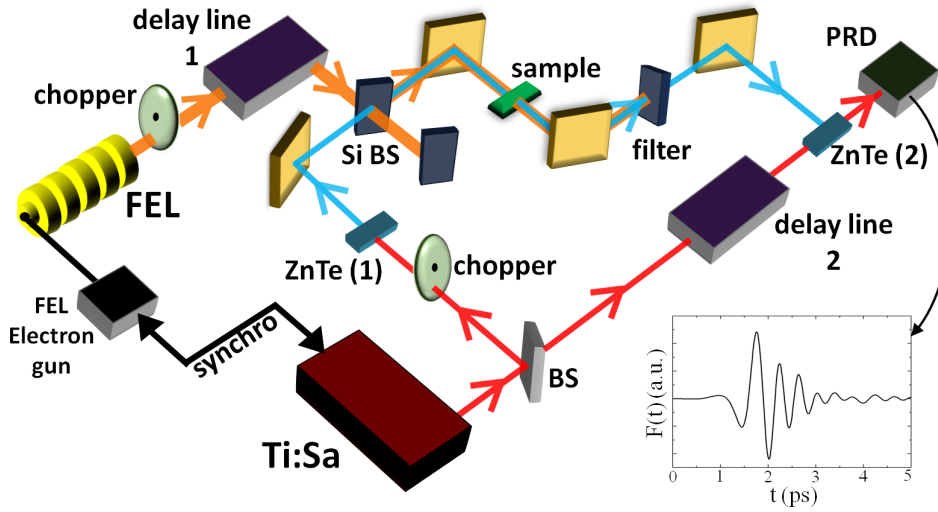


Figure 4.11: Pump-probe/TDS setup scheme. Orange line indicates the pump beam generated by the FEL, red line indicates the 800 nm beam generated by the Ti:Sa amplifier system and the light-blue line indicates the THz probe beam from the ZnTe generation crystal (number 1). The electro-optical effect takes place in a second ZnTe detection crystal (number 2), allowing the signal recording in a polarization-resolving detector (PRD). Two choppers are used for lock-in amplifier acquisitions.

kept at the steady selected temperatures of  $T = 37$  K and  $T = 97$  K.

The THz probe beam is generated via optical rectification in a ZnTe crystal hit by the ultrashort pulse emitted by a Ti:Sa regenerative amplifier system, lasing 10fs-short pulses at 800 nm with a repetition rate of 250 kHz synchronized with the master-clock driving the FEL electron gun. The generated probe pulses are quasi-single cycle oscillations of 300 fs, with a spectral content between 0.1 and 2.9 THz. However, diffraction effects inside the waveguide impose a low-frequency spectral cutoff at 0.7 THz (around 3 meV), where the free-space wavelength is 400  $\mu\text{m}$ , i.e. half of the waveguide thickness. Both the pump and probe beams are focused on the sample using flat and parabolic mirrors, and spatial overlap is guaranteed by a Si beam splitter (“Si BS” in fig. 4.11) that combines the FEL pump beam and the THz probe beam collinearly. While the beam splitter has a reflectivity of 42% at the pumping wavelength used here, resulting in a large reduction of the pump power delivered to the sample, the probe pulses can get through it without almost any attenuation. After the interaction with the sample, the pump beam is blocked by a low-pass filter which allows only the THz probe beam to get through.

The detection of the probe beam is performed in a second ZnTe crystal (identical to the one used for the THz generation) using the electro-optical sampling technique. To this aim, a second Ti:Sa beam obtained with the help a suitable beam splitter (“BS” in fig. 4.11) propagates inside the ZnTe detection crystal and it is afterwards directed to a polarization-resolving detector (“PRD” in fig. 4.11), which allows to retrieve the value of the electric field of the probe pulse.

The experimental setup features two delay lines for two different spectra acquisition: the first delay line (“delay line 1” in fig. 4.11) allows the tracking of the transmitted THz intensity as a function of the pump-probe delay  $t'$  with a long scan

range ( $-50 < t' < 400$  ps) similarly to what described in section 4.4.3, while the second one (“delay line 2” in fig. 4.11) allows for scanning the electric field time-domain traces  $F(t)$  of the THz probe pulses for a given pump-probe delay. The first kind of acquisition is used to extract the characteristic relaxation times of the out-of-equilibrium electron dynamics, while the time traces  $F(t)$  are Fourier transformed into frequency-resolved transmitted intensity  $H(\omega)$  for spectral analysis, in order to discriminate the free carrier losses and ISB transition bleaching effects. The time traces are cut at 10 ps after the leading edge, a value corresponding to a pump pulse duration that still enables a sufficient spectral resolution of 0.1 THz. Both the acquisitions are performed using a lock-in amplifier (not shown in the figures) at chopping frequencies of 33 Hz and 571 Hz for pump-probe and time-trace signals, respectively.

### 4.3.2 Optical rectification and electro-optical sampling

The fundamentals of these two non-linear processes could be easily understood starting with a classical approach, considering a non-centrosymmetric crystal hit by radiation. The charges can not oscillate following the radiation because of the presence of a preferred internal direction, and the polarization will not reverse together with the driving field. If the field oscillates periodically, the result is a steady dipole and the medium becomes polarized. When the field is applied by an ultra-short pulse, however, the mixing of different frequency components generates a fast changing polarization which results in the emission of THz radiation.

More in detail, the polarization vector  $\mathbf{P}$  of a non-linear material can be expressed in terms of a susceptibility  $\chi$  expanded in powers of the field  $\mathbf{F}$ :

$$\mathbf{P} = \varepsilon_0 \chi \mathbf{F} = \varepsilon_0 (\chi_1 + \chi_2 \mathbf{F} + \chi_3 \mathbf{F}^2 + \chi_4 \mathbf{F}^3 + \dots) \mathbf{F} \quad (4.14)$$

where  $\varepsilon_0$  is the vacuum electric permittivity. For a centrosymmetric crystal, all the even-order terms of the susceptibility  $\chi_{2n}$  are null due to the inversion symmetry of the crystal, and they generally exhibit only the common linear properties. In non-centrosymmetric crystals, instead, breaking the inversion symmetry allows the even-order components to be non-zero and, in particular, the second order component of the polarization vector is the term involved in optical rectification. Considering, for example, an electric field of two different components oscillating at  $\omega_1$  and  $\omega_2$ , the amplitude of the second order polarization vector  $P_2$  is:

$$\begin{aligned} P_2 &= \varepsilon_0 \chi_2 F_1 F_2 = \varepsilon_0 \chi_2 F_0^2 \cos(\omega_1 t) \cos(\omega_2 t) = \\ &= \varepsilon_0 \chi_2 \frac{F_0^2}{2} [\cos(\omega_1 - \omega_2)t + \cos(\omega_1 + \omega_2)t] \end{aligned} \quad (4.15)$$

where the second term is related to the second harmonic generation process and will be therefore omitted in the following. With only two components of the electric field, the polarization is thus proportional to an oscillating term with frequency  $(\omega_1 - \omega_2)$ . Extending to the case of a femtosecond near-infrared incident laser pulse, the lower frequency (THz) pulse generation is the result of the difference frequency mixing of all the frequencies within the bandwidth  $\Delta\omega$  of the laser pulse. The profile of the

radiated THz field  $F_{rad}$  follows directly from Maxwell equations:

$$\nabla^2 F_{rad} - \frac{1}{c^2} \frac{\partial^2}{\partial t^2} F_{rad} = \frac{1}{\varepsilon_0 c^2} \frac{\partial^2}{\partial t^2} P_2 \quad (4.16)$$

At fixed ultrashort pulse parameters, the generated THz pulse intensity and bandwidth are directly related to the crystal geometrical dimensions. Intense pulses are generated in thicker crystals, but increasing the thickness has also the effect of reducing the bandwidth because of phase mismatching and internal absorption. For the purpose of the present work, this trade-off led to the employment of ZnTe crystals able to emit THz pulses with spectral content between 0.1 and 2.9 THz. However, as said above, diffraction inside the sample impose spectral cutoff around 0.7 THz.

After the interaction with the sample, the THz probe pulse is sent to an identical ZnTe crystal for detection, where electro-optical sampling takes place. Here, exploiting the non-linear properties of the material, detection can be performed in a sort of reverse optical rectification, as it is described by the same term  $P_2$ . In fact, a THz pulse hitting the ZnTe crystal generates a birefringence therein, known as Pockels effect. To understand this effect we start considering the case without any applied electric field. In this situation, the spatial dispersion of the crystal refractive index  $\eta = \sqrt{\varepsilon_r}$  (which is directly related to the susceptibility  $\chi$  through common relations) is described by a 3-dimensional ellipsoid [89]:

$$\frac{x^2}{\eta_x^2} + \frac{y^2}{\eta_y^2} + \frac{z^2}{\eta_z^2} = 1 \quad (4.17)$$

where  $\eta_{x,y,z} = \eta$  in an isolated ZnTe crystal and the axes  $x$ ,  $y$  and  $z$  are the principal dielectric axes, i.e. the axes along which  $\mathbf{P}$  and  $\mathbf{F}$  are collinear. In the present case of ZnTe crystals, these axes are oriented with  $x$  and  $y$  lying on the plane parallel to the (100) surface. In the presence of an external electric field, the ellipsoid undergoes a change and can be expressed in the following general form [89]:

$$\left(\frac{1}{\eta^2}\right)_1 x^2 + \left(\frac{1}{\eta^2}\right)_2 y^2 + \left(\frac{1}{\eta^2}\right)_3 z^2 + 2\left(\frac{1}{\eta^2}\right)_4 yz + 2\left(\frac{1}{\eta^2}\right)_5 xz + 2\left(\frac{1}{\eta^2}\right)_6 xy = 1 \quad (4.18)$$

The first three terms are of the same form as the terms in equation 4.17, while the additional terms generate a rotation of the refractive index ellipsoid. In absence of external electric field, the first three terms are exactly the same as in equation 4.17 and the additional terms are null. In the general case of an applied electric field, all the six components experience a change proportional to the external electric field components:

$$\Delta \left(\frac{1}{\eta^2}\right)_i = \sum_{j=1}^3 r_{ij} F_j \quad (4.19)$$

where  $r_{ij}$  denotes the components of the so-called *electro-optic tensor*. In centrosymmetric crystals all the elements of the tensor are null, since the second order susceptibility  $\chi_2 = 0$ . For a non-centrosymmetric cubic crystal like the ZnTe, instead, every  $r_{ij}$  component is zero with the exception of  $r_{41}$ ,  $r_{52}$  and  $r_{63}$ , which are all of the

same value proportional to the susceptibility  $\chi_2$  and therefore directly related to the second order polarization vector  $P_2$ . Following reference [89], it is useful to redefine the principal axes of the deformed ellipsoid as a rotation around the  $z$  axis, which stays unchanged. This change of coordinate system assures that the  $z$  and  $x$  axes lie in the surface of a (110) ZnTe crystal, which is the common orientation used in this kind of crystals for THz generation and detection. In this case, if the applied electric field is along the  $z$  axis ( $F_3=F_z=F$ ), hence parallel to the crystal surface, the deformed ellipsoid is of the following form:

$$\frac{(x')^2}{\eta^2} + \frac{(y')^2}{\eta^2} + \frac{z^2}{\eta^2} + 2r_{41}Fxy = 1 \quad (4.20)$$

where  $x'$ ,  $y'$  and  $z'=z$  are the new axes.

In the present experiment, the rotation of the refractive index ellipsoid is induced by the THz probe pulse after the interaction with the sample. This change leads to a rotation of the optical polarization of a second beam of the ultrashort Ti:Sa pulses, previously deviated by a beam splitter towards the detection crystal (see fig. 4.11). The Ti:Sa beam polarization change is proportional to the intensity of the THz electric field as seen above, and the direction of rotation is determined by the sign of the field, making this technique sensitive not only to the magnitude of the THz field but also to its phase. The resulting elliptical polarized beam is sent to the polarization-resolving detector, where it propagates through a  $\lambda/4$  wave-plate and through a Wollaston prism right after. The split components of the polarized field are then analyzed by two photodiodes producing a difference in voltage proportional to the THz field, which can thus be recorded. Schematic representation of the described steps is shown in fig. 4.12.

With the help of a delay line (“delay line 2” in fig. 4.11), the whole electric field profile can be sampled at different times  $t$ , as shown in the example in fig. 4.13. The Fourier transform of such time trace signal shows the power spectrum  $H(\omega)$  of the THz pulse in the frequency domain and it will be used later in this chapter. Moving the mirror of the pump-probe delay line (“delay line 1” in fig. 4.11) while keeping the time-domain delay line fixed allows the tracking over time  $t'$  of the value of the electric field recorded at that specific position of the time-domain delay line, revealing the sample absorption changes caused by the effect of the delay between FEL pump and THz probe. The analysis of this type of signals is the topic of the next section.

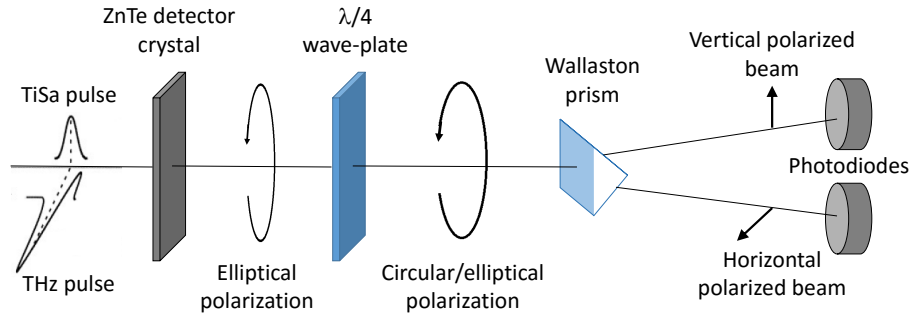


Figure 4.12: Detection process scheme of the probe beam coming out of the ZnTe detection crystal.

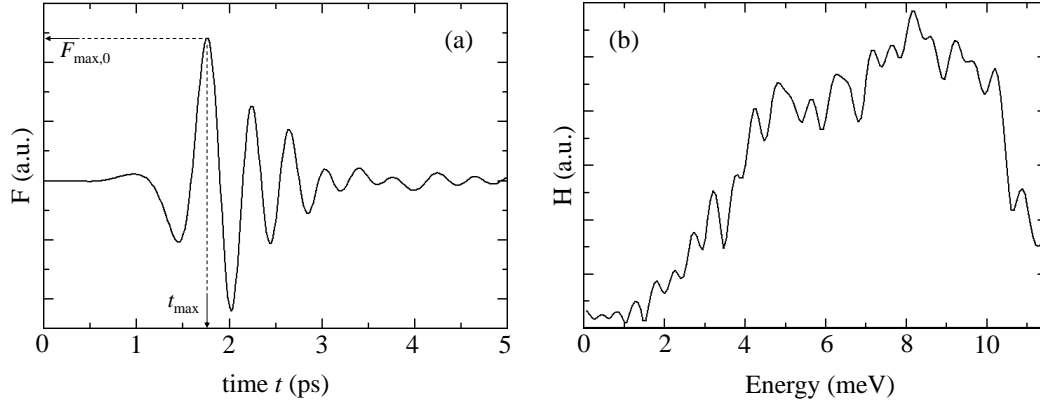


Figure 4.13: Time trace profile (a) and spectral content (b) of the detected THz probe pulse as a function of time  $t$  of the time-domain delay line.

### 4.3.3 ACQW relaxation times estimation

The crucial condition to realize a Si-based emitter consists in establishing a population inversion between two excited levels, which can only be possible if the relaxation time  $\tau_2$  of the upper excited level  $|2\rangle$  is high while relaxation time  $\tau_1 = \tau_{10}$  of the lower excited level  $|1\rangle$  towards ground level  $|0\rangle$  is very low. The quantum design of our samples, in fact, exploits the asymmetry of the ACQW structure to achieve a long life-time  $\tau_2$  of the upper excited state, which eventually allows to create a non-equilibrium carrier distribution suitable for light emission. In order to obtain such distribution, the non-equilibrium population of the 3-level system is generated by optical pumping with the FEL pulses and it is tracked over time to retrieve the sample transmittance as a function of the pump-probe delay time  $t'$ . Experimentally, the pump-probe data are obtained in two steps:

- scanning the time-domain delay line to detect the delay position  $t_{\max}$  at which the THz electric field is at maximum value, and keeping fixed the delay line at this specific position,
- scanning the pump-probe delay line to track the value of the electric field over the delay time  $t'$ .

These steps summarize the following procedure: with the pump beam switched off, the THz pulse profile is sampled over the time  $t$  set by the time-domain delay time, and the time trace of the electric field  $F(t)$  is obtained. The time-domain delay line is then kept fixed at the position corresponding to the delay time  $t_{\max}$  at which the maximum of the electric field  $F(t_{\max}) = F_{\max,0}$  is recorded (see fig. 4.13). Switching on the FEL pump beam, the pump-probe delay line is scanned and the value of  $F_{\max}(t')$  is tracked over the delay time  $t'$  set by the pump-probe delay line (time-domain delay line is kept fixed). In this way, the relaxation back to equilibrium after the pumping is monitored by measuring the return of the THz electric field  $F_{\max}(t')$  to its equilibrium value  $F_{\max,0}$  measured before the pump pulse arrived. With the use of a lock-in amplifier, the monitored quantity is  $\Delta F_{\max}(t') = F_{\max}(t') - F_{\max,0}$  which can be fitted to the standard exponential decay equation:

$$\Delta F_{\max}(t') = \Delta F_{\max}(0) e^{-\frac{t'}{\tau_R}} \quad (4.21)$$



where  $\Delta F_{max}(0)$  is the value of the electric field at pump-probe coincidence ( $t' = 0$ ) relative to its equilibrium value  $F_{max,0}$ . The free parameter of the fitting process is  $\tau_R$ , which represents the relaxation back to equilibrium of the system excited by pumping. Physically, with the described experiment one probes the free carrier absorption change returning to its equilibrium value, spectrally integrated between 0.7 and 2.9 THz (around 3-11.5 meV). Even if the electric field change  $\Delta F_{max}(t')$  is distinct from the optical transmission, both quantities are mainly determined by the electron dynamics and return back to equilibrium with the same characteristic time  $\tau_R$ . The free carrier absorption should not be observable in a pure TM configuration, since it takes place in the plane perpendicular to the sample growth direction  $z$  where the carriers should not be mobile. However, this condition is strictly true only at the metal/semiconductor interface, but the total thickness of the QW stack extends away from the interface to inner regions of the sample where the electric field of the propagating mode is not exactly parallel to the growth direction  $z$ . Therefore, the free carrier absorption is possible in our samples, although strongly reduced compared to the case of TE polarization, by a factor we estimated to be around 25. This process takes place in all the occupied subbands, which can be only levels  $|0\rangle$  and the  $|1\rangle$  when pumping the  $|0\rangle \rightarrow |1\rangle$  transition, or also level  $|2\rangle$  when pumping the  $|0\rangle \rightarrow |2\rangle$  transition.

In order to properly interpret the experimental results, the system relaxation dynamics back to the equilibrium after optical pulsed excitation has been studied in the framework of an out-of-equilibrium model similar to the one described for degenerate pump-probe experiments. The delay-time-dependent electron temperatures  $T_{e,0}$ ,  $T_{e,1}$  and  $T_{e,2}$  in the three subbands are separately defined and the entire electron system is allowed to relax energy towards the lattice by mean of optical phonon scattering, considered as a thermal bath at temperature  $T$  [80, 90]. For a more realistic description compared to the discussed model in section 4.2, here we take into account both the zone-center phonon at  $E_{ph,\Gamma} = 37$  meV and the [111] zone-boundary one at  $E_{ph,\Lambda} = 24$  meV. The model is then used to calculate the subband populations  $n_i$  after absorption of the pump pulse and their evolution as a function of pump-probe delay  $t'$ . The differential transmission change relative to pump-off conditions  $\Delta S/S = (S(t') - S_{off})/S_{off}$  is also determined numerically from the electron population and total kinetic energy calculated for each subband. It is found that, when pumping above the  $|0\rangle \rightarrow |2\rangle$  ISB transition, a single relaxation time scale  $\tau_R$  approximately governs both the transmittance change  $\Delta S/S$  and the population dynamics  $\Delta n_i/n_{tot} = (n_i(t') - n_{i,off})/n_{tot}$  in the three subbands. When pumping at the  $|0\rangle \rightarrow |1\rangle$  transition energy, instead, a more complicated dynamics with multi-exponential behavior results from the model.

## 4.4 Optical characterization of MQW samples

The discussed spectroscopy techniques have been employed to study the optical properties of the grown samples, in order to highlight the main features that can be exploited in the realization of a Si-compatible THz emitter. The first step of the optical investigation consists in verifying the outcome of the growth process, trying to link the structural parameters to the optical properties of the system. To

this aim, a series of 7 modulation-doped MQW samples (S1-S7) has been realized and characterized to extract the basic properties of a QW structure, as the ISB transitions rate and energy. The periodic repetition of single elements ensures that the optical properties of the system are referred to the single QW structure, with measurable effects determined by the sum of each QW contribution. Therefore, the number  $N_W$  of periods works as a multiplying factor amplifying the optical features of a single QW.

#### 4.4.1 Absorption energies and carrier densities

The optical characterization on MQW samples has been performed with the FTIR technique, in order to extract the ISB transition energies and verify the correspondence with theoretical predictions. Transmission spectra have been acquired in both TE and TM polarizations and the dichroic signal  $T(E)$  calculated to highlight only the ISB contributions. Starting from  $T(E)$  it is possible to obtain the bi-dimensional absorption coefficient from the relation

$$\alpha_{2D}(E) = -\frac{\ln[T(E)] \cos(\theta)}{CMN_W \sin^2(\theta)} \quad (4.22)$$

as discussed in section 4.1.3. The absorption coefficient functions of the first 5 samples are reported in fig. 4.14. To obtain a more quantitative characterization, the spectra have been analyzed with a fitting procedure using a gaussian curve, which returns in output the transition energy, the linewidth  $\Gamma$  and the peak area  $A$ .

The intrinsic broadening of the absorption peaks is expected to have a lorentzian lineshape while extrinsic contributions give a gaussian broadening. If both effect are present, the absorption peak should have a Voigt lineshape. In our experimental data the superimposed oscillations introduced by the employed polarizer prevent an unambiguous lineshape identification. The result of the the fit procedure of samples S6 and S4 employing lorentzian and Gaussian curves is shown in fig. 4.15 as examples. Although the gaussian curve reproduces the experimental data with a smaller

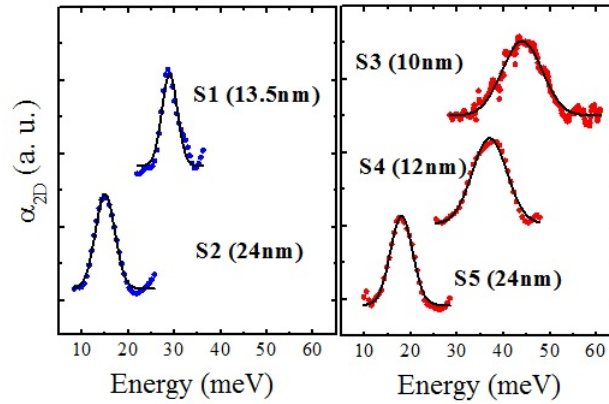


Figure 4.14: Bi-dimensional absorption coefficient for samples with different well width  $d_w$  with 10 nm spacer layers (left panel) or without spacer layers (right panel).

For a better visualization each curve has been normalized independently.

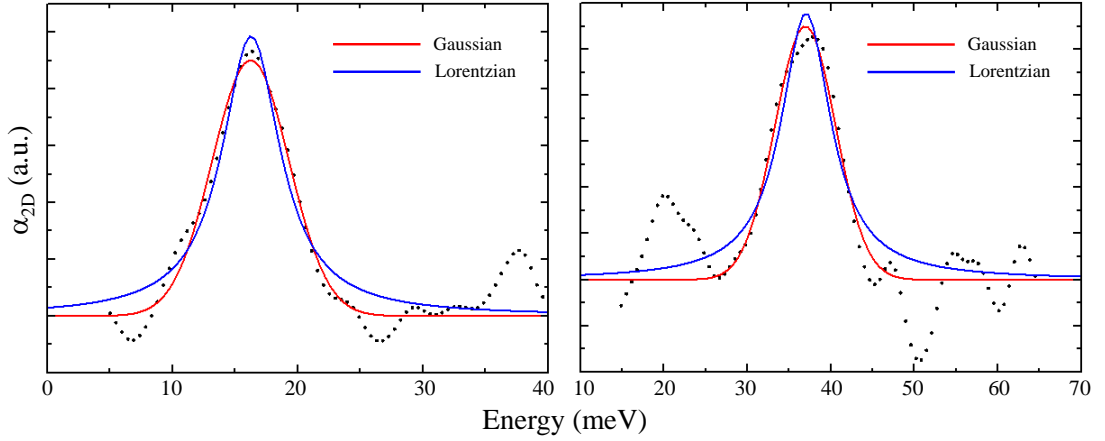


Figure 4.15: Fit results for sample S6 (left panel) and S4 (right panel) at 8 K using both gaussian and lorentzian curves.

value of the reduced  $\chi^2$ , the differences between the two curves are smaller than the oscillations introduced by the polarizer. In any case the important parameters (e.g. linewidth, peak position, peak area) can be retrieved correctly from our data, resulting quite independent (within 10%) from the chosen fitting curve.

Considering the output parameters summarized in table 4.1, all the observed ISB transitions are characterized by energies in the THz band, since they are between around 15 meV and 40 meV, fully achieving the objectives set for this work. Furthermore, the values obtained for the bi-dimensional absorption coefficients  $\alpha_{2D}$  reported in table 4.1 have been found to be suited for implementation in optical devices, although still lower than the standard values reported for III-V materials [3].

Sample	$d_w$ (nm)	$d_b$ (nm)	$\alpha_{2D}(E_{01})$ ( $10^{-3}$ )	$\Gamma$ (meV)	$E_{01}^{th}$ (meV)	$E_{01}$ (meV)	$n_{2D}$ ( $10^{11}\text{cm}^{-2}$ )	$\tilde{E}_{01}$ (meV)
S1	13.5	30	1.51	2.1	28.3	28.8	0.7	29.0
S2	24	30	2.08	2.2	10.4	14.9	0.9	11.9
S3	10	30	4.75	5.0	41.7	46.0	3.4	44.5
S4	12	25	0.78	4.3	33.7	37.0	1.2	34.9
S5	24	30	3.33	3.0	9.8	16.3	1.5	12.3
S6	24	30	2.22	3.4	9.4	18.0	2.0	12.7
S7	12	30	3.43	3.7	32.4	39.7	2.2	34.6

Table 4.1: Samples structural and optical properties: Ge QW width  $d_w$ , SiGe barrier width  $d_b$ , peak value of the bi-dimensional absorption coefficient  $\alpha_{2D}(E_{01})$ , linewidth  $\Gamma$ , theoretical ISB transition energy  $E_{01}^{th}$ , experimental ISB transition energy  $E_{01}$ , well charge density  $n_{2D}$ , theoretical ISB transition energy  $\tilde{E}_{01}$  after the depolarization shift correction is applied.

The bi-dimensional charge densities  $n_{2D}$  listed in the table have been calculated directly from the peak area following the relation [3]:

$$\int \alpha_{2D}(E) dE = n_{2D} \frac{\pi e^2 \hbar}{2\varepsilon_0 \eta c m^*} \quad (4.23)$$

The obtained densities for these modulation-doped samples are found to be one order of magnitude lower than the expected values, calculated as  $n_{2D}^{th} = n_{3D} \cdot d_w$  assuming a complete charge transfer from the doped barriers to the wells of width  $d_w$ . This discrepancy points out a partial charge transfer due to the small difference between the donor levels in the barriers and the lowest subband in the wells. Such effect is indeed stronger for thin wells, where the lowest subband has a higher energy thus closer to the barrier donor levels, and becomes weaker increasing the wells width.

The data acquired via FTIR spectroscopy and the corresponding fit results have been compared with the theoretical calculations to test both the robustness of the employed models and the quality of the grown samples. The energies of the levels inside the wells can be evaluated using the graphic procedure for the finite potential well described in section 2.1, in which the resulting energies depend not only from the well width  $d_w$  but also from the well depth  $V_0$ . This parameter is the band offset determined by the difference between the conduction bands minima of the Ge wells and the SiGe barriers at the L point, and it is evaluated to be around 100 meV. This method has been used to design the samples having a wide range of absorption energies. However, it does not take into accounts several aspects, as the charge density in the barriers due to the ionized donor atoms used for the modulation doping of the samples, and it is therefore too simple to be used in the analysis of the experimental data.

A more thorough approach consists in multi-band self-consistent calculations in the  $\mathbf{k} \cdot \mathbf{p}$  envelope function approximation [65], in which the electronic states are calculated in the Schrödinger-Poisson iterative scheme, taking into account ionized

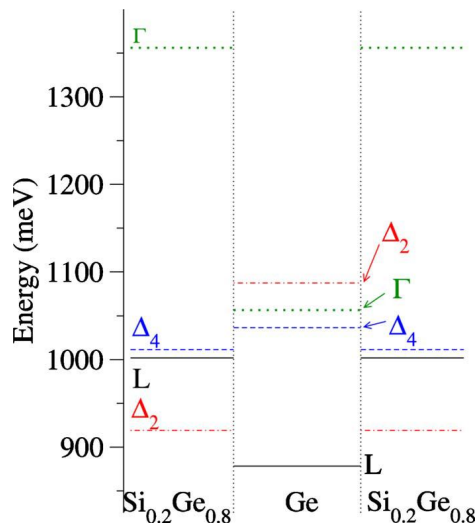


Figure 4.16: Calculated conduction band edge profiles of L,  $\Delta_2$ ,  $\Delta_4$  and  $\Gamma$  valleys for a Ge/Si<sub>0.2</sub>Ge<sub>0.8</sub> heterostructure. The energy scale is considered to start at the top of the valence band.

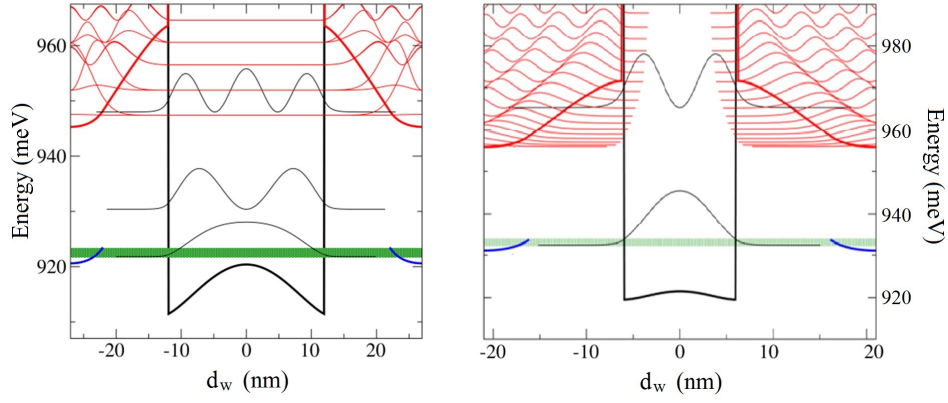


Figure 4.17: Calculations on samples S2 (left) and S1 (right) structure: conduction band profile and squared modulus of the level wavefunctions at L point (black lines) and  $\Delta$  point (red lines). Calculated Fermi level at low temperature (green line) and donor levels in the doped region of the barrier (blue lines).

impurities and contribution to the Hartree potential from electrons at the L,  $\Delta$  and  $\Gamma$  valleys. Exchange-correlation effects are included in the local-density approximation only for electrons at L point, since at low temperature the free electron density is mostly due to the confined carriers at L [65,91]. The Fermi level  $E_F$  is evaluated as a function of temperature taking into account also the occupation of the impurity levels in the barriers. As an example, the calculation on a Ge/Si<sub>0.2</sub>Ge<sub>0.8</sub> heterostructure is performed and the obtained L,  $\Delta_2$ ,  $\Delta_4$  and  $\Gamma$  profile of the conduction band edges are shown in fig. 4.16.

Calculations shows that the band offset between the L edges is slightly higher than 100 meV but the energy difference between the  $\Delta_2$  minima in the barriers and the L minima in the well is only 40 meV. This means that donor levels right under the SiGe conduction band edge at  $\Delta$  are very close to the ground level of the Ge well at L point. In other words the electronic density in the well due to the charge transfer from the barriers is limited by the small energy difference between the  $\Delta_2$  minimum in the barrier and the L minimum in the well. This is even more clear looking at fig. 4.17, in which the calculation results for samples S2 and S1 are reported. The plots show not only the band alignment and the calculated wavefunctions, but also the donor levels in the barriers which, far from the interface, are below the Fermi level. As a consequence, a very small fraction of the donor states is ionized and this explains why the experimental densities  $n_{2D}$  in the investigated samples are found to be so much lower than the values expected implying a complete charge transfer. Moreover, the spatial separation in modulation doped structures is responsible for the band bending of the band edge profiles, as apparent in fig. 4.17. In particular, the bending of the well profile at L point slightly reduces the energy separation between the confined subbands, as previously introduced in section 2.5.

The ISB transition energies obtained from the model are reported in table 4.1 as  $E_{01}^{th}$  next to the experimental values  $E_{01}$ . The comparison between theoretical predictions and experimental data shows how the agreement is not good for every sample, because of a non-negligible contribution of the depolarization shift. Recalling what discussed in section 2.5, the transition energy that takes into account the

depolarization shift correction is

$$\tilde{E}_{01} = E_{01}^{th} (1 + \phi)^{1/2} \quad (4.24)$$

where

$$\phi = \frac{2e^2 \bar{d}}{\varepsilon_r \varepsilon_0 E_{01}^{th}} n_{2D} \quad (4.25)$$

The depolarization shift is therefore a relevant contribution to the transition energy for wide wells and high carrier densities  $n_{2D}$ , e.g. the case of sample S6. The revised values  $\tilde{E}_{01}$  for the transition energies are reported in table 4.1, showing how the applied correction improves the comparison for every sample. As previously discussed, any other effect that leads in principle to an energy shift has not been considered here, as they are of smaller intensity compared to the depolarization shift and they partially compensate each other [3].

The analysis of the FTIR spectra allowed also to study the temperature dependence of the ISB transition energies. The behavior was found to be different for wide and narrow QWs, as reported in fig. 4.18 for samples S2 and S1. In fact, in the absorption spectra of samples featuring wide wells it is possible to observe a blue shift of the ISB transition peak with increasing temperature, which is instead absent in the spectra acquired from narrow well samples. This effect is attributed to the small energy separation of the subbands in wide well, which facilitates the promotion of a portion of the electron density of the ground subband  $|0\rangle$  into the first excited subband  $|1\rangle$ . At low temperature, all the electrons populate the fundamental level of sample S2 and only the first ISB transition  $|0\rangle \rightarrow |1\rangle$  at  $E_{01} \simeq 16$  meV is induced by the incident radiation. Increasing the temperature, however, has the effect of partially populate subband  $|1\rangle$  and a second contribution from the  $|1\rangle \rightarrow |2\rangle$  transition around 20 meV is added to the principal peak in the absorption spectrum, until it becomes dominant at higher temperatures. The absorption peaks observed at each temperature are therefore obtained as the sum of two contributions weighted according to the actual population of the starting level [68].

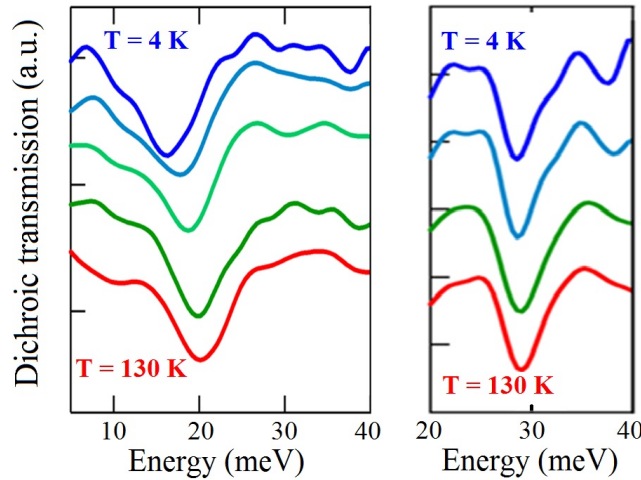


Figure 4.18: ISB transition energy dependence on increasing temperature for samples S2 (left) and S1 (right), featuring well width  $d_w$  of 24 and 13.5 nm.

### 4.4.2 Linewidth broadening

One of the most important characteristic of an ISB transition is its spectral linewidth  $\Gamma$ . This aspect is of crucial importance for the realization of optical devices since it heavily influences their performances. Furthermore, a narrow linewidth is a fingerprint of the structural quality of the realized heterostructures, because it is the expression not only of the intrinsic interaction processes (e.g. electron-phonon scattering), but also of the scattering channels related to the sample structural quality like defects, impurities, or interface roughness, for example.

It is important to notice that achieving a narrow linewidth is of great relevance also for experiments and applications making use of the coherence between quantum mechanical energy states [92,93], since this condition is associated with a long coherence time of the QW states. In addition to applications, the analysis of the physical mechanisms behind the line broadening is also relevant from a more fundamental perspective, being closely related to open issues in the physics of low dimensional semiconductors as intra- and inter-subband relaxation, transport properties, and many-body effects [94,95].

Despite the fact that the theoretical framework has been originally developed to describe ISB transitions in n-type Si inversion layers [72,96,97], the absorption linewidth in QW systems and its dependence on the various scattering processes have been investigated mainly in III-V materials [95]. Experimental studies on the absorption lineshape of systems based on group-IV semiconductors have been performed insofar only on p-type low-Ge content structures, where the linewidth broadening is dominated by the large non-parabolicity of the valence bands [98,99]. On the contrary, this broadening effect is negligible in n-type Ge/SiGe heterostructures, where the single parabolic conduction band minimum originates almost parallel subbands with constant  $E_{01}$  transition energy. This situation allows the study of the intrinsic electron scattering mechanisms that contribute to the linewidth broadening, and eventually to obtain much narrower linewidths than those reported in p-type Si/SiGe heterostructure materials.

#### Theoretical framework

The single-well ISB linewidth (whose values are reported in table 4.1) have been modeled in collaboration with “Università di Pisa” to address the relative importance of the different scattering sources contributing to the lineshape. To this aim, the theoretical linewidth  $\Gamma^{th}(E)$  of the first ISB transition as a function of electron energy  $E$  has been evaluated starting from the theory developed by Ando [72,96,97] and expanded by Unuma [95]. The calculation takes into account scattering processes originating from the presence of interface roughness (IFR), ionized impurities (II), acoustic (AP) and optical (OP) phonons, and alloy disorder (AD):

$$\Gamma^{th}(E) = \Gamma^{IFR}(E) + \Gamma^{II}(E) + \Gamma^{AP}(E) + \Gamma^{OP}(E) + \Gamma^{AD}(E) \quad (4.26)$$

The electron-electron scattering has been here neglected, since it generates a negligible contribution to the linewidth broadening at the investigated carrier densities [95]. In addition, for each perturbing potential  $H^i$ , every contribution to the

linewidth  $\Gamma^i(E)$  has been evaluated considering both intra- and inter-subband scattering events, given by [80]:

$$\begin{aligned}\Gamma_{intra}^i(E) &= 2\pi \sum_{k'} \{ |\langle 0\mathbf{k}' | H^i | 0\mathbf{k} \rangle - \langle 1\mathbf{k}' | H^i | 1\mathbf{k} \rangle|^2 \} \\ \Gamma_{inter}^i(E) &= 2\pi \sum_{k'} \{ |\langle 0\mathbf{k}' | H^i | 1\mathbf{k} \rangle|^2 \}\end{aligned}\quad (4.27)$$

where a  $\delta$  function ensuring the energy conservation is implied. In the above equations  $|j\mathbf{k}\rangle$  are the electronic states with subband index  $j$  and momentum  $\mathbf{k}$  in the plane perpendicular to the growth axis. The brace brackets  $\{\dots\}$  indicate a statistical average over the spatial distribution of scattering centers.

The IFR intra- and inter-subband contribution to the linewidth broadening have been evaluated starting from the root mean square roughness  $\tilde{\Delta}$  and correlation length  $\tilde{\Lambda}$  estimated on the basis of transmission electron microscopy measurements performed on the Ge/SiGe interfaces of similar CVD-grown samples [65, 68]. The expression of these contributions is as follows:

$$\begin{aligned}\Gamma_{intra}^{IFR}(E) &= \frac{m_d \tilde{\Delta}^2 \tilde{\Lambda}^2}{\hbar^2} \int_0^\pi d\theta \left( \frac{F_{00}}{S(q)} - F_{11} \right)^2 \exp \left( \frac{-q^2 \tilde{\Lambda}^2}{4} \right) \\ \Gamma_{inter}^{IFR}(E) &= \frac{m_d \tilde{\Delta}^2 \tilde{\Lambda}^2}{\hbar^2} F_{01}^2 \int_0^\pi d\theta \exp \left( \frac{-\bar{q}^2 \tilde{\Lambda}^2}{4} \right)\end{aligned}\quad (4.28)$$

where  $\tilde{\Delta} = 3.5 \text{ \AA}$ ,  $\tilde{\Lambda} = 70 \text{ \AA}$ ,  $m_d = 0.3m_e$  is the DOS effective mass of Ge,  $q$  and  $\bar{q}$  are the modulus of the in-plane momentum vector exchanged in the intra- and inter-subband scattering, respectively. Their dependence on the scattering angle  $\theta$  is given by:

$$\begin{aligned}q^2 &= 2k^2(1 - \cos \theta) \\ \bar{q}^2 &= 2k^2 + \frac{2m_d E_{01}}{\hbar^2} - 2k \sqrt{k^2 + \frac{2m_d E_{01}}{\hbar^2}} \cos \theta\end{aligned}\quad (4.29)$$

The terms  $F_{mn}$ , with  $m, n=0, 1$ , are given by  $F_{mn} = V_0 \psi_m(-d_w/2) \psi_n(-d_w/2)$ , where  $V_0$  is the height of the QW confinement potential and  $\psi_{m,n}(-d_w/2)$  are the values of the levels  $|0\rangle$  and  $|1\rangle$  envelope functions at the well/barrier interface. In equation 4.28 and hereafter, the screening effect has been taken into account inserting the function  $S(q)$ , whose detailed expression could be found in reference [95, 97]. This static correction is needed only for intra-subband scattering processes, while the dynamic screening is expressed by the depolarization shift in inter-subband transitions.

As for the II contributions to the broadening, for a given ionized impurity concentration profile  $N(Z)$  they are of the following form:

$$\begin{aligned}\Gamma_{intra}^{II}(E) &= \frac{m_d e^4}{4\pi \epsilon_0^2 \kappa_{avg}^2 \hbar^2} \int dZ N(Z) \int_0^\pi d\theta \left[ \frac{1}{q} \int dz \left( \frac{\psi_0^2(z)}{S(q)} - \psi_1^2(z) \right) e^{-q|z-Z|} \right]^2 \\ \Gamma_{inter}^{II}(E) &= \frac{m_d e^4}{4\pi \epsilon_0^2 \kappa_{avg}^2 \hbar^2} \int dZ N(Z) \int_0^\pi d\theta \left[ \frac{1}{q} \int dz \psi_0(z) \psi_1(z) e^{-\bar{q}|z-Z|} \right]^2\end{aligned}\quad (4.30)$$



where  $\kappa_{avg} = \frac{1}{2}(\varepsilon_r^{Ge} + \varepsilon_r^{SiGe})$  is the average dielectric constant of the well+barrier material.

Concerning the phonon scattering, the electron-phonon coupling is mediated only by the deformation potential, which is thus the only contribution to  $H^{AP}$  and  $H^{OP}$ . As already discussed, this result directly follows from the non-polar nature of the SiGe alloy contrary to what happens in III-V material systems, in which the long-range Fröhlich interaction is also present and generates a sharp scattering resonance at the phonon energy. In the evaluation of the linewidth broadening caused by phonon scattering, acoustic and optical phonon branches have been assumed to be respectively linear and flat, and referred to a 3D phonon bath. Under these approximations the acoustic phonon contributions are:

$$\begin{aligned}\Gamma_{intra}^{AP}(E) &= \frac{m_d k_B T D_{ac}^2}{\pi \hbar^2 C_{11}} \int_0^\pi d\theta \int dz \left[ \frac{\psi_0^2(z)}{S(q)} - \psi_1^2(z) \right]^2 \\ \Gamma_{inter}^{AP}(E) &= \frac{m_d k_B T D_{ac}^2}{\pi \hbar^2 C_{11}} \int_0^\pi d\theta \int dz [\psi_0(z) \psi_1(z)]^2\end{aligned}\tag{4.31}$$

where  $T$  is the temperature,  $D_{ac} = 2.5$  eV [100] is the effective deformation potential for acoustic phonons in Ge,  $C_{11} = 1.3 \cdot 10^{11}$  N/m<sup>2</sup> is the longitudinal elastic constant and  $k_B$  is the Boltzmann constant. Notice that  $\Gamma_{inter}^{AP}$  does not depend on the electron kinetic energy  $E$ , while  $\Gamma_{intra}^{AP}$  is only weakly dependent on  $E$  through the screening function  $S(q)$ .

The linewidth broadening due to interaction with the optical phonons has been calculated starting from the expressions derived in reference [99] and conveniently modified to obtain both intra- and inter-subband scattering events among L valleys in Ge:

$$\begin{aligned}\Gamma_{intra}^{OP}(E) &= \frac{m_d}{2\varrho d_w} \left\{ \frac{D_{op}^2}{\hbar\omega_{ph}} [\Theta(E - \hbar\omega_{ph})(N_q + 1) + N_q] \right. \\ &\quad \left. + \frac{3(D_{op}^{LL})^2}{\hbar\omega_{ph}^{LL}} [\Theta(E - \hbar\omega_{ph}^{LL})(N_q + 1) + N_q] \right\} \\ \Gamma_{inter}^{OP}(E) &= \frac{m_d}{2\varrho d_w} \left\{ \frac{D_{op}^2}{\hbar\omega_{ph}} [\Theta(E + E_{01} - \hbar\omega_{ph})(N_q + 1) + N_q] \right. \\ &\quad \left. + \frac{3(D_{op}^{LL})^2}{\hbar\omega_{ph}^{LL}} [\Theta(E + E_{01} - \hbar\omega_{ph}^{LL})(N_q + 1) + N_q] \right\}\end{aligned}\tag{4.32}$$

where  $\varrho$  is the Ge mass density and  $\Theta(E)$  is the Heaviside step function;  $D_{op} = 5.5 \cdot 10^8$  eV/cm and  $D_{op}^{LL} = 3 \cdot 10^8$  eV/cm are the Ge effective deformation potentials associated with intra- and inter-valley scatterings, respectively;  $\hbar\omega_{ph} = 27.6$  meV and  $\hbar\omega_{ph}^{LL} = 37$  meV are the corresponding effective optical phonon energies [100].

Finally, the contribution of the alloy disorder scattering has been evaluated. This scattering mechanism is particularly significant for small well width, where the wavefunction penetration in the Si<sub>1-x</sub>Ge<sub>x</sub> barriers is larger. The obtained expressions

are:

$$\begin{aligned}\Gamma_{intra}^{AD} &= \frac{m_d a^3 (\delta E_c)^2 x(1-x)}{\pi \hbar^2} \int_0^\pi d\theta \int_{alloy} dz \left[ \frac{\psi_0^2(z)}{S(q)} - \psi_1^2(z) \right]^2 \\ \Gamma_{inter}^{AD} &= \frac{m_d a^3 (\delta E_c)^2 x(1-x)}{\pi \hbar^2} \int_0^\pi d\theta \int_{alloy} dz [\psi_0(z)\psi_1(z)]^2\end{aligned}\quad (4.33)$$

where  $\delta E_c$  is the estimated difference between conduction band minima of Si and Ge at L point, and  $a$  is the lattice parameter here taken equal to the one of the substrate.

### Samples linewidth evaluation

In order to analyze the data obtained from FTIR spectroscopy, the theoretical model developed here has been applied to our single-well samples, whose characteristics are summarized in table 4.2 together with the obtained values of  $\Gamma^{th}$ .

To address the relevant contributions to the scattering phenomena influencing the ISB transition linewidth, before discussing the agreement between the experimental and theoretical values it is helpful to start comparing the theoretical linewidth contributions for two different samples, featuring either a narrow (S3) or a wide (S6) QW without the presence of spacer layers. In fig. 4.19 the contributions to  $\Gamma^{th}$  higher than 0.02 meV are plotted as a function of the electron kinetic energy  $E$ . Notice that in these samples the low-temperature estimated values of  $E_F$  (see table 4.2) are relatively low, especially if compared with those obtained in III-V QWs having similar carrier densities. This is due to four degenerate Ge conduction-band minima at the L point which exhibit a large value of the bi-dimensional DOS effective mass. It follows that the scatterings at low temperature  $T$  involve electrons having very small kinetic energies in all the studied samples. Therefore only the inter-subband term of  $\Gamma^{OP}$  may not vanish, while the OP intra-subband broadening, which comprises the Heaviside step function, is always suppressed for energy conservation. On the contrary, for the IFR and II broadenings the dominant contributions are re-

Sample	$d_w$ (nm)	$d_b$ (nm)	$n_{2D}$ ( $10^{11}\text{cm}^{-2}$ )	$E_F$ (meV)	$\Gamma$ (meV)	$\Gamma^{th}$ (meV)	$\tilde{\Gamma}^{th}$ (meV)
S1	13.5	10+ <b>10</b> +10	0.7	0.14	2.1	0.69	2.49
S2	24	10+ <b>10</b> +10	0.9	0.16	2.2	0.39	2.19
S3	10	<b>30</b>	3.4	0.60	5.0	3.19	4.99
S4	12	<b>25</b>	1.2	0.19	4.3	1.37	3.17
S5	24	<b>30</b>	1.5	0.27	3.0	1.07	2.87
S6	24	<b>30</b>	2.0	0.37	3.4	1.54	3.34
S7	12	4+ <b>22</b> +4	2.2	0.39	3.7	1.87	3.67

Table 4.2: Single-well samples properties: QW width  $d_w$ , SiGe barrier width  $d_b$ , well charge density  $n_{2D}$ , evaluated Fermi energy  $E_F$ , experimental linewidth  $\Gamma$ , linewidth prediction  $\Gamma^{th}$ , corrected linewidth theoretical value  $\tilde{\Gamma}^{th}$ . Bold numbers indicate the doped layers, eventually sandwiched between spacer layers.

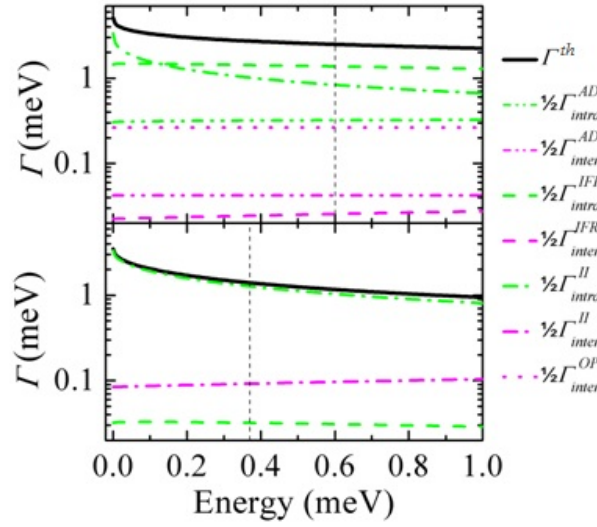


Figure 4.19: Scattering contributions to  $\Gamma^{th}$  for sample S3 (top panel) and S6 (bottom panel) as a function of the kinetic energy  $E$  of the electrons in the first subband  $|0\rangle$ . Vertical dashed lines indicate the calculated Fermi energy  $E_F$ .

lated to intra-subband events, which are up to two orders of magnitude larger than those associated with the inter-subband ones. This fact is due to the larger values of the exchanged momentum  $\bar{q}$  in IFR and II inter-subband scatterings, which exponentially suppress the integrand function reported in equations 4.28 and 4.30.

Another result is that for both narrow and wide wells the term  $\Gamma_{intra}^{II}(E)$  significantly decreases for increasing electron energy. In fact, at larger values of  $E$  the exchanged momentum  $q$  increases, decreasing the value of the integrand in equation 4.30. The other active contributions, instead, remain almost constant in the investigated energy range, as it happens for example to  $\Gamma^{IFR}(E)$ .

While some contributions to the broadening are unimportant for both narrow and wide QWs, some others have a different impact on the total linewidth. In particular,  $\Gamma^{AP}$  is found to be negligible in both samples because of the experimental conditions, since both the intra- and inter-subband terms are proportional to  $T$ . This is not the case of IFR and AD scatterings, since they are much larger in narrow-well samples compared to that of wide-well samples. The reason behind this difference is the larger value of the wavefunction at the well/barrier interface and inside the SiGe barrier. Moreover, in narrow wells we have  $E_{01} > \hbar\omega_{ph}^{LL}, \hbar\omega_{ph}$  and thus the  $\Gamma_{inter}^{OP}$  term also contributes to the linewidth. On the contrary, in wide wells  $E_{01} < \hbar\omega_{ph}^{LL}, \hbar\omega_{ph}$  and the inter-subband OP contribution is as negligible as the IFR and AD ones. Concerning the latter, it is important to notice that the intra-subband term is much higher than the corresponding inter-subband one (see fig. 4.19) because  $\psi_1^2(z) \gg |\psi_0(z)\psi_1(z)|$  in the barrier region, where the integration must be performed.

To understand the effect of the spacer layer, narrow-well samples linewidths have been compared since in this case the wavefunction widely extends into the barrier region [65]. In fig. 4.20 the linewidth broadening contributions of samples S1 and S4 are shown as a function of the electron kinetic energy  $E$ . The two samples have similar well width (13.5 nm and 12 nm) but only S1 features a spacer layer.

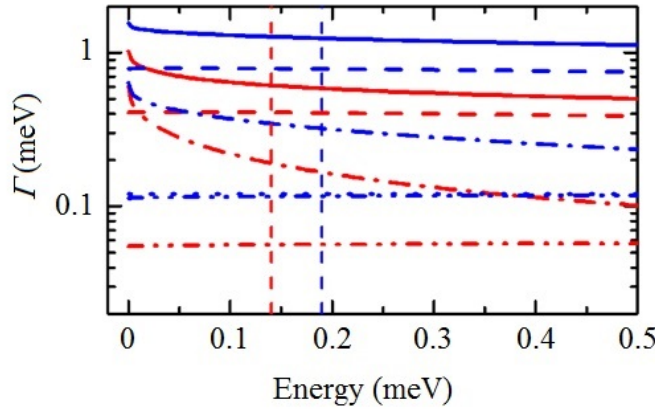


Figure 4.20: Linewidth broadening contributions to  $\Gamma^{th}$  for samples S1 (red lines) and S4 (blue lines):  $\Gamma^{th}(E)$  (solid line),  $\frac{1}{2}\Gamma_{intra}^{II}(E)$  (dash-dotted line),  $\frac{1}{2}\Gamma_{intra}^{IFR}(E)$  (dashed line),  $\frac{1}{2}\Gamma_{inter}^{OP}(E)$  (dotted line), and  $\frac{1}{2}\Gamma_{intra}^{AD}(E)$  (dash-dot-dot line). Vertical lines indicate the calculated Fermi energy  $E_F$ .

As previously commented, the IFR and II scatterings are the predominant channels for both samples, but for sample S4 also the optical phonon scatterings are active and contributes to the linewidth broadening. It is interesting to notice that in the proximity of  $E = 0$  the contribution of II scattering in the two samples is similar, even if S1 has the spacer layer and a carrier density smaller by a factor of  $\simeq 2$ . Increasing the energy, instead, the effects of  $\Gamma_{intra}^{II}$  in the two samples are not comparable anymore, as it decreases more rapidly in sample S1. This result implies that the presence of the spacer layer has a positive impact in the linewidth only for high kinetic energies, while it has a detrimental influence for low values of  $E$ . In order to elucidate this behavior, it is useful to consider again equation 4.30: for small values of  $E$ , the II intra-subband term dominates the inter-subband one, and taking a  $q \rightarrow 0$  limit of  $\Gamma_{intra}^{II}$  a finite value is obtained. Its functional dependence on the distance between the well/barrier interface and the ionized impurity position is not a monotonically decreasing function, as displayed in fig. 4.21 which shows the intra- and inter-subband terms of  $\Gamma^{II}$  originated by a  $\delta$ -like bi-dimensional donor distribution, placed at distance  $Z$  from the center of the well ( $Z = 0$ ).

Curves refer to different values of the electron kinetic energy in the 0–10 meV range, in which the inter-subband contribution depends very weakly on the energy. For modulation doped samples ( $Z > d_w/2$ ),  $\Gamma_{inter}^{II}$  is minimized and smaller than  $\Gamma_{intra}^{II}$ , which instead exhibits a stronger dependence on the electron kinetic energy. Furthermore, for low values of  $E$  (comparable with the Fermi energy of our samples) the intra-subband broadening is larger when the impurity is far from the center of the well, and in the  $E \rightarrow 0$  limit it increases with  $Z$  also in the region beyond the well/barrier interface. This effect tends to disappear at larger energy for which the spacer layer starts to have a beneficial effect on the linewidth, as shortly introduced.

Experimental evidence supporting this statement is the anomalous temperature dependence of the broadening observed in samples with spacer layers. In this case, a slight linewidth decrease is observed as a function of the temperature in the 10–110 K range, as reported in fig. 4.22(a). This behavior could be attributed to the

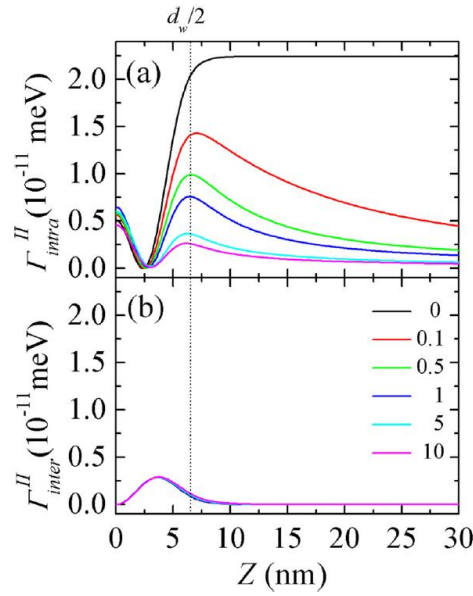


Figure 4.21: Sample S1 (a) intra- and (b) inter-subband  $\Gamma^{II}$  contribution caused by a  $\delta$ -like bi-dimensional donor distribution placed at a distance  $Z$  from the center of the well. Data are plotted for different electron kinetic energy according to the legend in panel (b) expressed in meV. Vertical dotted line indicates the position of the well/barrier interface.

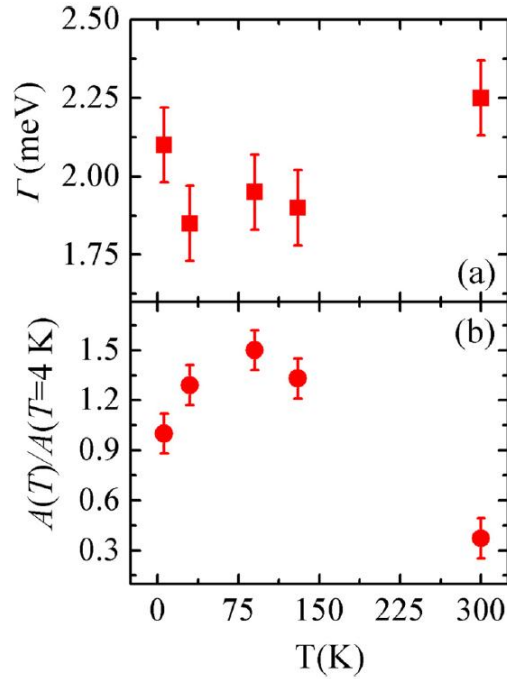


Figure 4.22: Sample S1 experimental linewidth broadening (a) and normalized integrated absorbance (b) as a function of lattice temperature.

temperature-driven increase of the electronic energies which, in turns, enhances the positive effect of the spacer layer on the  $\Gamma_{intra}^{II}$  term. This effect seems to largely compensate for the increase with  $T$  of the ionized impurity density which is deduced by the rise of the integrated absorbance  $A(T) = \int \alpha_{2D}(T, \hbar\omega) d\omega$  in the 10–110 K temperature range shown in fig. 4.22(b). The initial increase of  $A(T)$  is attributed to the larger number of electrons transferred from the donors located in the barrier into the fundamental subband  $|0\rangle$ . The decrease observed in the  $T > 110$  K region is due to the thermal excitation of a portion of the electron density into the first excited subband  $|1\rangle$  [68].

### Calculated values comparison with experimental data

The developed model does not take into account the effect of structural defects on the linewidth broadening, which instead is known to play a significant role. In order to estimate this contribution, we compared the experimental linewidth of two samples featuring large wells (S5 and S6), in which the IFR and OP scatterings are negligible. According to our model, the only dominant contribution is the II one, which approximately depends linearly on the charge impurity density for a given doping profile. Assuming this linear dependence, a residual broadening  $\Gamma_0 \sim 1.8$  meV has been found for wide-well samples without spacer layer, extrapolating the data at  $n_{2D} = 0$ . This procedure is sketched in fig. 4.23(a). We attribute this residual broadening  $\Gamma_0$  mainly to scatterings with defects originated in the substrate and propagating through the sample, but it also includes all the eventual inhomogeneous contributions to the linewidth broadening. In the figure it is also present the value of  $\Gamma$  for sample S2 for comparison, showing how the presence of the spacer layer has only a small impact on the linewidth broadening, since its value is out of the linear extrapolation only by a small quantity. It is clear that the residual broadening  $\Gamma_0$  has to be added to the theoretical evaluations  $\Gamma^{th}$  of the samples linewidth. The corrected theoretical values  $\tilde{\Gamma}^{th} = \Gamma^{th} + \Gamma_0$  are reported in table 4.2 and graphically displayed in fig. 4.23(b) together with the experimental data. The comparison shows an excellent agreement between experimental data and theoretical predictions, highlighting the robustness of the model.

The reported results for the linewidth broadening and the corresponding theoretical values are of great importance also for the estimation of the coherence time

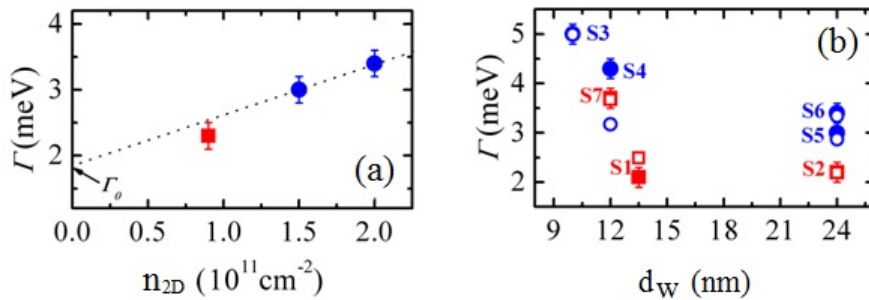


Figure 4.23: Measured values of  $\Gamma$  as a function of carrier density  $n_{2D}$  (a) and well width  $d_w$  (b) for samples with (red squares) and without (blue circles) the spacer layer. Open symbols in panel (b) represent the corresponding theoretical values  $\tilde{\Gamma}^{th}$ .

$\tau_c$ , related to the ISB transition linewidth via the following relation:

$$\Gamma = \hbar \left( \frac{1}{\tau_c} + \frac{1}{2\tau_{10}} \right) \quad (4.34)$$

Since the non-radiative ISB relaxation time  $\tau_{10}$  is much larger than  $\tau_c$  [80, 101], the second term can be neglected and the linewidth  $\Gamma$  is found to be proportional to  $1/\tau_c$ . The reported values of  $\Gamma$  as small as 2 meV lead to coherence times up to  $\tau_c \sim 0.4$  ps. However, the theoretical model suggests that the linewidth is still dominated by the residual broadening  $\Gamma_0$ , thus by extrinsic effects related to structural imperfections. It follows that improving the crystalline quality of the substrate may lead to coherence times  $\tau_c > 1$  ps, a desirable result for every experiment relying to coherence between quantum states in semiconductor heterostructures.

### 4.4.3 Degenerate pump-probe measurements

Besides the coherence time, the other optical parameter important for applications is the lifetime of the excited states inside the QWs. In fact, emitter devices require a long ISB relaxation time at high temperatures in order to ease the establishment of a population inversion between the levels. In this regard, heterostructures in group-IV semiconductors are good candidate because of their non-polar nature. In order to study the electron system dynamics in MQW samples, pump-probe experiments have been performed. The differential transmission change  $\Delta S/S$  has been measured for different MQW samples at different pumping powers  $P$  and lattice temperatures  $T$ , and the system relaxation back to the equilibrium has been

Sample	$E_{01}$ (meV)	$T$ (K)	$P$ (mW)	$\tau_{10}$ (ps)
S1	28.8	4	40	33
		50	40	33
		130	40	33
S2	14.9	30	40	34
		90	40	34
S6	18.0	4	40	27
		30	40	34
		90	40	30
S4	37.0	4	8	57
		60	8	31
		4	750	25
S4bis	39.0	4	8	65
		90	8	24
		90	300	19

Table 4.3: Experimental conditions and fit results of the pump-probe measurements.

extracted as the relaxation time  $\tau_{10}$  from the excited subband  $|1\rangle$  to the ground subband  $|0\rangle$ .

The experimental conditions in which different pump-probe measurements are performed have been summarized in the table 4.3 together with the corresponding results [80,101]. In order to highlight any eventual difference in the relaxation times for different doping techniques, the sample S4bis has been grown as a copy of sample S4 but with a different doping technique. In fact, sample S4bis is realized with the direct doping technique instead of the modulation doping adopted for the other samples, and the comparison with sample S4 was conducted within a second run of experiment. Since the structural characteristics are all the same, any important difference in the relaxation dynamics has to be ascribed to the different doping technique or to the different charge density in the ground subband.

In the first set of measurements, performed on samples S1, S2 and S6, the power was kept fixed at 40 mW, while the lattice temperature  $T$  was varied from 4 K to 130 K. In this conditions, the extracted relaxation times are found almost constant with increasing lattice temperature. In fig. 4.24 the spectra of sample S2 acquired at 30 and 90 K are reported. It is evident that the measurements at both lattice temperatures highlight the same relaxation time of  $\tau_{10} = 34$  ps. The same behavior has been observed in the differential transmission change of samples S1 and S6. According to what previously discussed, this behavior is due to the high electron temperature  $T_e$  generated with pumping powers of 40 mW, and the effect of a changing lattice temperature is therefore completely hidden. In order to highlight and study a change in the relaxation times with lattice temperature, measurements on samples S4 and S4bis have been performed employing a drastic variation in the pumping power, from very low values of 8 mW to very high values of 750 mW. In this way, we were able to investigate the system relaxation dynamics as a function of both lattice and electron temperatures  $T$  and  $T_e$ . The acquired spectra for samples S4 and S4bis are reported in fig. 4.25, together with the predictions obtained by the model developed and discussed in section 4.2. The electron temperatures  $T_e$  calculated by the discussed model are also reported. Notice that since the temperature  $T_e$  of the electronic system is the direct consequence of the energy absorbed by the incident radiation of the pumping beam, the same peak value of the differential transmission change  $\Delta S/S$  before relaxation (pump-probe coincidence, at null value of delay time)

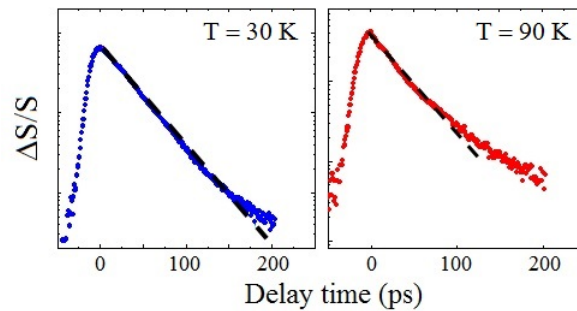


Figure 4.24: Pump-probe signals  $\Delta S/S$  as a function of pump-probe delay time for sample S2 at  $T = 30$  K (left panel) and  $T = 90$  K (right panel). Dashed black lines indicate the exponential fit result, returning the same relaxation time of 34 ps.



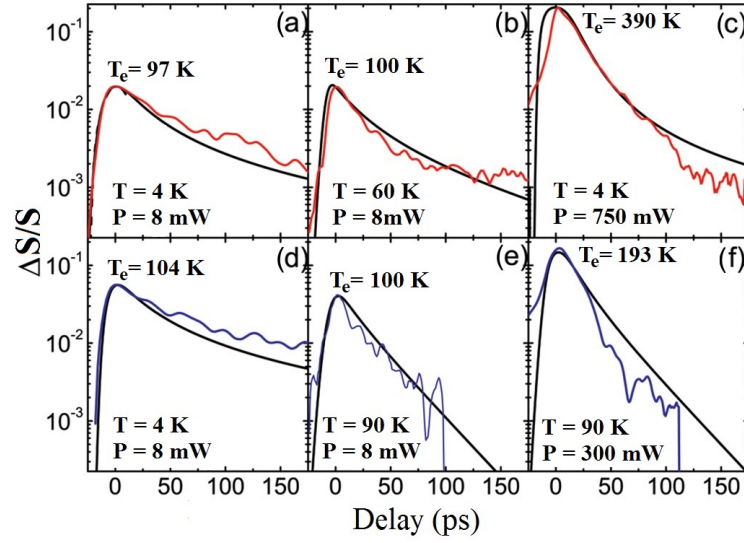


Figure 4.25: Pump-probe signals  $\Delta S/S$  as a function of pump-probe delay time for sample S4 (panels a-c) and S4bis (panels d-f) at different temperatures and pump powers. Solid black lines are the theoretical results obtained from the model discussed in reference [80].

corresponds to the same temperature  $T_e$  of the electronic system.

Looking at the data in the figure, it is possible to notice that the peak value of the signal increases with pumping powers because of a higher amount of energy transferred to the electron system, which therefore is characterized by a higher temperature  $T_e$ . This means that a larger fraction of electrons populates the excited subband with sufficient energy to emit optical phonons. The opening of this scattering channel results in a more effective cooling of the electron system. The consequence is that the emission of optical phonons is suppressed at longer delay times, leaving the acoustic phonon scattering the only relaxation mechanism. When the dynamics is dominated by the acoustic phonons interaction, the relaxation time scale is larger and this change of behavior is considered to be responsible for the multi-exponential decay observed in the spectra and in the simulated curves. This conclusion is supported by the simulations discussed in section 4.2.

Concerning sample S4 (top panels in fig. 4.25), the differential transmission changes at low pumping powers exhibit a comparable peak value, although the base lattice temperature is significantly different. This behavior confirms that the electron temperature is almost the same in the cases of fig. 4.25(a-b), around a value of  $T_e = 100$  K. The effect of the difference in lattice temperatures of  $T = 4$  K and  $T = 60$  K is a different dynamics after pumping, characterized by an initial relaxation time of 57 and 31 ps, respectively. Being comparable to the electron temperatures, the faster initial relaxation rate observed at  $T = 60$  K is to be entirely attributed to a larger phonon population, since a more efficient stimulated emission of optical phonons can be achieved at higher lattice temperatures. The same argument stands for sample S4bis (panels d-e), in which a higher peak value of the pump-probe signals  $\Delta S/S$  is associated to higher charge density in the well obtained with the more effective direct doping technique. In fact, the amount of optical energy absorbed by each electron in sample S4 and S4bis is found to be equal

within the experimental error. Since in the two samples the donors are located in different regions, i.e. barrier and well, their interaction with the confined electron wave functions is different. This leads to the conclusion that impurity scattering does not play a major role in the non-radiative relaxation dynamics, and therefore the modulation doping technique does not add any significant advantage in terms of relaxation times.

At higher pumping powers, the signals exhibit a higher peak value in both samples as expected from the above discussion. In fact, the calculated electron temperatures are much higher compared to the case of low pumping powers (390 and 190 K in samples S4 at 750 mW and sample S4bis at 300 mW, respectively). In this case, a much higher fraction in subband  $|1\rangle$  can relax towards subband  $|0\rangle$  via phonon emission, and much shorter relaxation times are obtained.

The degenerate pump-probe experiments here reported confirmed the prediction of very long ISB relaxation times in Ge/SiGe QWs up to 65 ps. Although the higher values are obtained at low lattice temperatures and low pump powers, the relaxation dynamics at higher temperatures and powers takes place at time scale not shorter than 20 ps, which can be anyway considered a high value compared to the relaxation times of few picoseconds due to the Fröhlich interaction. These results support the feasibility of Ge-based ISB emitters in the THz range, capable of higher temperature operation with respect to the more common devices based on III-V materials.

## 4.5 Optical characterization of ACQW samples

The long ISB relaxation times obtained from MQW samples strongly suggest the possibility to realize a THz emitter device. In fact, the high values reported in the previous section should be suitable to guarantee the establishment of a population inversion between the confined levels of a QW structure. This peculiarity of the group-IV materials has thus been exploited in the 3-level ACQW samples, in which the long ISB relaxation times and a proper wavefunction engineering should in principle ensure light emission. To this aim, optical measurements on samples S8 and S9 have been performed with the pump-probe/TDS technique at the FELBE facility, in order to investigate the possibility to achieve population inversion.

### 4.5.1 Quantum Fountain

The optical properties of the heterostructures discussed so far and the corresponding ISB transition selection rules can be tuned to match the desired characteristics needed in order to realize an opto-electronic device. This is possible by employing the ACQW design already described, in which the stationary levels established in the structure lose the defined symmetry they would have in a symmetric QW system and the overlap of their wavefunctions can be engineered changing the structural parameters. This tuning wavefunction overlap reflects the asymmetry of the structure. In fact, since each level does not have a defined symmetry anymore, any ISB transition is in principle allowed even if modulated in intensity by the actual wavefunction overlap integral of the levels involved in the transition. If, for example, the  $|0\rangle \rightarrow |2\rangle$  ISB transition is forbidden in a single (thus symmetric) QW, it becomes

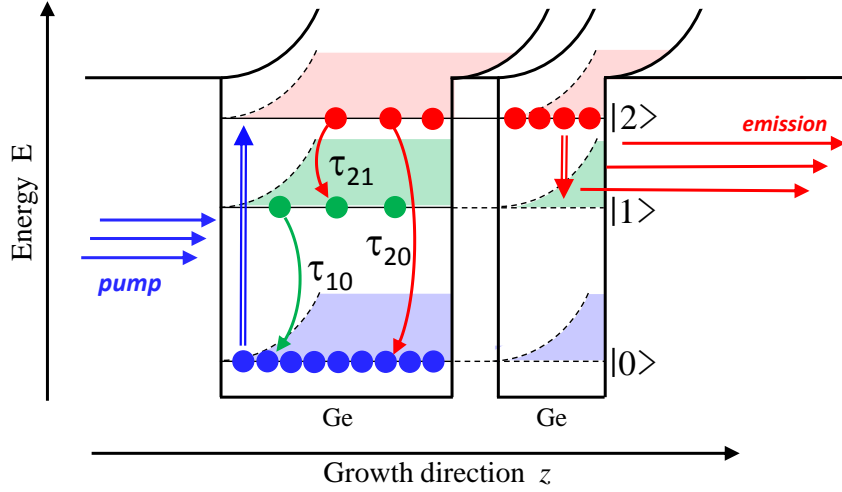


Figure 4.26: Operation scheme of a QF device. The three subbands and their in-plane parabolic dispersion are indicated with different colors, while the black thick line represents the conduction band profile. Straight vertical arrows represent the radiative transitions while the curved arrows represent the non-radiative ones.

allowed in an ACQW system. This important result can be exploited within the so-called *quantum fountain* (QF) device [33–39, 103]. Such emitter is based on a 3-level ACQW design in which the electrons are optically pumped from level  $|0\rangle$  to level  $|2\rangle$  in order to generate light emission resulting from the radiative transition towards the almost unoccupied level  $|1\rangle$ . Electrons can then relax back to the fundamental level  $|0\rangle$  hence depopulating level  $|1\rangle$  and allowing further transitions from level  $|2\rangle$ , as depicted in fig. 4.26. The establishment of this loop process does not guarantee radiative emission itself, since two crucial conditions must be fulfilled: the first one is a long non-radiative ISB transition time  $\tau_{20}$  of the direct relaxation channel  $|2\rangle \rightarrow |0\rangle$  and the second one is that the ISB relaxation time  $\tau_{10}$  of the  $|1\rangle \rightarrow |0\rangle$  transition has to be much shorter than the relaxation time  $\tau_{21}$  of the  $|2\rangle \rightarrow |1\rangle$  transition. With these two conditions satisfied, the population inversion  $\Delta n = n_2 - n_1 > 0$  is established during pumping. The population inversion can be approximately related to the ISB relaxation times through the following relation [103]:

$$\Delta n \sim \left(1 - \frac{\tau_{10}}{\tau_{21}}\right) n_2 \quad (4.35)$$

Positive gain can be therefore achieved for high population  $n_2$  and low relaxation times ratio  $\tau_{10}/\tau_{21}$ , obtained by varying the wells width and especially the thickness of the barrier in the middle, i.e. by tuning the wavefunctions overlap inside the structure and the resulting ISB transition probability. This wavefunction engineering, performed exploiting the asymmetry of the structure, is the first step towards the realization of a QF device because it sets the proper relaxation times of each ISB transition.

### 4.5.2 Absorption energies

The prediction on energy levels inside an ACQW system is a task that demands a better approach compared to the single isolated QW case described in section 2.1, and requires numerical methods. In this regard, the quantum state design for samples S8, S9 and S10 was conducted in collaboration with “Università di Pisa”, employing a multi-valley self-consistent effective mass calculation, in order to obtain the proper conduction band profile at L point, the energy of the confined levels and the corresponding wavefunctions. The design has been performed by varying the geometrical parameters within the available ranges [65, 68] trying to obtain a transition energy  $E_{01}$  close to the [111] zone-boundary optical phonon energy of  $E_{ph,\Lambda} \simeq 24$  meV [100] for fast depopulation of level  $|1\rangle$  and, at the same time, a transition energy  $E_{12}$  lower than the phonon one to guarantee a long lifetime of the excited state  $|2\rangle$ . Contrary to what happens in III-V systems, we could not exploit the sharp resonance of the  $|1\rangle \rightarrow |0\rangle$  ISB transition, because of the different behavior of the electron interaction with optical phonons as a function of the subband separation. As already discussed in section 4.2, the polar nature of materials like GaAs implies a sharp resonance in the transition rate when the subband separation equals the optical phonon energy. This property is largely exploited in several devices as QFs or QCLs to achieve a fast and efficient depopulation of subband  $|1\rangle$  in order to establish a population inversion between subbands  $|1\rangle$  and  $|2\rangle$ . Group-IV semiconductors like Ge do not feature this sharp resonance because the coupling interaction with optical phonons does not depend on the exchanged momentum. Here, we therefore design the QF system exploiting the long ISB relaxation times in Ge QWs to obtain a long lifetime of the state  $|2\rangle$ , increased even more by a proper wavefunction engineering. Figure 4.27 shows the scheme of sample S9, in which the predicted ISB transition energies are indicated.

The results obtained from the performed calculation are displayed in table 4.4 together with the structural parameters of the samples, and can be compared to the experimental data obtained by FTIR spectroscopy, which are reported in fig. 4.28. At low temperature ( $T = 10$  K), only the  $|0\rangle \rightarrow |1\rangle$  transition is observed, centered between 22 and 26 meV according to the different structural parameters of the samples. The other transitions are absent in the spectra for several reasons. Concerning the  $|0\rangle \rightarrow |2\rangle$  transition that should be used for optical pumping in a QF device, despite the selection rule inhibiting the transition is violated due to asymmetry of the QW structure, the wavefunction overlap between level  $|0\rangle$  and  $|2\rangle$

Sample	$d_w$ (nm)	$d_b$ (nm)	$E_{01}$ (meV)	$E_{02}$ (meV)	$E_{12}$ (meV)
S8	<b>13</b> +4.5	30	26	41	15
S9	<b>15</b> +5.5	30	22	34	12
S10	<b>15</b> +3.5	30	23	48	25

Table 4.4: ACQW samples quantum well width  $d_w$ , barrier width  $d_b$ , and predicted ISB transition energies. Bold numbers indicate the doped layers.

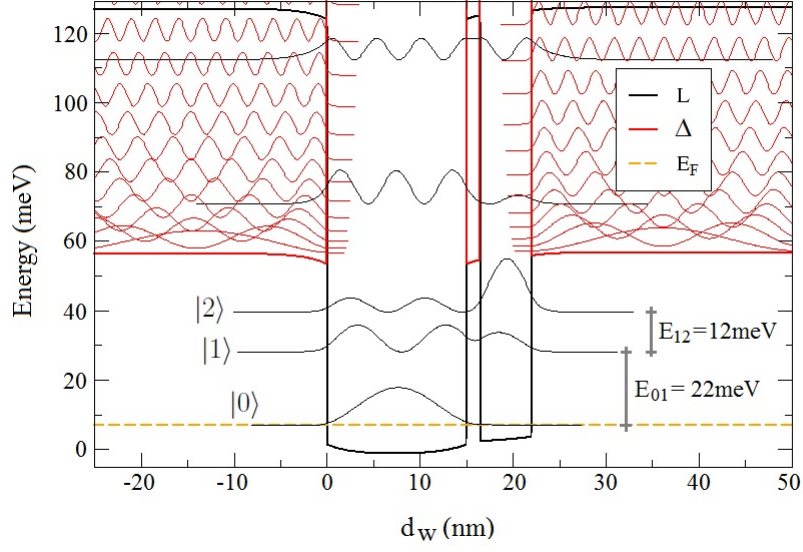


Figure 4.27: Calculations on S9 conduction band profile and squared modulus of the level wavefunctions at L point (black lines) and  $\Delta$  point (red lines). Calculated Fermi level at low temperature (yellow line) and predicted transition energies  $E_{01}$  and  $E_{12}$  are also indicated.

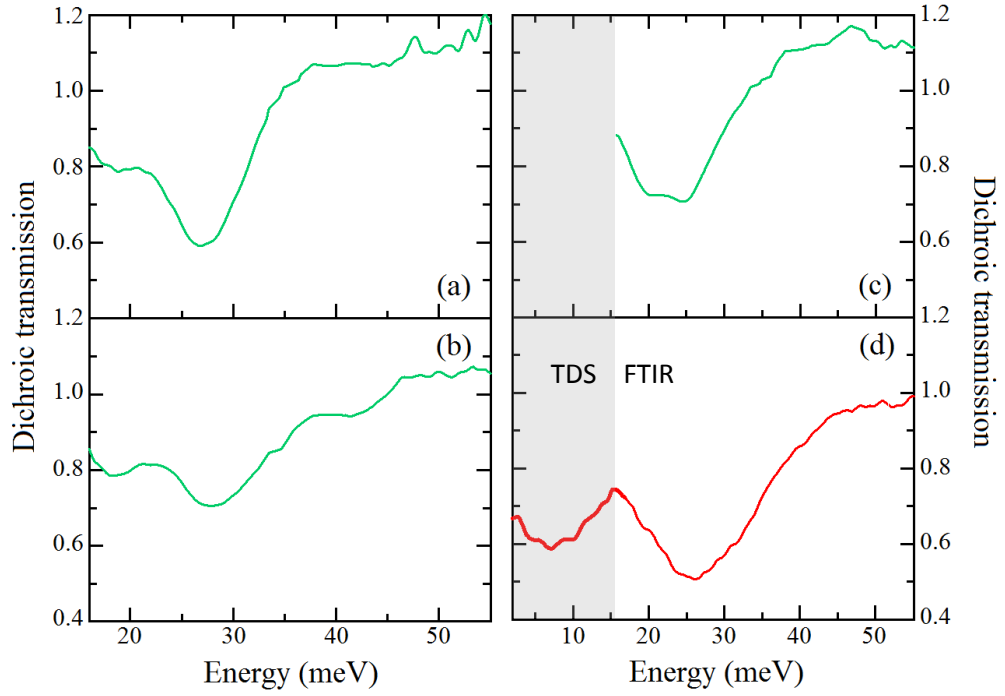


Figure 4.28: Low temperature dichroic signal of samples S10 (a), S8 (b) and S9 (c) obtained by FTIR measurements. Panel (d) displays the room temperature dichroic signal of sample S9 extended with TDS. The shaded area of the plot represents the energy range accessible only by TDS.

is still very low, leading to a small absorption probability at  $E_{02}$ . This choice of low wavefunction overlap, made at the design stage, prevents the fast depopulation of the subband  $|2\rangle$  towards subband  $|0\rangle$  but implies that the selection rules is not enough violated to allow the detection of the absorption peak with the FTIR setup. The optical pumping, instead, will be performed with a proper source (the FEL) delivering to the samples powers of several orders of magnitude higher than the one employed in the FTIR measurements. Concerning instead the  $|1\rangle \rightarrow |2\rangle$  ISB transition, the starting level is empty at  $T = 10$  K and the transition cannot be observed. At room temperature (300 K), the transition should be visible due to significant thermal population of level  $|1\rangle$ , however, depending on the sample, it falls either out of the range of the FTIR setup or within the broad range of the more intense dip related to the  $|0\rangle \rightarrow |1\rangle$  transition.

Starting from fig. 4.28(a), the dichroic signal of sample S10 displays an intense ISB absorption centered at 26 meV, which is compatible with the predicted  $|0\rangle \rightarrow |1\rangle$  transition at 23 meV. The remaining mismatch is possibly due to uncertainties in the charge density in the well that ultimately sets the transition resonance after consideration of the depolarization shift. The much weaker  $|1\rangle \rightarrow |2\rangle$  transition falls at  $E_{12} = 25$  meV, well inside the  $|0\rangle \rightarrow |1\rangle$  transition dip and it is therefore not observable even at room temperature. The experimental data of sample S10 are in good agreement with the theoretical predictions and contribute to proof the robustness of the design, growth and modeling procedures adopted. However, the energy overlap of the  $|0\rangle \rightarrow |1\rangle$  and  $|1\rangle \rightarrow |2\rangle$  transition makes this sample not a good candidate for the ISB relaxation time investigation, which will be instead performed on the other two samples.

In sample S8 (fig. 4.28(b)) the narrow well thickness was increased to 4.5 nm if compared to sample S10 and the wide well thickness was reduced to 13 nm. Correspondingly, the  $|0\rangle \rightarrow |1\rangle$  transition appears at the slightly higher energy of  $E_{01} = 28$  meV. The  $|1\rangle \rightarrow |2\rangle$  transition is predicted at  $E_{12} = 15$  meV but is not observed in the FTIR spectra even at room temperature due to the lower electron population obtained in this specific sample, evident from the lower spectral weight of the  $|0\rangle \rightarrow |1\rangle$  transition at low temperature.

Finally, in fig. 4.28(c) the dichroic signal of sample S9 at low temperature is shown. The wide well thickness is 15 nm as for sample S10, hence the  $|0\rangle \rightarrow |1\rangle$  ISB transition appears almost at the same energy of  $E_{01} = 25$  meV. The larger thickness of the narrow well (5.5 nm compared to 3.5 nm) sets the predicted  $|1\rangle \rightarrow |2\rangle$  transition energy to  $E_{12} = 12$  meV. This value is outside the range of the FTIR setup in waveguide configuration, but it can be extended with the help of the TDS setup. In this case, the GaP crystal pair is used instead of the more common ZnTe, in order to exploit a larger energy range at the cost of efficiency [104, 105]. Figure 4.28(d) shows the room temperature spectrum obtained by merging the FTIR dichroic signal and the same quantity measured by TDS, rotating the sample in the THz-TDS beam to acquire the transmittance in both TE and TM polarizations independently. In the merged dichroic spectrum, the  $|1\rangle \rightarrow |2\rangle$  transition appears as a broad dip centered around 10 meV, less intense than the  $|0\rangle \rightarrow |1\rangle$  transition. Since both the ISB transitions involved in the QF emission has been clearly identified confirming the predicted properties obtained by calculations, sample S9 is the best candidate to study the relaxation dynamic of the ACQW structure.

### 4.5.3 Relaxation times

The relaxation times related to the ISB transitions in ACQW samples have been measured employing the pump-probe/TDS technique. The theoretical differential transmission change  $\Delta S/S$  and global relaxation time  $\tau_R$  obtained by the model described in section 4.2 can be directly compared to the experimental data, as reported in table 4.5 for different temperatures  $T$  and pump powers  $P$ . The experimental pump-probe curves of sample S9 are displayed in fig. 4.29 together with the model results. As already discussed, even if the measured electric field change  $\Delta F_{max}(t')$  is distinct from the optical transmission, both quantities are determined by the electron dynamics as clear from the behavior of the relative subband populations  $\Delta n_i/n_{tot}$  displayed in the figure. Therefore, both  $\Delta F_{max}(t')$  and  $\Delta S/S$  return back to equilibrium with the same characteristic time  $\tau_R$ . The electric field change  $\Delta F_{max}(t')$  was always found to be negative, therefore it is reported as  $-\Delta F_{max}(t')$  in fig. 4.29 for clarity. This negative sign indicates that the pump induces a decrease of the frequency-integrated TM transmittance, due to the free carrier absorption increase.

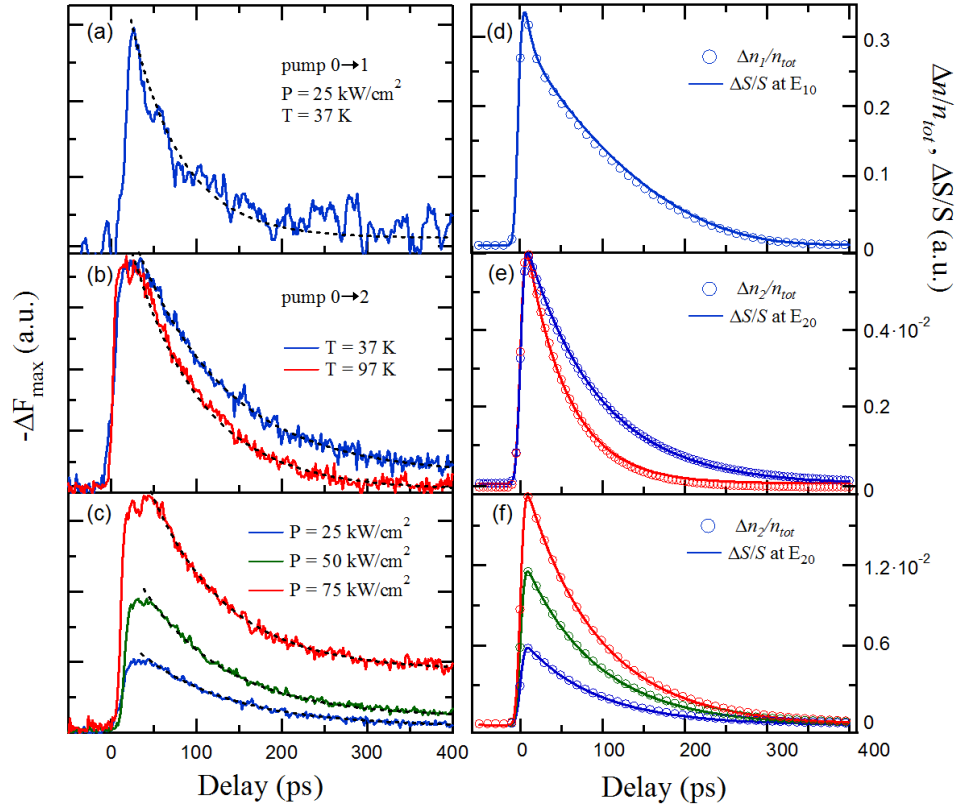


Figure 4.29: Relaxation dynamics of sample S9. Left panels: data (continuous lines) and fits (black dashed lines) of the THz electric field intensity change as a function of pump-probe delay for different temperatures  $T$  and pump powers  $P$ . Right panels: results of the out-of-equilibrium model for the optical transmittance change  $\Delta S/S$  and population variations  $\Delta n_i/n_{tot}$  of the pumped levels referred to the total electron density at the corresponding  $T$  and  $P$  values.

$T$ (K)	$P$ (kW/cm <sup>2</sup> )	$E_{FEL}$ (meV)	$\tau_R$ (ps)	$\tau_R^{th}$ (ps)	$\tau_{10}$ (ps)	$\tau_{20}$ (ps)	$\tau_{21}$ (ps)
37	17	25	60	15-90	15-90	-	-
37	25	41	106	80	30	100	$\gg \tau_{21}^{ac}$
37	50	41	96	81	30	90	$\gg \tau_{21}^{ac}$
37	75	41	88	82	30	90	$\gg \tau_{21}^{ac}$
97	60	41	81	50	6	90	200

Table 4.5: Experimental ( $\tau_R$ ) and theoretical ( $\tau_R^{th}$ ) relaxation times of sample S9 at different temperatures  $T$ , pump powers  $P$  and pump energies  $E_{FEL}$ . The ISB relaxation times  $\tau_{jk}$  obtained from the model are also reported, where  $\tau_{21}$  at low  $T$  is found to be much higher than the typical acoustic phonons relaxation times.

When pumping at  $E_{FEL} = E_{01} = 25$  ( $\lambda_{FEL} = 50$   $\mu\text{m}$ ), a large population variation is generated. This large variation is due to a high overlap of the first two wavefunctions  $\psi_0(z)$  and  $\psi_1(z)$  obtained with the wavefunction engineering, which determines a large ISB absorption coefficient. The character of this transition is thus similar to what is expected in a single isolated QW, and the relaxation time  $\tau_R$  is considered to be determined mainly by the  $|1\rangle \rightarrow |0\rangle$  ISB transition characterized by a relaxation time  $\tau_{10}$ . The out-of-equilibrium model provides a multi-exponential behavior with relaxation times increasing from 15 to 90 ps as the electron temperatures decrease. In other words, the relaxation back to the equilibrium is in this case dominated by the dynamics of population  $n_1$ , as clear from fig. 4.29(d) and considering that at low temperature  $n_2 \simeq 0$ . The experimental value of  $\tau_R = 60$  ps here obtained for pumping at the 25 meV is comparable to the rather long relaxation times of 30-60 ps already found in degenerate pump-probe measurements on MQW samples (see section 4.4.3).

When pumping at  $E_{FEL} = 41$  meV ( $\lambda_{FEL} = 30$   $\mu\text{m}$ ) above the  $|0\rangle \rightarrow |2\rangle$  ISB transition at  $E_{02} = 35$  meV, small population variations are induced due to the small absorption coefficient and a single-exponential fit reasonably reproduces the  $\Delta F_{max}(t')$  data of fig. 4.29(b-c), with  $\tau_R$  in the range of 80-110 ps (see table 4.5). Even if  $E_{02} \simeq E_{ph,\Gamma}$  meV, the out-of-equilibrium model shows that  $\tau_{20} \simeq 100$  ps, due to the small overlap of  $\psi_0(z)$  and  $\psi_2(z)$  in the ACQW structure obtained by the wavefunction engineering. Furthermore, we found  $\tau_{21} \gg \tau_{20} > \tau_{10} = 30$  ps at all the explored  $T$  and  $P$  values. The comparison of these values with the observed  $\tau_R$  allows to safely ascribe the slow experimental relaxation to the direct  $|2\rangle \rightarrow |0\rangle$  non-radiative transition by phonon emission with  $\tau_{20} \simeq 100$  ps. In fact, referring to the QF scheme depicted in fig. 4.26, the relaxation of the excited state  $|2\rangle$  can occur directly towards the ground level  $|0\rangle$  or towards level  $|1\rangle$  and level  $|0\rangle$  right after. Hence, the global relaxation time of the system pumped around  $E_{02}$  is expressed by:

$$\frac{1}{\tau_R} = \frac{1}{\tau_{20}} + \frac{1}{\tau_{21} + \tau_{10}} \quad (4.36)$$

At low temperature, the model shows values for  $\tau_{21}$  longer than 1 ns, because the ISB transition energy  $E_{12}$  is much lower than any optical phonon energy  $E_{ph}$ .



However, the values of  $\tau_{21}$  are found to be extremely high because the employed model takes into account only the relaxation mechanism due to optical phonon scattering. In a more realistic scenario, also the interaction with acoustic phonons should be considered, leading to a scattering rate determined by both contributions:

$$\frac{1}{\tau_{21}} = \frac{1}{\tau_{21}^{op}} + \frac{1}{\tau_{21}^{ac}} \quad (4.37)$$

where  $\tau_{21}^{op}$  is the contribution of the optical phonon scattering and  $\tau_{21}^{ac}$  the contribution by acoustic phonons, which is in the range of 200-500 ps [67, 80]. Since the calculated values of  $\tau_{21}^{op}$  are found to be much larger than  $\tau_{21}^{ac}$ , the values of the relaxation time  $\tau_{21}$  are mostly ascribed to the acoustic phonon interaction:

$$\tau_{21}^{op} \gg \tau_{21}^{ac} \Rightarrow \frac{1}{\tau_{21}} = \frac{1}{\tau_{21}^{op}} + \frac{1}{\tau_{21}^{ac}} \simeq \frac{1}{\tau_{21}^{ac}} \ll \frac{1}{\tau_{20}} \quad (4.38)$$

Therefore in equation 4.36  $\tau_R \simeq \tau_{20}$ .

Concerning the measurements at high temperature ( $T = 97$  K), the decrease of  $\tau_R$  from 106 to 81 ps is also consistent with the presented interpretation, because a higher lattice temperature corresponds to a higher temperature of the electronic system in subband  $|2\rangle$ , which can exhibit energy comparable to  $E_{ph}$  and therefore relax towards subband  $|1\rangle$  via optical phonon scattering. This leads to the decrease of  $\tau_{21}^{op}$  from 1 ns to 200 ps compared to the case of low temperature. As a consequence, the second term of equation 4.36 is no more negligible and  $\tau_R$  becomes smaller.

Basing on these results, a more realistic value of  $\tau_{21} \simeq 200$  ps has been used to calculate the relaxation time ratio  $\tau_{10}/\tau_{21} \simeq 0.15$ , which is an important parameter related to radiative emission. Such extremely low value of  $\tau_{10}/\tau_{21}$  is favorable for population inversion between the two excited levels [90, 103], here obtained by exploiting the slow relaxation of the transition with  $E_{12} < E_{ph}$  instead of exploiting the fast phonon-resonant depopulation of the lower excited level as previously done in QF devices realized in III-V semiconductor compounds [33, 34, 102]. This is an important achievement of the present work, which may lead to radiative emission in future devices based on ACQW structures realized in Si-compatible materials. In summary, the results of the conducted investigation highlight a non-radiative ISB dynamics in Ge ACQWs rather slow if compared to similar structures previously realized in III-V compound semiconductors [35, 103, 106, 109].

#### 4.5.4 Spectral analysis and gain extrapolation

The transmittance of the samples in the non-equilibrium conditions achieved with pumping has been studied using the Fourier transform of the recorded time traces  $F(t)$  of the probe electric field at coincidence with the pump and 50 ps before the pump pulse arrives. The difference of the two spectrally-resolved transmitted intensity spectra  $H(\omega)$  divided by the spectral content of the probe pulse (see fig. 4.13(b)) provides information on the electron distribution generated by the pump, through the analysis of the transmittance change  $\Delta H/H$  shown in fig. 4.30(a).  $H(\omega)$  is directly proportional to the transmittance  $S(\omega)$  so that  $\Delta H/H = \Delta S/S$ .

In order to correctly interpret the acquired data, a theoretical model of radiation transmission through our samples has been here used starting from reference [107].

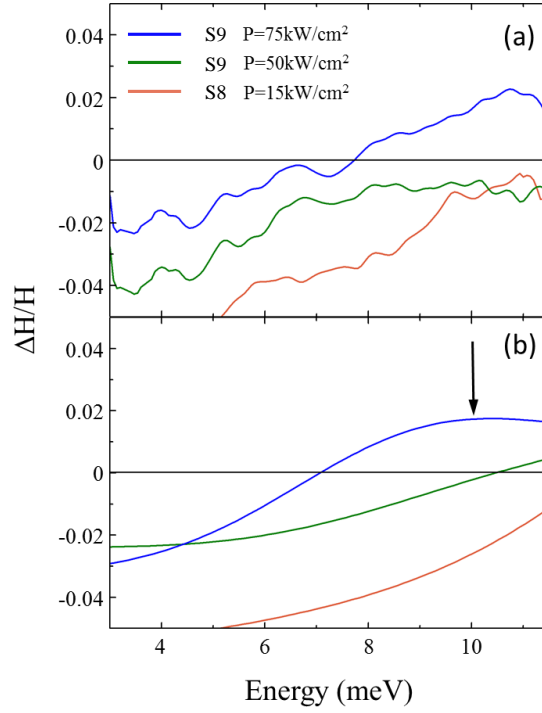


Figure 4.30: Low temperature ( $T = 37$  K) spectrally resolved data (a) and electrodynamic model (b) of the relative transmittance change of the probe pulse for sample S9 pumped at  $75 \text{ kW/cm}^2$  (blue) and  $50 \text{ kW/cm}^2$  (green), and for sample S8 pumped at  $15 \text{ kW/cm}^2$  (orange). The arrow at  $10 \text{ meV}$  indicates the photon energy at which the lorentzian peak corresponding to the  $|1\rangle \rightarrow |2\rangle$  ISB transition is centered.

Following this model, the transmittance  $S(\omega)$  of a thin absorbing film on a transparent substrate of refractive index  $\eta$  can be written in terms of the complex conductivity  $\tilde{\sigma}(\omega)$  of the film as:

$$S(\omega) = \frac{4\eta}{(Z_0 d \sigma' + \eta + 1)^2 + (Z_0 d \sigma'')^2} \quad (4.39)$$

where  $\tilde{\sigma}(\omega) = \sigma'(\omega) + i\sigma''(\omega)$  is the complex optical conductivity of the film. The absorption path length and the refractive index were set to  $d = 14 \text{ }\mu\text{m}$  and  $\eta = 3.5$  respectively, while  $Z_0$  is the free space impedance. The value of  $d$  accounts for an optical path with multiple reflections through the QW stack thickness along the waveguide length. The optical conductivity is modeled as the sum of a Drude term related to free carriers plus three Lorentz oscillators representing the three ISB transitions from level  $j$  to level  $k$  ( $0 \leq j < k \leq 2$ ):

$$\tilde{\sigma}(\omega) = \frac{\sigma_D}{1 - i\omega/\gamma_D} + \sum_{j < k} \frac{\omega I_{L,jk}}{i(\omega_{L,jk}^2 - \omega^2) + \omega \gamma_{L,jk}} \quad (4.40)$$

where  $\sigma_D$  and  $\gamma_D$  are the Drude conductivity and scattering rate, while  $\omega_{L,jk}$ ,  $\gamma_{L,jk}$  and  $I_{L,jk}$  are the Lorentz oscillator frequency, linewidth and strength, respectively. The Lorentz oscillator frequencies are set by the relation  $\hbar\omega_{L,jk} = E_{jk}$  and  $\gamma_{L,jk}$

by the ISB transition linewidths. The Lorentz oscillator strength  $I_{L,jk} \sim (n_j - n_k)$  depends on the relative occupation of levels  $j$  and  $k$ , and can become negative in case of population inversion. The quantity  $\sigma_D \gamma_D = 4\pi n_{3D} e^2 / \varepsilon_0 m^*$  is called *Drude weight* and it is proportional to the energy dissipated by the free carriers. Both  $\sigma_D$  and  $\gamma_D$  were initially set as free parameters of the fit procedure, resulting in variations of  $\gamma_D$  below the 1%. Since high variations of the pumping powers were found to induce negligible variations in  $\gamma_D$ , here this parameter is considered constant and equal to  $\gamma_D = 250 \text{ cm}^{-1}$ . The only free parameters able to vary in the fit of  $\tilde{\sigma}(\omega)$  are therefore  $I_{L,jk}$  and  $\sigma_D$ .

In fig. 4.30(a) the pump-induced relative transmitted intensity change is displayed for sample S8 and S9 at different pumping powers  $P$ , while fig. 4.30(b) shows the theoretical transmittance changes  $\Delta S/S$  obtained with the described model, whose corresponding Drude-Lorentz parameters are reported in table 4.6. As clear from the figure, the experimental data are reasonably reproduced with this model, given the small number of degrees of freedom. The fit values obtained for the Drude conductivity  $\sigma_D$  imply a Drude weight 25 times lower than what expected if generated by the whole three-dimensional free carrier density present in the system. This result is consistent with the adopted experimental conditions, in which the incident beam is TM-polarized and the in-plane absorption is strongly suppressed.

The only observable effect in sample S8 is the reduction of the transmitted intensity  $H(\omega)$  compared to the case of zero pump power ( $\Delta H/H < 0$ ), attributed to the increase of the Drude weight  $\sigma_D \gamma_D$ . No information can be obtained on the population because the  $|1\rangle \rightarrow |2\rangle$  ISB transition falls outside the accessible spectral range of the THz probe. Owing to the smaller electron density in sample S8, as seen from the FTIR analysis in section 4.1.3, a lower power level is sufficient to induce relative changes comparable to that of sample S9 at higher  $P$ . Here instead, beyond the increase of the Drude weight, a reduced strength  $I_{L,12}$  of the Lorentz oscillator centered at  $E_{12} = 10.4 \text{ meV}$  is also observed due to the increase of the population in the upper level. This bleaching effect in sample S9 explains the positive overshoot of  $\Delta H/H$  above 10 meV, marked by the arrow in fig. 4.30(b). Physically, the increase

Sample	P (kW/cm <sup>2</sup> )	$\sigma_D(0)$ ( $\Omega^{-1}\text{cm}^{-1}$ )	$\gamma_D$ (cm <sup>-1</sup> )	$I_{L,12}$ (cm <sup>-2</sup> )	$\gamma_{L,12}$ (cm <sup>-1</sup> )	$\hbar\omega_{L,12}$ (meV)
S8	0	23	250	0.62	125	15.0
	15	27	250	0.59	125	15.0
S9	0	40	250	1.12	125	10.4
	50	45	250	1.09	125	10.4
	75	47	250	0.84	125	10.4

Table 4.6: Drude-Lorentz model parameters at  $T = 37 \text{ K}$  and different FEL pump powers  $P$ : Drude conductivity  $\sigma_D(0)$  and scattering rate  $\gamma_D$ , intensity of Lorentz oscillators  $I_{L,12}$  with linewidth  $\gamma_{L,12}$ , centered at the frequency  $\omega_{L,12}$  corresponding to the nominal  $|1\rangle \rightarrow |2\rangle$  transition energy. Values of  $\gamma_D$  and  $\gamma_{L,12}$  are purposely kept constant to a best-fit value for all samples and powers.

of the Drude weight under pumping can be explained with the removal of some of the electrons from the fundamental level, which reduces the Pauli blocking effect and allows more free carrier scattering processes. In fact, after the pump pulse arrives part of the electrons are excited in the upper level  $|2\rangle$  and the free carrier absorption takes place therein too, increasing the numbers of electrons able to absorb radiation.

The modulation of the Lorentz oscillator intensity strength  $I_{L,12} \sim (n_1 - n_2)$  with the relative occupation of the two excited levels (i.e. the bleaching) can be monitored as a function of the pump power delivered to the sample.

The population at  $T = 37$  K of the first and second excited levels at 25 and 35 meV above the Fermi level (which corresponds to the fundamental level as shown in fig. 4.27) can be calculated using the Fermi-Dirac distribution:

$$\rho_j = \frac{1}{e^{\frac{E_j - E_F}{k_B T}} + 1} \quad (4.41)$$

where  $E_j$  is the energy of the  $j$ -th level,  $E_F$  is the energy of the Fermi level and  $k_B$  is the Boltzmann constant. The calculation shows that 0.08% of the electrons populate level  $|1\rangle$  and 50 times less electrons populate level  $|2\rangle$ . In these conditions, the optical pumping of electrons from the ground level to the upper excited level inhibits the  $|1\rangle \rightarrow |2\rangle$  absorption signal, resulting in the decrease of  $I_{L,12}$  under pumping from  $1.12 \text{ cm}^{-2}$  at  $P = 0$  to  $0.84 \text{ cm}^{-2}$  at  $P = 75 \text{ kW/cm}^2$ .

From the oscillator strength reduction we evaluated that  $8 \cdot 10^{14}$  electrons/ $\text{cm}^3$  are brought to level  $|2\rangle$  by the pump pulse, leading to a pump efficiency around 2%, compatible with the expected low photon absorption cross section of the  $|0\rangle \rightarrow |2\rangle$  ISB transition. This is the main drawback of our ACQW design, which has to be traded with the advantage of long relaxation times.

At lower temperatures the population of level  $|1\rangle$  rapidly decreases according to the Fermi distribution factor, while the same amount of electrons are pumped into level  $|2\rangle$ , favoring population inversion even at low  $P$ . Possibly, net spontaneous

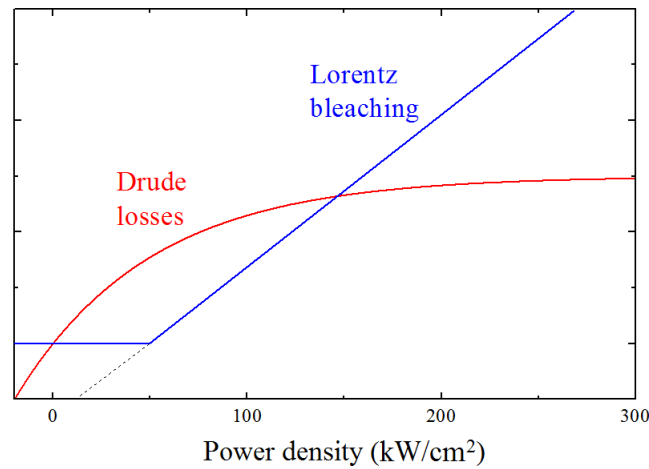


Figure 4.31: ISB transition intensity (blue line) and free carrier absorption (red line) as a function of increasing pumping power. The plots show the change of  $\sigma_D$  and  $I_{L,12}$  with respect to the equilibrium conditions at zero pumping powers.

emission may then take place at lower temperatures [8], but it could not be probed with the present coherently-locked THz-TDS probe which is insensitive to all contributions of the THz field that are not generated in the ZnTe electro-optic crystal emitter. Concerning stimulated emission, which would instead be measurable with the THz-TDS setup, population inversion should be strong enough to overcome the free carrier losses and produce a significant amplification of the THz-TDS probe beam. The density of electrons brought from level  $|0\rangle$  to level  $|2\rangle$  by the pump pulse at  $75 \text{ kW/cm}^2$  is estimated to be 20% of those previously present in level  $|1\rangle$ , according to the Fermi distribution factor at 37 K and 25 meV, meaning that population inversion is not achieved ( $n_2/n_1 \sim 0.2 < 1$ ). In fact, in the present experiment, thermal balance issues forced us to limit  $P$  to  $\sim 75 \text{ kW/cm}^2$  and  $T$  to 37 K. However, it is reasonable to ask whether positive material gain can be achieved at the energy  $E_{12}$  for higher pumping powers, assuming a negligible population  $n_1$  of the first excited level (low  $T$ ). We therefore extrapolated the trend of the model parameters of sample S9 to higher optical powers.

The two key points used in the extrapolation procedure consists in the free carrier absorption saturation around FEL pump power of  $300 \text{ kW/cm}^2$  and the ISB transition oscillator strength linear increase in the investigated range of power levels. This different behavior with increasing optical pump power of pump-induces free carrier absorption and upper level population is displayed in fig. 4.31. Such behaviors are found to be in agreement with what observed in previous works [37,108] and compatible with previous observations in degenerate pump-probe experiments performed on symmetric QWs grown on the same material platform [80].

Assuming a system temperature of  $T < 20 \text{ K}$  at which corresponds a negligible population  $n_1$  and pumping conditions in which the pumped population  $n_2$  is still low with respect to the total electron density in the ground level ( $n_1 \ll n_2 \ll n_0$ ), the trend measured at low pump powers has been extended up to FEL power of 1

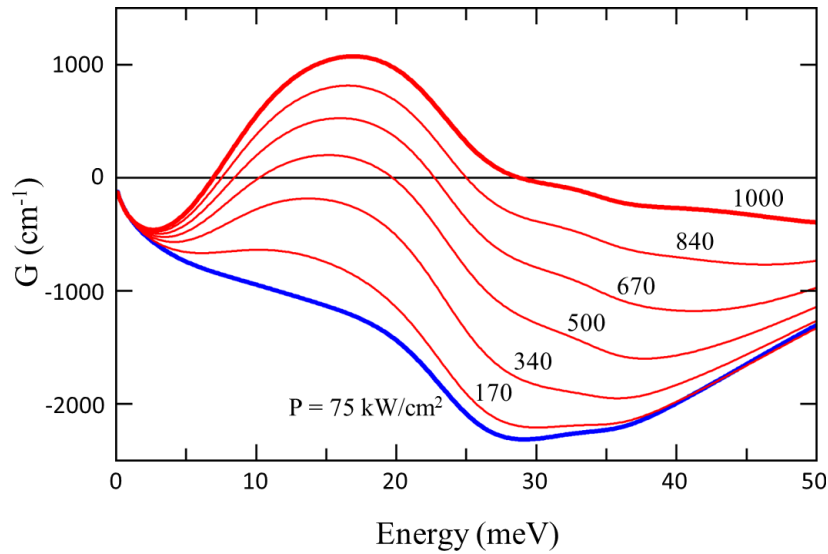


Figure 4.32: Calculated ISB gain function of sample S9 for increasing FEL pump power from the experimental value of  $75 \text{ kW/cm}^2$  (blue line) up to  $1 \text{ MW/cm}^2$  (red thick line). Positive gain values are predicted for pump power above  $500 \text{ kW/cm}^2$ .

MW/cm<sup>2</sup> to estimate the material gain spectrum, taking into account the  $|1\rangle \rightarrow |2\rangle$  ISB transition as positive contribution and free carrier and ISB losses centered at  $E_{02} = 35$  meV and  $E_{01} = 25$  meV as negative contributions. The gain function  $G(\omega) = -\alpha(\omega)$  can be derived from  $\tilde{\sigma}(\omega)$  by standard electrodynamics relations [64]. The results of this calculation are shown in fig. 4.32, in which a power threshold around FEL power of 500 kW/cm<sup>2</sup> can be identified for net positive gain at photon energies between 10 and 20 meV ( $2.5 < \omega < 5$  THz). Due to absorption in the Si substrate, such  $P$  levels probably require short-pulsed optical pumping in the picosecond range. A pump power density of 500 kW/cm<sup>2</sup> was indeed available from the FEL, but it could not be delivered to the sample without significantly increase its steady-state temperature because of thermal balance limitations. Sample heating is unavoidable in the present waveguide configuration due to pump absorption in both the 800  $\mu\text{m}$  thick Si substrate and the doped QWs, but it could be partly avoided by electromagnetic engineering of the laser cavity [109]. Future works will focus on designing suitable optical pumping schemes with the goal of reaching lasing action from Ge/SiGe QWs grown on silicon substrates, relying on the quantitative analysis reported in the present work.

# Conclusions

The work of this thesis focused on the realization and characterization of n-type Ge/SiGe quantum well (QW) heterostructures, with the aim to identify and study the properties needed for a future implementation in opto-electronic devices in the far-infrared region of the electromagnetic spectrum. The important requirement of the grown structures to be compatible with the standard Si-based microelectronics CMOS platform for the large scale production has been taken into consideration both in the choice of the materials and in the growth technique employed. Particular attention has been paid to structures suitable to achieve radiative emission from transitions within the QWs that fall in the THz band.

In this context, two different kinds of QW structures have been investigated. The first one is a multi quantum well (MQW) modulation-doped structure which consists in the periodic repetition of symmetric elements of single QWs separated by thick barriers to prevent any coupling between them. This structure has been used to the seminal study of the inter-subband (ISB) transition properties in Ge QWs and to highlight the main features useful in THz technology. Basing on the results obtained from the MQW samples, a second type of structure has been considered, and direct-doped asymmetric coupled quantum well (ACQW) samples have been realized. Here, the periodic element consists in two QWs of different width separated only by a barrier thin enough to ensure the coupling of the two wells. The introduced asymmetry reflects in a more flexible structure in which the optical properties can be tuned by varying the structural parameters. Exploiting the peculiarities of the ACQW structure, the possibility to realize a quantum fountain (QF) device has been investigated, mainly studying the ISB transition characteristics in terms of relaxation times and population inversion under optical pumping.

The investigated samples have been realized using the Chemical Vapor Deposition technique starting from Si(100) substrates, on top of which the active region can be grown. The thickness and compositions of the deposited layers have been chosen with the aim to observe ISB transitions in the THz range. In order to obtain a conduction band offset larger than 100 meV, we have realized heterostructures with Ge QWs confined by  $\text{Si}_{1-x}\text{Ge}_x$  barriers with  $0.80 < x < 0.85$ . However, the growth of these structures on top of Si(100) substrates induces the formation of a large number of defects in the crystalline structure, due to the high lattice mismatch between Si and Ge.

To overcome this problem, a virtual substrate with high Ge content can be included in the deposition process between the Si substrate and the active region. This buffer layer collects the large number of generated defects preventing them to extend along the whole sample, therefore allowing a proper deposition of the

QW heterostructure on top. Despite the major problems in the growth of Ge/SiGe systems, this strategy allowed us to obtain structures of excellent quality and to observe ISB transitions therein.

The structural characterization conducted on the realized samples testifies the high quality that can be achieved with the state-of-the-art techniques employed in the deposition process. The transmission electron microscopy (TEM) investigation on the virtual substrates shows how the reverse graded approach allows to confine in the lower layers the lattice defects generated at the interface with the Si substrate. The propagation of the threading dislocations is furthermore prevented by the interfaces between the layers of increasing Si concentration in the step graded region. This strategy results in a final layer of the virtual substrate exhibiting high crystalline quality and low lattice defect density of  $N_{TD} < 3 \cdot 10^6 \text{ cm}^{-2}$ , which are good conditions for a proper QW active region deposition. In fact, high resolution TEM images show the sub-nanometer precision of the QW heterostructure growth, with abrupt interfaces of roughness lower than 0.4 nm. It is also shown that the grown structures are almost free of extended defects and their surface roughness is as low as 3 nm, as obtained by atomic force microscopy measurements. Layers thickness and periodicity have been investigated also by X-ray diffraction measurements, whose results confirm the high precision of the grown heterostructure. Moreover, the diffraction pattern allows to evaluate the residual strain in the structure, resulting in a partially strain compensation that has been taken into account in the sample design to obtain the desired optical properties. The ensemble of the results obtained by the performed structural characterization stands as a proof of the reliability of the employed deposition techniques and of the excellent quality of the grown samples.

The optical characterization discussed in this work started with Fourier transform infrared (FTIR) spectroscopy measurements on MQW samples, in order to highlight the main optical features of a Ge QW system. The obtained transmission spectra allow to identify the ISB transitions and their principal characteristics. First of all, the transition energies have been retrieved and compared to the values predicted from a multi-band self-consistent calculations in the envelope function approximation. The experimental values are found to be in agreement with the theoretical prediction, provided the contribution of the depolarization shift is included as a correction of the empty-band calculation. All the investigated samples feature ISB transitions with energies in the THz range within the restrahlen band of III-V materials, as required by the motivation leading this work of thesis. Furthermore, the good quality of the samples is proved by the narrow absorption peaks, whose linewidth  $\Gamma$  has found to be as low as 2 meV.

The acquired transmission spectra have been also used to calculate the bi-dimensional absorption coefficient, from which it is possible to retrieve values of coherence time as high as 0.4 ps via the absorption peak linewidth. In order to correctly interpret the experimental data, a theoretical framework for the linewidth broadening of ISB transitions in modulation-doped Ge QWs in SiGe heterostructures has been developed, taking into account all the possible scattering mechanisms. The prediction obtained by the model highlights the differences in the linewidth broad-



ening for different QW thicknesses. Although some contributions are significant in both wide and narrow QWs, as it happens for the ionized impurities scattering, most of them appear negligible or dominant according to the QW thickness. In particular, narrow QWs exhibit ISB transition energies higher than the optical phonon one in Ge, leading to a high electron-phonon scattering rate. Moreover, the wavefunction of the high energy subbands is not efficiently confined in the well region but extends inside the barriers. Therefore, the wavefunction has a relatively high value at the interface with the barrier and it penetrates deeply in the SiGe layers. The consequence is a significant contribution to the linewidth broadening due to the SiGe alloy disorder and interface roughness. On the contrary, wide QWs feature low ISB transition energies and the level wavefunctions do not significantly extend in the barrier region. The result is that the scattering contributions from phonons, alloy disorder and interface roughness are almost negligible, leaving the ionized impurities scattering the only dominant term in the linewidth broadening. Also the effect of a spacer layer separating the well by the doped region in the barrier has been discussed, showing how its presence has a beneficial effect only for high electron kinetic energies, being instead detrimental at low kinetic energies. The comparison of the experimental data with the theoretical predictions highlights an extrinsic contribution due to scattering with defects. This result suggests the possibility to achieve coherence times longer than 1 ps, by improving the structural quality of the samples.

Beside the optical characterization of the samples in the steady-state conditions, investigation on the carrier dynamics has been performed with pump-probe spectroscopy measurements. Samples have been optically pumped to transfer a portion of the electron density from the ground subband to the excited one, in order to study the dynamics back to the equilibrium. The behavior of the differential transmission change has been monitored over time and compared to a computational model including subband populations and separate temperatures for the electron and phonon systems. The comparison allowed to extract the relaxation times related to the first ISB transition occurring between the first two subbands, which are found to be tens of picoseconds in a wide range of temperatures, powers and energies. The obtained result of long ISB relaxation times in Ge QWs confirmed the feasibility of the system to be employed for THz emitters, suggesting the realization of ACQW structures for the implementation in QF devices.

Different samples with the asymmetric design have been grown varying the thickness of both QWs and barriers, according to a thorough wavefunction engineering performed with the aim to obtain the proper ISB relaxation times to achieve population inversion between the two excited subbands  $|1\rangle$  and  $|2\rangle$ . In particular, the upper excited state needs to exhibit a long lifetime with the  $|2\rangle \rightarrow |1\rangle$  transition much slower than the  $|1\rangle \rightarrow |0\rangle$  one, i.e.  $\tau_{21} \gg \tau_{10}$ . To this aim, the structural parameters are set in order to obtain the  $|2\rangle \rightarrow |1\rangle$  and the  $|1\rangle \rightarrow |0\rangle$  transition energies lower and higher than the phonon one, respectively. In this way, the electron-phonon scattering from subband  $|2\rangle$  is highly suppressed and radiative emission can occur, while the scattering from subband  $|1\rangle$  is fostered to quickly depopulate the level. After confirming the transition energies with FTIR measurements, the samples have been characterized combining the techniques of pump-probe and time-domain spectroscopy (TDS). Here, the samples are optically pumped at the energy corresponding to the  $|0\rangle \rightarrow |2\rangle$

ISB transition while probed in a broadband region in the THz range. The global relaxation times back to the equilibrium in different conditions are compared with theoretical predictions and the individual relaxation times of the involved ISB transitions are extracted. The presented results showed how the successful wavefunction engineering led to relaxation times perfectly suitable for emitter devices, with values of  $\tau_{21} \simeq 200$  ps and  $\tau_{10} = 30$  ps. The corresponding relaxation time ratio  $\tau_{10}/\tau_{21} \simeq 0.15$  is found to be extremely low compared to the typical values reported for III-V systems, suggesting the possibility to achieve even better performances.

Although it was not possible to obtain population inversion in our samples due to the sub-threshold pumping forced by thermal limitations, the  $|1\rangle \rightarrow |2\rangle$  ISB absorption bleaching has been observed for increasing pumping powers, suggesting the possibility to achieve positive material gain at higher values. Therefore, we developed a model to calculate the material gain  $G(\omega)$  including the  $|1\rangle \rightarrow |0\rangle$  ISB transitions as positive contribution for the emission process, and the Drude-like free carrier absorption as the main optical loss mechanisms. The model parameters have been fitted to reproduce the experimental data at different pumping powers and their values have been extrapolated to higher powers. The result of this procedure showed how a net positive material gain can be achieved in our systems for pumping powers above  $500 \text{ kW/cm}^2$ . This value is only slightly higher than what reported for III-V systems, and can be easily lowered down with a proper cavity realization for high modal gain.

Starting from the results obtained in the ACQW structures characterization, in fact, the realization of optical resonators for positive modal gain can be possibly obtained as a long term objective and it represents the natural continuation of the present work. As a closer objective, our efforts will be put into achieving higher material gain by further optimizing the design with the eventual addition of more active subbands, in order to obtain a more flexible structure which could allow for a wider and easier tuning of the optical properties. This intermediate step towards the realization of THz emitters based on our QF design is needed to foster a favorable balance between gain and free carrier absorption, which constitutes the main and unavoidable loss mechanism.

In summary, the present work of thesis allowed to identify the main characteristics of n-type Ge/SiGe QW heterostructures for opto-electronic applications and to exploit them in the realization of engineered structures featuring properties suitable for the future implementation in QF devices for THz emission.

# Publications

## Journal Papers

M. Virgilio, M. Ortolani, M. Teich, S. Winnerl, M. Helm, D. Sabbagh, G. Capellini, M. De Seta, “Combined effect of electron and lattice temperatures on the long intersubband relaxation times of Ge/Si<sub>1-x</sub>Ge<sub>x</sub> quantum wells”, *Phys. Rev. B* 89, 045311 (2014).

E. Calandrini, M. Ortolani, A. Nucara, G. Scappucci, W. M. Klesse, M. Y. Simmons, L. Di Gaspare, M. De Seta, D. Sabbagh, G. Capellini, M. Virgilio, L. Baldassarre, “Determination of the free carrier concentration in atomic-layer doped germanium thin films by infrared spectroscopy”, *J. Opt.* 16, 094010 (2014).

M. Virgilio, D. Sabbagh, M. Ortolani, L. Di Gaspare, G. Capellini, M. De Seta, “Physical mechanisms of intersubband-absorption linewidth broadening in s-Ge/SiGe quantum wells”, *Phys. Rev. B* 90, 155420 (2014).

L. Di Gaspare, D. Sabbagh, M. De Seta, A. Sodo, S. Wirths, D. Buca, P. Zaumseil, T. Schroeder, G. Capellini, “Epi-cleaning of Ge/GeSn heterostructures”, *J. Appl. Phys.* 117, 045306 (2015).

D. Sabbagh, J. Schmidt, S. Winnerl, M. Helm, L. Di Gaspare, M. De Seta, M. Virgilio, M. Ortolani, “Electron dynamics in silicon-germanium terahertz quantum fountain structures”, submitted to *ACS Photonics* (2015).

## Conferences

D. Sabbagh, L. Di Gaspare, G. Capellini, M. Virgilio, M. Ortolani, M. De Seta, “Depolarization shift by plasmons in n-doped Germanium Quantum Wells”, *Plasmonica14*, Rome (2014).

D. Sabbagh, M. Virgilio, M. De Seta, L. Di Gaspare, J. Schmidt, S. Winnerl, M. Helm, M. Ortolani, “Intersubband relaxation in a 3-level coupled quantum well system probed by THz pump-probe time-domain spectroscopy”, *German THz Conference 2015*, Dresden (2015).

D. Sabbagh, L. Di Gaspare, M. Virgilio, M. Ortolani, G. Capellini, P. Zaumseil, J. Schmidt, S. Winnerl, M. Helm, M. De Seta, “n-type s-Ge/SiGe quantum wells as promising material for THz lasing”, *E-MRS Fall meeting 2015*, Warsaw (2015).



# Bibliography

- [1] M. Helm, P. England, E. Colas, F. DeRosa, S. J. Allen, *Phys. Rev. Lett.* 63, 74 (1989).
- [2] J. H. Smet, C. G. Fonstad, Q. Hu, *J. Appl. Phys.* 79, 9305 (1996).
- [3] M. Helm, “Intersubband Transitions in Quantum Wells. In Semiconductors and Semimetals”, edited by H. C. Liu and F. Capasso, Academic Press (2000).
- [4] B. S. Williams, *Nature Photonics* 1, 517 (2007).
- [5] D. J. Paul, *Laser & Photon. Rev.* 4, 610 (2010).
- [6] G. Dehlinger, L. Diehl, U. Gennser, H. Sigg, J. Faist, K. Ensslin, D. Grützmacher, E. Müller, *Science* 290, 2277 (2000).
- [7] S. A. Lynch, R. Bates, D. J. Paul, D. J. Norris, A. G. Cullis, Z. Ikonić, R. W. Kelsall, P. Harrison, D. D. Arnone, C. R. Pidgeon, *Appl. Phys. Lett.* 81, 1543 (2002).
- [8] R. Bates, S. A. Lynch, D. J. Paul, Z. Ikonić, R. W. Kelsall, P. Harrison, S. L. Liew, D. J. Norris, A. G. Cullis, W. R. Tribe, D. D. Arnone, *Appl. Phys. Lett.* 83, 4092 (2003).
- [9] D. J. Paul, *Semiconductor Science and Technology* 19, 75 (2004).
- [10] D. Indjin, Z. Ikonić, V. D. Jovanović, N. Vukmirović, P. Harrison, R. W. Kelsall, *Semicond. Sci. Technol.* 20, 237 (2005).
- [11] C. R. Pidgeon, P. J. Phillips, D. Carder, B. N. Murdin, T. Fromherz, D. J. Paul, Wei-Xin Ni, Ming Zhao, *Semicond. Sci. Technol.* 20, L50 (2005).
- [12] K. Driscoll, R. Paiella, *J. Appl. Phys.* 102, 093103 (2007).
- [13] P. Rauter, T. Fromherz, N. Q. Vinh, B. N. Murdin, J. P. Phillips, C. R. Pidgeon, L. Diehl, G. Dehlinger, D. Grützmacher, Ming Zhao, Wei-Xin Ni, G. Bauer, *New J. Phys.* 9, 128 (2007).
- [14] P. Rauter, T. Fromherz, C. Falub, D. Grützmacher, G. Bauer, *Appl. Phys. Lett.* 94, 081115 (2009).
- [15] A. Valavanis, T. V. Dinh, L. J. M. Lever, Z. Ikonić, R. W. Kelsall, *Phys. Rev. B* 83, 195321 (2011).

- [16] P. Sookchoo, F. F. Sudradjat, A. M. Kiefer, H. Durmaz, R. Paiella, M. G. Lagally, *ACS Nano* 7, 2326 (2013).
- [17] C. Cicek Boztug, J. R. Sanchez-Pérez, F. Cavallo, M. G. Lagally, R. Paiella, *ACS Nano* 8, 3136 (2014).
- [18] S. Wirths, R. Geiger, N. von den Driesch, G. Mussler, T. Stoica, S. Mantl, Z. Ikonić, M. Luysberg, S. Chiussi, J. M. Hartmann, H. Sigg, J. Faist, D. Buca, D. Grützmacher, *Nature Photon.* 9, 88 (2015).
- [19] J. Faist, F. Capasso, D. L. Sivco, C. Sirtori, A. L. Hutchinson, A. Y. Cho, *Science* 264, 553 (1994).
- [20] R. Köhler, A. Tredicucci, F. Beltram, H. E. Beere, E. H. Linfield, A. G. Davies, D. A. Ritchie, R. C. Iotti, F. Rossi, *Nature* 417, 156 (2002).
- [21] M. Tonouchi, *Nature Phot.* 1, 97 (2007).
- [22] D. Grischkowsky, S. Keiding, M. van Exter, C. Fattinger, *J. Opt. Soc. Am. B* 7, 2006 (1990).
- [23] Q. Wu, T. D. Hewitt, X. C. Zhang, *Appl. Phys. Lett.* 69, 1026 (1996).
- [24] M. De Seta, G. Capellini, Y. Busby, F. Evangelisti, M. Ortolani, M. Virgilio, G. Grosso, G. Pizzi, A. Nucara, S. Lupi, *Appl. Phys. Lett.* 95, 051918 (2009).
- [25] A. Valavanis, Z. Ikonić, L. Lever, C. A. Evans, R. W. Kelsall, *Proceedings of the 5th IEEE International Conference on Group IV Photonics*, Sorrento, Italy, 2008 (IEEE, New York, 2008).
- [26] P. See, D. J. Paul, *Electron Device Letters* 22, 582 (2001).
- [27] P. Murzyn, C. R. Pidgeon, J. P. R. Wells, I. V. Bradley, Z. Ikonić, R. W. Kelsall, P. Harrison, S. A. Lynch, D. J. Paul, D. D. Arnone, D. J. Robbins, D. Norris, A. G. Cullis, *Appl. Phys. Lett.* 80, 1456 (2002).
- [28] R. W. Kelsall, Z. Ikonić, P. Murzyn, C. R. Pidgeon, P. J. Phillips, D. Carder, P. Harrison, S. A. Lynch, P. Townsend, D. J. Paul, S. L. Liew, D. J. Norris, A. G. Cullis, *Phys. Rev. B* 71, 115326 (2005).
- [29] P. Rauter, T. Fromherz, G. Bauer, N. Q. Vinh, B. N. Murdin, J. P. Phillips, C. R. Pidgeon, L. Diehl, G. Dehlinger, D. Grützmacher, *Appl. Phys. Lett.* 89, 211111 (2006).
- [30] A. Valavanis, L. Lever, C. A. Evans, Z. Ikonić, R. W. Kelsall, *Phys. Rev. B* 78, 035420 (2008).
- [31] G. Ciasca, M. De Seta, G. Capellini, F. Evangelisti, M. Ortolani, M. Virgilio, G. Grosso, A. Nucara, P. Calvani, *Phys. Rev. B* 79, 085302 (2009).
- [32] M. Virgilio, G. Grosso, *Journal of Physics: Condensed Matter* 18, 1021 (2006).

- [33] Y. Lavon, A. Sa'ar, Z. Moussa, F. H. Julien, R. Planel, *Appl. Phys. Lett.* 67, 1984 (1995).
- [34] O. Gauthier-Lafaye, P. Boucard, F. H. Julien, S. Sauvage, S. Cabaret, J. M. Lourtioz, V. Thierry-Mieg, R. Planel, *Appl. Phys. Lett.* 71, 3619 (1997).
- [35] O. Gauthier-Lafaye, S. Sauvage, P. Boucaud, F. H. Julien, F. Glotin, R. Prazeres, J. M. Ortega, V. Thierry-Mieg, R. Planel, *J. Appl. Phys.* 83, 2920 (1998).
- [36] O. Gauthier-Lafaye, F. H. Julien, S. Cabaret, J. M. Lourtioz, G. Strasser, E. Gornik, M. Helm, P. Bois, *Appl. Phys. Lett.* 74, 1537 (1999).
- [37] O. Gauthier-Lafaye, B. Seguin-Roa, F. H. Julien, P. Collot, C. Sirtori, J. Y. Duboz, G. Strasser, *Physica E* 7, 12 (2000).
- [38] N. Vukmirović, V. D. Jovanović, D. Indjin, Z. Ikonić, P. Harrison, V. Milanović, *J. Appl. Phys.* 97, 103106 (2005).
- [39] M. Beeler, E. Trichas, E. Monroy, *Semicond. Sci. Technol.* 28, 074022 (2013).
- [40] M. Califano, N. Q. Vinh, P. J. Phillips, Z. Ikonić, R. W. Kelsall, P. Harrison, C. R. Pidgeon, B. N. Murdin, D. J. Paul, P. Townsend, J. Zhang, I. M. Ross, A. G. Cullis, *Phys. Rev. B* 75, 045338 (2007).
- [41] N. W. Ashcroft, N. D. Mermin, "Solid State Physics", Saunders College Publishing (1976).
- [42] J. H. Davies, "The Physics of Low-Dimensional Semiconductors", Cambridge University Press (1998).
- [43] R. Braustein, *Phys. Rev.* 109 (1958).
- [44] J. Weber, M. I. Alonso, *Phys. Rev. B* 40, 5683 (1989).
- [45] M. Rieger, P. Vogl, *Phys. Rev. B* 48, 14276 (1993).
- [46] F. Schäffler, *Semicond. Sci. Technol.* 12, 1515 (1997).
- [47] G. Capellini, M. De Seta, Y. Busby, M. Pea, F. Evangelisti, G. Nicotra, C. Spinella, M. Nardone, C. Ferrari, *J. Appl. Phys.* 107, 063504 (2010).
- [48] F. L. Fabbri, F. Cembali, M. Servidori, and A. Zani, *J. Appl. Phys.* 74, 2359 (1993).
- [49] E. Ayers, "Heteroepitaxy of semiconductors: theory, growth, and characterization", Taylor and Francis Group (2007).
- [50] R. People, J. C. Bean, *Appl. Phys. Lett.* 47, 322 (1985).
- [51] E. Bauer, *Z. Kristallogr.* 110, 372 (1958).
- [52] F. C. Frank, J. H. Van Der Merwe, *Proc. R. Soc. London* 198, 205 (1949).

- [53] B. V. Volmer, A. Weber, *Z. Phys. Chem.* 119, 277 (1926).
- [54] I. N. Stranski, L. Krastanov, *Sitzungsber. Akad. Wiss. Wien* 146, 797 (1938).
- [55] J. W. Matthews, A. E. Blakeslee, *J. Cryst. Growth* 32, 265 (1976).
- [56] M. T. Currie, S. B. Samavedam, T. A. Langdon, C. W. Leitz, E. A. Fitzgerald, *App. Phys. Lett.* 72, 1718 (1998).
- [57] K. Sawano, K. Kawaguchi, S. Koh, Y. Hirose, T. Hattori, K. Nakagawa, Y. Shiraki, *J. Electrochem. Soc.* 150, G376 (2003).
- [58] L. H. Wong, J. P. Liu, F. Romanato, C. C. Wong, Y. L. Foo, *Appl. Phys. Lett.* 90, 061913 (2007).
- [59] B. Cunningham, J. O. Chu, S. Akbar, *Appl. Phys. Lett.* 59, 3574 (1991).
- [60] L. Colace, G. Masini, F. Galluzzi, G. Assanto, G. Capellini, L. Di Gaspare, E. Palange, F. Evangelisti, *Appl. Phys. Lett.* 72, 3175 (1998).
- [61] V. A. Shah, A. Dobbie, M. Myronov, D. J. F. Fulgoni, L. J. Nash, D. R. Leadley, *Appl. Phys. Lett.* 93, 192103 (2008).
- [62] C. Sirtori, F. Capasso, J. Faist, S. Scandolo, *Phys. Rev. B* 50, 8663 (1994).
- [63] H. C. Liu, *J. Appl. Phys.* 73, 3062 (1993).
- [64] M. Dressel, G. Grüner, “Electrodynamics of solids”, Cambridge University Press (2002).
- [65] Y. Busby, M. De Seta, G. Capellini, F. Evangelisti, M. Ortolani, M. Virgilio, G. Grosso, G. Pizzi, P. Calvani, S. Lupi, M. Nardone, G. Nicotra, C. Spinella, *Phys. Rev. B* 82, 205317 (2010).
- [66] F. Stern, W. E. Howard, *Phys. Rev.* 163, 816 (1967).
- [67] M. Virgilio, G. Grosso, G. Pizzi, M. De Seta, G. Capellini, M. Ortolani, *Phys. Rev. B* 86, 205317 (2012).
- [68] M. De Seta, G. Capellini, M. Ortolani, M. Virgilio, G. Grosso, G. Nicotra, P. Zaumseil, *Nanotechnology* 23, 465708 (2012).
- [69] S. J. Allen, D. C. Tsui, B. Vinter, *Solid State Commun.* 20, 425 (1976).
- [70] T. Ando, A. B. Fowler, F. Stern, *Rev. Mod. Phys.* 54, 437 (1982).
- [71] T. Ando, *Solid State Commun.* 21, 133 (1977).
- [72] T. Ando, *Z. Phys. B* 26, 263 (1977).
- [73] W. Kohn, L. J. Sham, *Phys. Rev.* 140, A1133 (1965).
- [74] K. S. M. Bandara, D. D. Coon, O. Byungsung, Y. F. Lin, M. H. Francombe, *Appl. Phys. Lett.* 53, 1931 (1988); erratum: *Appl. Phys. Lett.* 55, 206 (1989).



- [75] V. S. Kopp, V. M. Kaganer, G. Capellini, M. De Seta, P. Zaumseil, *Phys. Rev. B* 85, 245311 (2012).
- [76] S. G. Pavlov, U. Böttger, R. Eichholz, N. V. Abrosimov, H. Riemann, V. N. Shastin, B. Redlich, H. W. Hübers, *Appl. Phys. Lett.* 95, 201110 (2011).
- [77] P. R. Griffiths, J. A. De Haseth, “Fourier Transform Infrared Spectroscopy”, John Wiley and sons (1986).
- [78] M. A. Stroschio, “Phonons in Nanostructures”, Cambridge University Press (2001).
- [79] B. K. Ridley, *Phys. Rev. B* 39, 5282 (1989).
- [80] M. Virgilio, D. Sabbagh, M. Ortolani, L. Di Gaspare, G. Capellini, M. De Seta, *Phys. Rev. B* 90, 155420 (2014).
- [81] K. Driscoll, R. Paiella, *Appl. Phys. Lett.* 89, 191110 (2006).
- [82] G. Sun, H. H. Cheng, J. Menendez, J. B. Khurgin, R. A. Soref, *Appl. Phys. Lett.* 90, 251105 (2007).
- [83] L. Lever, A. Valavanis, Z. Ikonić, R. W. Kelsall, *Appl. Phys. Lett.* 92, 021124 (2008).
- [84] L. Lever, A. Valavanis, C. A. Evans, Z. Ikonić, R. W. Kelsall, *Appl. Phys. Lett.* 95, 131103 (2009).
- [85] D. Stehr, S. Winnerl, M. Helm, T. Dekorsy, T. Roch, G. Strasser, *Appl. Phys. Lett.* 88, 151108 (2006).
- [86] S. Lutgen, R. A. Kaindl, M. Woerner, T. Elsaesser, A. Hase, H. Kunzel, M. Gulia, D. Meglio, P. Lugli, *Phys. Rev. Lett.* 77, 3657 (1996).
- [87] M. Fischetti, *IEEE Trans. Electron Devices* 38, 634 (1991).
- [88] S. Barbieri, M. Ravaro, P. Gellie, G. Santarelli, C. Manquest, C. Sirtori, S. P. Khanna, E. H. Linfield, A. G. Davies, *Nature Photon.* 5, 303 (2011).
- [89] H. C. B. Skjeie, “Terahertz Time-Domain Spectroscopy”, PhD thesis (2012).
- [90] P. Kinsler, P. Harrison, R. W. Kelsall, *Phys. Rev. B* 58, 4771 (1998).
- [91] O. Gunnarsson, B. I. Lundqvist, *Phys. Rev. B* 13, 4274 (1976).
- [92] A. A. Batista, D. S. Citrin, *Phys. Rev. Lett.* 92, 127404 (2004).
- [93] C. W. Luo, K. Reimann, M. Woerner, T. Elsaesser, R. Hey, K. H. Ploog, *Phys. Rev. Lett.* 92, 047402 (2004).
- [94] D. E. Nikonov, A. Imamoglu, L. V. Butov, H. Schmidt, *Phys. Rev. Lett.* 79, 4633 (1997).

- [95] T. Unuma, M. Yoshita, T. Noda, H. Sakaki, H. Akiyama, *J. Appl. Phys.* 93, 1586 (2003).
- [96] T. Ando, *J. Phys. Soc. Jpn.* 44, 765 (1978).
- [97] T. Ando, *J. Phys. Soc. Jpn.* 54, 2671 (1985).
- [98] S. K. Chun, D. S. Pan, K. L. Wang, *Phys. Rev. B* 47, 15638 (1993).
- [99] B. Mukhopadhyay, P. K. Basu, *Phys. Status Solidi B* 241, 1859 (2004).
- [100] C. Jacoboni, F. Nava, C. Canali, G. Ottaviani, *Phys. Rev. B* 24, 1014 (1981).
- [101] M. Ortolani, D. Stehr, M. Wagner, M. Helm, G. Pizzi, M. Virgilio, G. Grosso, G. Capellini, M. De Seta, *Appl. Phys. Lett.* 99, 201101 (2011).
- [102] J. B. Khurgin, G. Sun, L. R. Friedman, A. Soref, *J. Appl. Phys.* 78, 7398 (1995).
- [103] F. H. Julien, J. P. Leburton, “Infraed Intersubband Emission in Optically Pumped Quantum wells. In Long Wavelength Infrared Emitters Based on Quantum Wells and Superlattices”, edited by M. Helm, Gordon and Breach Science Publishers (2000).
- [104] Q. Wu, X. C. Zhang, *Appl. Phys. Lett.* 70, 1784 (1997).
- [105] S. Casalbuoni, H. Schlarb, B. Schmidt, P. Schmüser, B. Steffen, A. Winter, *Phys. Rev. ST Accel. Beams* 11, 072802 (2008).
- [106] B. S. Williams, B. Xu, Q. Hu, M. R. Melloch, *Appl. Phys. Lett.* 75, 2927 (1999).
- [107] R. P. S. M. Lobo, J. D. La Veigne, D. H. Reitze, D. B. Tanner, H. Barber, E. Jacques, P. Bosland, J. Burns, G. L. Carr, *Phys. Rev. B* 72, 024510 (2005).
- [108] A. Liu, C. Z. Ning, *Appl. Phys. Lett.* 75, 1207 (1999).
- [109] S. Tomić, V. Milanović, Z. Ikonić, *IEEE J. Quantum Electron.* 37, 1337 (2001).

